Doklady Physics, Vol. 45, No. 9, 2000, pp. 435–438. Translated from Doklady Akademii Nauk, Vol. 374, No. 1, 2000, pp. 31–34.

PHYSICS

Electric Field Effect on Photoluminescence Spectra of High-Density Two-Dimensional Electron Gas in *N*-AlGaAs/GaAs/AlGaAs Heterostructures

A. V. Guk, L. É. Velikovskiĭ, V. É. Kaminskiĭ,
Corresponding Member of the RAS V. G. Mokerov, Yu. V. Fedorov, and Yu. V. Khabarov

Received April 4, 2000

The photoluminescence (PL) spectroscopy of quantum wells with modulated doping (where both types of charge carriers are spatially bounded) is an efficient method for studying optical transitions involving subbands of two-dimensional electron gas (2DEG) [1–4]. The PL provides information on the widths of 2D quantum subbands, their splitting, band filling, and overlap of wave functions. In contrast to galvanomagnetic measurements, these data can be obtained not only at sufficiently low temperatures (<10 K), but at $T > 77$ K as well.

Additional information on the behavior of 2D electron gas in quantum wells with modulated doping can be gained from the analysis of the effect produced on the PL spectra by the electric field F applied across the surface barrier. The field F acts only upon mobile charge carriers; therefore, the main effects manifesting themselves in this case are those related to electrons bounded due to the action of the self-consistent potential formed by the electrons themselves. Here, the component related to their spatial bounding by the heterobarriers does not change. From the viewpoint of applications, such studies provide useful data on the behavior of electron subbands in the channel of a high electron mobility transistor (HEMT) device as a function of the voltage across the transistor gate, i.e., of its operation mode.

In this paper, we study the electric field effect on the PL spectra of *N*-AlGaAs/GaAs/AlGaAs quantum wells with modulated doping.

The heterostructure samples under study were grown by molecular-beam epitaxy onto semi-insulating GaAs (001) substrates at 610°C. The samples contained a buffer layer of undoped GaAs 0.1 μm thick. The following layers were subsequently grown onto the buffer layer: a 0.5-μm-thick contact layer of silicon-doped $n^+(7 \times 10^{17}$ cm$^{-3})$ GaAs, a 0.1-μm-thick lower heterobarrier layer of undoped $Al_{0.25}Ga_{0.75}As$, a 20-nm-thick quantum well layer of undoped GaAs (in which the 2D electron gas was formed), a 10-nm-thick heterobarrier spacer layer of undoped $Al_{0.25}Ga_{0.75}As$, a 10-nm-thick silicon doped $n^+(3 \times 10^{18}$ cm$^{-3})$ heterobarrier layer of $Al_{0.25}Ga_{0.75}As$ (serving as an electron source), a 13-nm-thick heterobarrier layer of undoped $Al_{0.25}Ga_{0.75}As$, and, finally, a thin (5 nm) protective layer of undoped GaAs. The cross section of the heterostructure is shown in Fig. 1.

To apply an electric field across the sample, two contacts were formed: a barrier contact on the outer

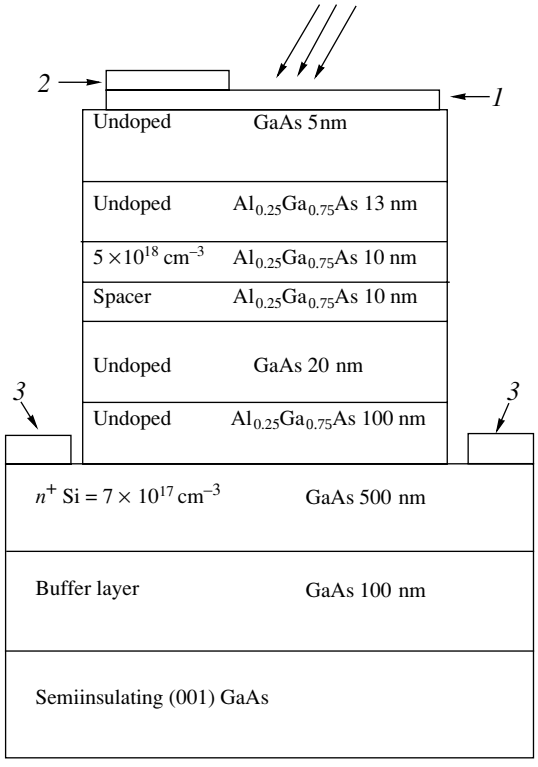

Fig. 1. Cross section of the *N*-AlGaAs/GaAs/AlGaAs/n^+GaAs quantum well for PL measurements in the electric field: (*1*) semitransparent (10 nm) gold layer; (*2*) thick (0.3 μm) contact gold layer; (*3*) ohmic Au/Ge/Ni contacts.

Institute of Radio Engineering and Electronics, Russian Academy of Sciences, ul. Mokhovaya 11, Moscow, 103907 Russia

1028-3358/00/4509-0435$20.00

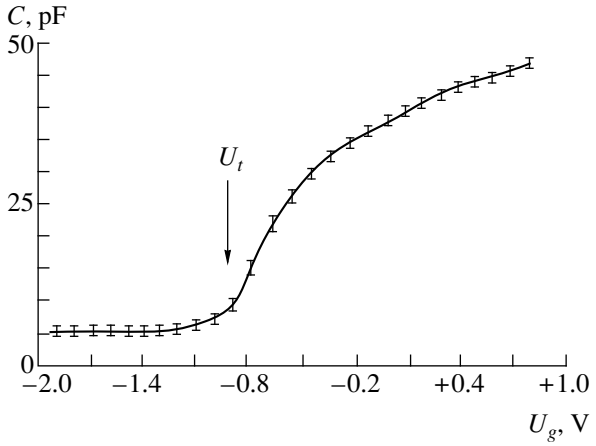

Fig. 2. Capacitance–voltage (*C–V*) characteristics of quantum well *N*-AlGaAs/GaAs/AlGaAs/n^+GaAs at various voltages U_g across the Schottky gate.

surface of the sample and an ohmic contact at the buried n^+ GaAs layer (Fig. 1). For the latter, a mesa region was etched off using optical lithography down to the n^+ GaAs layer. At the latter layer, Au/Ge/Ni ohmic contact was produced by sputtering and subsequent thermal annealing. The barrier contact was formed by the deposition of gold onto the outer surface of the heterostructure. This contact consisted of two components: the lower (about 10 nm thick) semitransparent layer, which covered the entire operating surface of the sample, and a thicker upper layer (about 0.3 μm) occupying 20% of the operating area. The external electrode was attached to this upper layer.

The PL measurements were performed at $T = 77$ K. As an excitation source of PL, we used an Ar^+ laser characterized by the wavelength $\lambda = 514$ nm and radiation density up to 100 W/cm^2. The capacitance–voltage (*C–V*) characteristics were also measured. These measurements were carried out for sample regions smaller by a factor of 100–200 than those for PL measurements. The voltage across the Schottky gate varied within the range –1.5 to 1.0 V.

Table 1. Parameters of the PL spectra: spectral positions of peaks $h\nu_1$ and $h\nu_2$, the separation $h\Delta\nu_{12}$ between them, and the ratios of their intensities I_2/I_1 at various voltages U_g across the gate

U_g, V	$h\nu_1$, eV	$h\nu_2$, eV	$h\Delta\nu_{12}$, meV	I_2/I_1
–1.5	1.510	–	–	0
–1.0	1.507	1.530	23	0.52
–0.5	1.505	1.530	25	1.45
0	1.505	1.530	25	2.64
0.5	1.500	1.527	27	2.91

The PL spectra of one of the samples are shown in Fig. 2 for various U_g, and the corresponding *C–V* curve is presented in Fig. 3. The "cutoff" voltage of the transistor structure $U_T = -1.0$ V (or the threshold voltage) is indicated by the arrows in Fig. 3. Below this value, electrons are absent in the quantum well (i.e., in the device channel), whereas at higher voltages, $U_g > U_T$, the channel becomes populated by electrons and their density n_{2D} increases with U_g.

According to Fig. 3, in the case $U_g = -1.5$ V ($U_g < U_T$), only a single line corresponding to the photon energy $h\nu_e = 1.511$ eV is present in the PL spectrum, and for $U_g = -1.0$ V ~ U_T, two PL lines are observed: the more intense line at $h\nu_1 = 1.507$ eV and the second less intense line at $h\nu_2 = 1.530$ eV. With the voltage increase at the gate, the intensity I_2 of the second line increases and, at $U_g > -0.5$ V, it becomes larger than intensity I_1 of the first line, which, in turn, is shifted toward lower $h\nu$ (Fig. 1). The main characteristic parameters of the spectra under study, namely, $h\nu_1$, $h\nu_2$, $h\Delta\nu_{12} = h(\nu_1 - \nu_2)$, and I_2/I_1 are presented in the table for various values of U_g.

With allowance for our previous studies of PL spectra for quantum wells with modulated doping [4], we can suggest an interpretation of the data obtained. The line $h\nu_0$ observed at $U_g = -1.5$ V ($U_g < U_T$) corresponds to optical transitions between the lowest electron subband e_1 and hole subbands in the "empty" quantum well, which seems to be quasi-rectangular (due to its depletion by the negative voltage applied across the gate). On the other hand, the two lines $h\nu_1$ and $h\nu_2$ observed at $U_g > U_T$, i.e., after the quantum wells have been filled by electrons, should be attributed to optical transitions from the filled electron subbands e_1 and e_2 into hole subbands in a quasi-triangular quantum well. The increase in intensity I_2 with U_g, which is observed here, should be related to the increase in filling of upper band e_2 and with the transformation of the quantum well from the quasi-rectangular shape to the quasi-triangular one.

To verify the suggested interpretation, we calculated the $n_{2D}(U_g)$ dependence for the heterostructure under study. Its band structure is illustrated in Fig. 4. The $n_{2D}(U_g)$ dependence was calculated based on the solution to the equations:

$$n_{2D} = \frac{\chi(U_g - U_T - \varphi_0)}{q(d + d_s)}. \quad (1)$$

Here, χ is the dielectric constant, U_g is the gate voltage φ_0 (Fig. 4), and U_T is the threshold voltage:

$$U_T = \varphi_B - \frac{qN_{Si}^+ d}{\chi}, \quad (2)$$

N_{Si}^+ is the concentration of ionized donors and φ_B is the

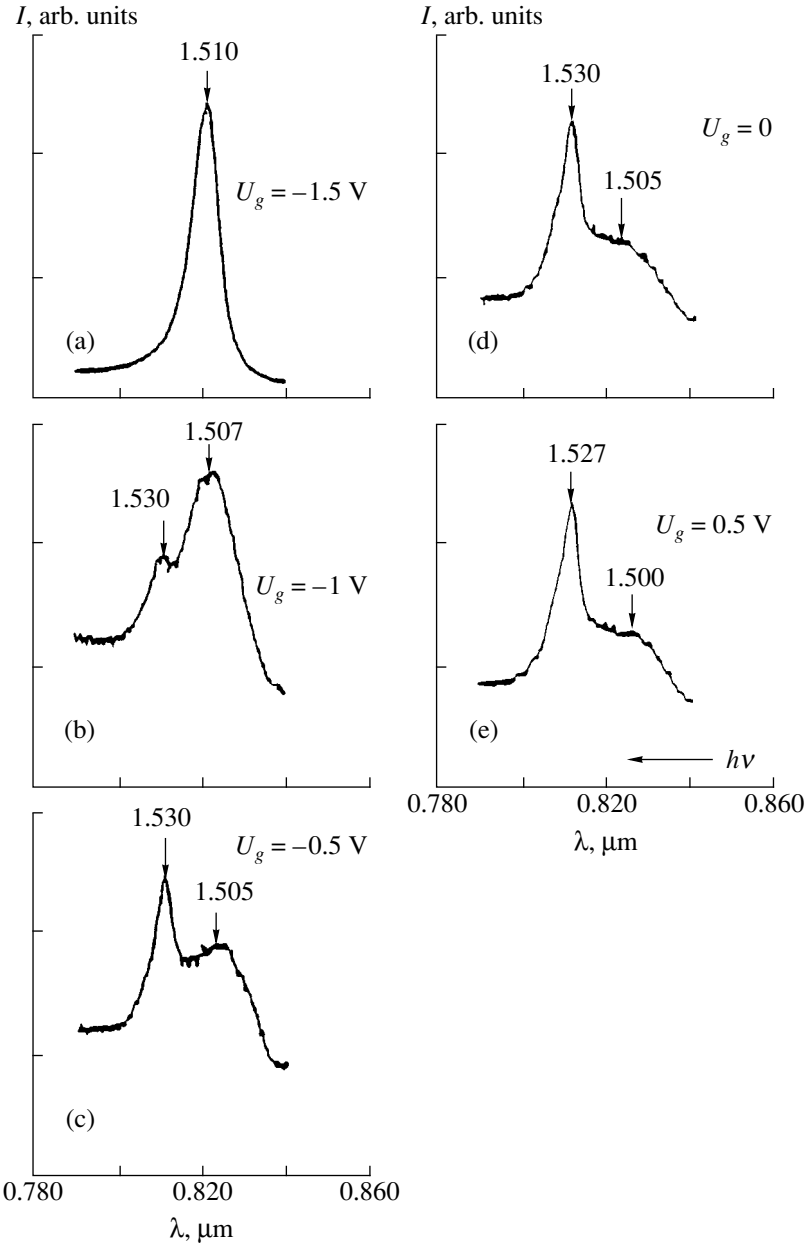

Fig 3. PL spectra of the modulating-doped quantum well *N*-AlGaAs/GaAs/AlGaAs/n^+GaAs for various values of the voltage U_g at the Schottky gate.

barrier height towards GaAs.

$$N_{\mathrm{Si}}^{+} = \frac{N_{\mathrm{Si}}}{1 + 2\exp\left(\dfrac{q^2 n_{2\mathrm{D}} d_s}{\chi^{kT}} + \dfrac{q\varphi_0 + E_D + \Delta E_C}{kT}\right)}, \quad (3)$$

where E_D is the ionization energy of Si donors and U_T = –1.2 V. At U_g > –0.6 V, $n_{2\mathrm{D}}$ attains the saturation value

$$C = \frac{d}{dU_G}(N_{\mathrm{Si}}^{+} - n_{2\mathrm{D}}). \quad (4)$$

The calculations demonstrated that the most pronounced dependence of $n_{2\mathrm{D}}$ on U_g is observed at U_g ranging from –1 to –0.6 V. In this case, $n_{2\mathrm{D}}$ rapidly increases from nearly zero values up to 6.1×10^{11} cm^{-2}, and then it remains almost constant. Using these data, the PL spectra were calculated by finding the self-consistent solution to the Schrödinger and Poisson equations [4]. It was found that the line $h\nu_1$ includes 1*e*–1*hh*, 1*e*–2*hh*, and 1*e*–1*lh* transitions, where 1*hh* and 2*hh* are the first and the second subbands of heavy holes, respectively, and 1*lh* is the first subband of light holes. The $h\nu_2$ line observed only for the filled e_2 subband corresponds to the optical 2*e*–1*hh* and 2*e*–1*lh* transitions.

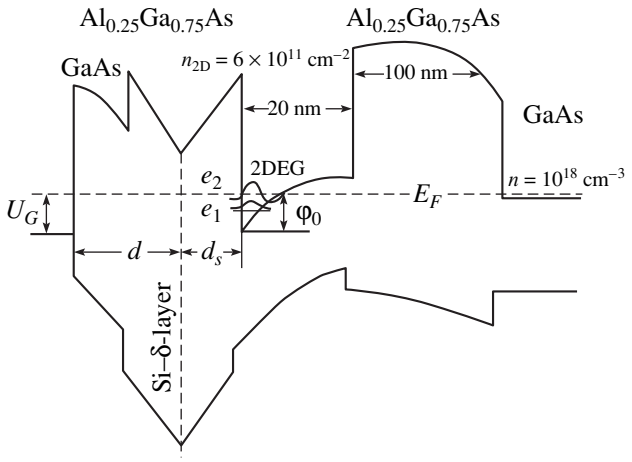

Fig. 4. Schematic band structure of *N*-AlGaAs/GaAs/AlGaAs/n^+GaAs quantum wells with modulated doping (d_s = 10 nm, d = 18 nm).

The calculations confirmed that the changes in the PL spectra accompanied by the increase in U_g (Fig. 2) are related to the increased electron filling of the quantum well. Close to U_T, the electron concentration n_{2D} increases so steeply that both subbands became filled almost immediately. The shape of the quantum well undergoes certain changes, but they are not significant. This is confirmed by the data presented in Fig. 2 and in the table. The data demonstrate that the distance $h\Delta\nu_{12}$ between the lines $h\nu_1$ and $h\nu_2$, corresponding to the energy gap between the subbands e_2 and e_1 and the spectral position of the line $h\nu_2$, do not change very much with the increase in U_g. The observed shift of the line $h\nu_1$ (~11 meV) for U_g ranging from –1.0 up to +0.5 V indicates that the increase in the self-consistent bending of the bands does not exceed 6–10 meV.

The results obtained demonstrate that the PL spectra of quantum wells with modulated doping measured as a function of the gate voltage present an efficient method, which provides an opportunity to study the behavior of 2DEG quantum subbands directly in the HEMT device channel. It also provides deeper insight into the principles underlying the operation of this device. In this connection, we can assume that the effect of rapid simultaneous filling of two electron subbands at a slight change of U_g in the vicinity of its threshold value is responsible for the enhanced steepness $g_m = \dfrac{dI_{sd}}{dU_g}$ (I_{sd} is the drain current) in the HEMT devices as compared to conventional field-effect transistors.

ACKNOWLEDGMENTS

This work was supported by the Russian Ministry of Science and Technology in the framework of the program “Physics of Solid-State Nanostructures.”

REFERENCES

1. Y. K. Yuan, K. Mohammed, M. A. A. Pudensi, *et al.*, Appl. Phys. Lett. **45**, 739 (1984).
2. Zh. I. Alferov, A. M. Vasil’ev, P. S. Kop’ev, *et al.*, Pis’ma Zh. Éksp. Teor. Fiz. **43**, 442 (1986) [JETP Lett. **43**, 569 (1986)].
3. I. V. Kukushkin, K. von Klitzing, and L. Ploog, Phys. Rev. B **37**, 8509 (1988).
4. A. V. Guk, V. É. Kaminskiĭ, V. G. Mokerov, *et al.*, Fiz. Tekh. Poluprovodn. (St. Petersburg) **31**, 1367 (1997) [Semiconductors (St. Petersburg) **31**, 1178 (1997)].

Translated by T. Galkina

Doklady Physics, Vol. 45, No. 9, 2000, pp. 439–442. Translated from Doklady Akademii Nauk, Vol. 374, No. 2, 2000, pp. 180–183.

PHYSICS

The Effect of Surface Fractal Characteristics of Solid Electrolytes on Temperature Dependence for Constant-Phase-Angle Elements

Ya. L. Kobelev* and Corresponding Member of the RAS E. P. Romanov**

Received April 26, 2000

1. INTRODUCTION

Temperature dependence of a constant-phase-angle element (CPA element) of solid electrolyte (non-Debye dependence of the impedance on the alternating current frequency) is caused by complicated physical processes occurring during the temperature change and resulting in the reconstruction of atomic clusters both at the electrolyte/electrode contact interface and at the surfaces of crystallites forming solid electrolytes. In this case, the temperature-dependent fractal structure of the cluster distribution over the surface of crystallites plays the main role.

Soon after the Mandelbrot paper [1], more than twenty fractal theories of CPA elements appeared. These theories took into account various factors affecting the fractal structure and, therefore, suggested various dependences of CPA element α on the fractal dimension d of the surface (see, e.g., [2–8]). However, these theories are not able to describe the temperature dependence of CPA elements. At this time, there is only one statistical theory of the temperature dependence of CPA elements in which the fractal structure of the crystallite surface is taken into account [9]. At the same time, the calculations of the temperature dependence for a CPA element within the framework of at least the main fractal models of CPA elements using the approach of [9] are of significant interest. Such calculations would allow us to choose with more confidence suitable fractal models to describe physical properties of actual (including also the low-temperature) solid electrolytes and, thus, to estimate the effect of fractal structure on physical properties of electrolytes. The latter problem is not simple, although it is quite important. The goal of this paper is to use the dependence of CPA elements in fractal models [2–8] on the fractal dimension of the crystallite surface for description of the temperature dependence of CPA elements in the framework of statistical theory of such an element [9].

2. STATISTICAL THEORY OF THE CONSTANT-PHASE-ANGLE ELEMENT

The fractal theory of temperature dependence for a CPA element [9] is based on the assumption that the CPA element of a polycrystalline electrolyte can be calculated as a mean value of the CPA elements for surfaces of various crystallites forming a solid electrolyte. For each of these crystallites, the cluster distribution over the surface determining CPA elements has its own value of fractal dimension. It can also be calculated as a mean value of CPA elements for small regions of the surface of the electrolyte/electrode contact in the monocrystalline solid electrolyte, which have different values of fractal dimension due to distortion of the crystal structure, the presence of vacancies, etc. The averaging is performed with respect to the fractal dimension of crystallites, and the distribution function over the individual crystallites for the fractal dimension is chosen in the Gaussian form:

$$\alpha_{av} = A(\beta)\int_0^{d_0}\alpha(d)\exp\left(-\frac{\alpha(d)^2}{2\beta^2}\right)dd, \qquad A(\beta) = \frac{1}{\beta\Phi(\alpha_0/\beta)}\sqrt{\frac{2}{\pi}}. \tag{1}$$

In expression (1), the sum over dimensions of all crystallites is replaced by the integral; $\alpha(d)$ is the CPA element of the individual crystallite; d is the fractal dimension of this crystallite; d_0 is the maximum fractal dimension for boundaries of grain contacts; the lower limit corresponds to a point contact; and $\beta \equiv \beta(T)$ is a characteristic parameter of the Gaussian distribution, which is defined by physical characteristics of a solid electrolyte and its surface. The quantity β is defined by quantities that can be measured independently of the CPA-element measurement:

* *Ural State University, pr. Lenina 51, Yekaterinburg, 620083 Russia*

** *Institute of Metal Physics, Ural Division, Russian Academy of Sciences, ul S. Kovalevskoĭ 18, Yekaterinburg, 620219 Russia*

1028-3358/00/4509-0439$20.00

$$\beta(T) = \frac{D(T)C(T)}{\sigma(T)S_{av}}, \quad (2)$$

where D is the diffusion coefficient, C is the capacitance at the surface of the electrolyte/electrode contact for the zero frequency, σ is the conductivity of the electrolyte, and S_{av} is the mean surface area of crystallites. If the dependence of the crystallite CPA element $\alpha(d)$ on its fractal dimension d is known, relationships (1) and (2) allow us to find the temperature dependence for a CPA element in the solid electrolyte. Comparing the temperature dependence of the CPA element with the experimental data, we can verify the correctness of the choice of the fractal model determining the dependence $\alpha(d)$ used for the theoretical description.

In [9], the temperature dependence of the CPA element was found for a fractal model, in which the relation between $\alpha(d)$ and d is determined by the scaling properties of effective capacitances ($C \sim S^{1+d}$, where S is the area of the effective capacitor with the capacitance C and d is the fractal dimension of the surface along the chosen direction). In this case, the fractal dimension of the surface determining the effective capacitance C is anisotropic (it has fractal characteristics in one direction and has usual nonfractal properties along another direction) and has a simple form $\alpha(d) = d$. In the fractal theories of CPA elements considered by the other authors [2–8], there are different $\alpha(d)$ dependences (in a statistical model of CPA elements, they can be considered as dependences of CPA elements on the fractal dimension found for individual crystallites). These dependences were obtained on the basis of other physical assumptions concerning the surface structure of the solid electrolyte/electrode contact. In the fractal theories of CPA elements developed by Pajkossy and Nyikos [2], the scaling properties $\xi^d C_j(1, \omega)$ are attributed to the admittance of the double electric layer at the electrode/sample boundary, which is described by a set of effective capacitances C_j and resistances R_j; here, ξ is a scaling factor and d is the fractal dimension of the contact surface (in our case of the surface of an individual crystallite) that results in the dependence $\alpha = \frac{1}{d-1}$.

The dependence $\alpha = \frac{d-1}{2}$ was also obtained by the other by Pajkossy and Nyikos in [3] on the basis of features of the ionic diffusion toward the fractal surface (also characterized by the fractal dimension d) for CPA elements. In the Liu theory [4], the fractal surface is modeled by the Cantor set formed as a product of two Cantor sets (of the "Cantor dust" type) at the segment. The theory applicable to a porous electrode with a cross section in the form of a Sierpinski gasket [8], etc., leads to the same results. The electric properties of such surfaces can be described by the equivalent hierarchical *RC*-circuit. In the theories indicated, the CPA element has a form $\alpha = 3 - d$. In the model of Le Mehaute and Crepy [5], fractal characteristics of a surface are chosen in such a way that they determine the scaling proportional to $\omega^{1/d}$ in the frequency domain (ω is the frequency, d is the fractal dimension) that results in the dependence $\alpha = \frac{1}{d}$. In the theories of Halsey [6] and of Ball and Blunt [7] for modeling fractal properties of a solid electrolyte surface, a superposition of one-dimensional waves sequentially imposed onto the plane surface is considered, starting from a certain minimum wavelength, which corresponds to the smallest size of the surface inhomogeneities (to the smallest scale of the self-similarity). This leads to the dependence of CPA elements on the fractal dimension in the form $\alpha = 5 - 2d$.

Here, we present the numerical calculations of temperature dependence for the CPA element with allowance for the measured temperature dependence of diffusion coefficient, capacitance, conductivity, and the mean area of crystallites, which enter into the expression for characteristic parameter β and allow us to write (2) in the form

$$\beta = \beta_0(T)\exp\left(-\frac{\Delta(b \times 10^3)}{T}\right),$$
$$\Delta b = \frac{E_a}{k \times 10^3}, \quad \beta_0(T) = \frac{\beta_0}{T^n}, \quad (3)$$

where β_0 and Δb are the parameters determined from the experimental dependences of diffusion, capacitance, and conductivity, and k is the Boltzmann constant. Note that we can introduce into (3) a numerical factor related to the technology of the sample preparation and its prehistory. All parameters entering into relationship (2) can be determined from experiments independently of impedance measurements for the CPA element. The choice of β in form (3) is convenient due to the fact that the temperature dependence of the parameters involved in $\beta(T)$ can be obtained not only from the measurements of impedance characteristics, but also from well-known theoretical formulas determining the diffusion coefficient, capacitance, and electric conductivity of solid electrolytes.

To reveal the effect of the fractal dimension of the crystallite surface on the temperature dependence of the CPA element, it is necessary to perform calculations of the temperature dependence of the CPA element for a solid electrolyte, for which the most comprehensive experimental data on the diffusion coefficient, capacitance, and conductivity entering into the parameter β are available [see (3)]. As an example of such a solid electrolyte, we choose a monocrystalline solid electrolyte Na + β-Al_2O_3 [10] and present here the calculations of the temperature dependence for a CPA element. In this case, we have the most complete experimental data to determine β according to formula (2) and these data

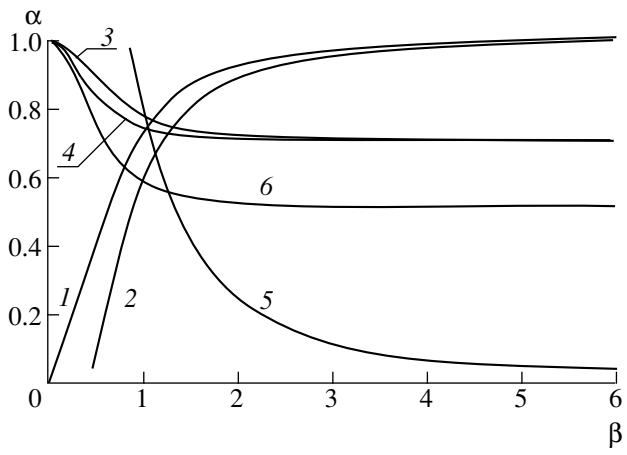

Fig. 1. Dependence of the CPA element α on the characteristic parameter β for different fractal theories: α = (*1*) *d*, (*2*) $\frac{d-1}{2}$, (*3*) $\frac{1}{d-1}$, (*4*) $\frac{1}{d}$, (*5*) 3 – *d*, (*6*) 5 – 2*d*.

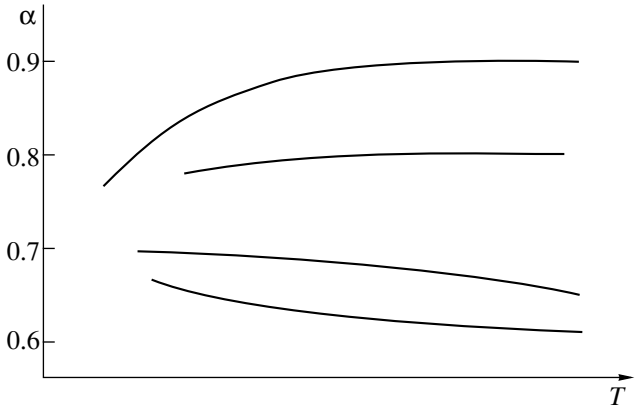

Fig. 2. Typical temperature dependences of the experimentally observed exponent for the constant-phase-angle element.

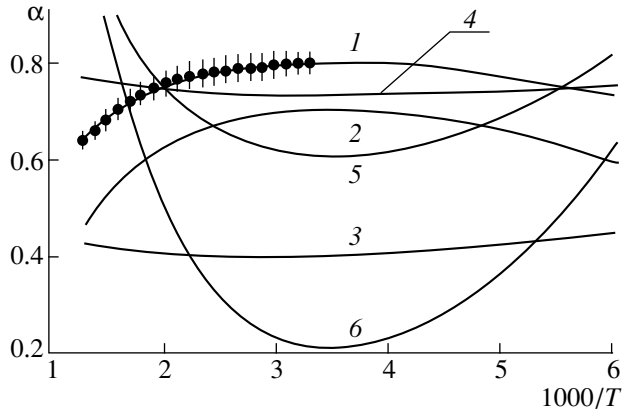

Fig. 3. Temperature dependence of the CPA element α for different fractal theories: α = (*1*) *d*, (*2*) $\frac{d-1}{2}$, (*3*) $\frac{1}{d-1}$, (*4*) $\frac{1}{d}$, (*5*) 3 – *d*, (*6*) 5 – 2*d* for $\beta_0 = 937$ K and $E_a = 0.024$ eV corresponding to experiment [10]; experimental data of [10] are denoted by dots.

were obtained using the same sample. The plots of CPA element α versus parameter β entering (1) are shown in Fig. 1.

3. TEMPERATURE DEPENDENCE OF CPA ELEMENTS

Experimental data obtained by studying CPA elements of solid electrolytes using the impedance techniques in a wide frequency range (10^2–10^5 Hz) demonstrate the existence of different types of temperature dependence for a CPA element (Fig. 2). For some electrolytes, the CPA element decreases with the growth of temperature [10]; for other electrolytes, it increases [11] or remains nearly constant [12]. Temperature dependence of CPA elements for the fractal theories listed above are given in Fig. 3. Correlation of the character of CPA elements for various fractal theories of CPA elements [2–9], with assumptions concerning the character of the fractal structure of the surface, which are in the basis of these theories, allows us to make certain conclusions about the type of fractal structure of the electrolyte surface. These conclusions are based on the comparison with the experimental data on CPA elements. Thus, the theory [9], in which the fractal surface is anisotropic, agrees better with the experimental results for Na + β-Al_2O_3 electrolyte. Analysis of curves in Fig. 3, which is based on the form of temperature dependences, provides an opportunity to reveal the character of surface fractal structures (distribution of clusters) affecting the behavior of CPA elements.

CONCLUSIONS

We extended to a finite temperature range a number of main fractal theories for CPA elements, which do not describe the temperature dependence. We compared the theoretical temperature dependences for CPA elements obtained in the framework of the theories under study with the experimental curves for CPA elements. This comparison allows us to use the measured temperature dependences of CPA elements in various theories to reveal the fractal features of the electrolyte/electrode contact surface and, thus, to estimate and, possibly, to monitor their physical properties.

ACKNOWLEDGMENTS

We are grateful to participants of the seminar held by the Chair of low-temperature physics (Ural State University) for valuable discussions on the results.

This work was partially supported by the Russian Foundation for Basic Research, project no. 00-02-16285.

REFERENCES

1. B. B. Mandelbrot, *The Fractal Geometry of Nature* (Freeman, New York, 1982).

2. T. Pajkossy and L. Nyikos, Electrochim. Acta **30**, 1533 (1985).
3. T. Pajkossy and L. Nyikos, Electrochim. Acta **31**, 1347 (1986).
4. S. H. Liu, Phys. Rev. Lett. **55**, 529 (1985).
5. A. Le Mehaute and G. Crepy, Solid State Ionics **9**/**10**, 17 (1983).
6. T. C. Halsey, Phys. Rev. A **36**, 5877 (1987).
7. R. Ball and M. Blunt, J. Phys. A **21**, 197 (1988).
8. B. Sapoval, Solid State Ionics **23** (4), 253 (1987).
9. L. Ya. Kobelev, Ya. L. Kobelev, V. L. Kobelev, and O. L. Kobeleva, Élektrokhimiya **35**, 294 (1999).
10. H. Engstrom, J. B. Bates, and J. C. Wang, Solid State Commun. **35**, 543 (1980).
11. D. I. Bronin and B. L. Kuzin, in *Proceedings of the All-Union School on Electrochemistry* (Sverdlovsk, 1991), Vol. 1, p. 135.
12. S. N. Shkerin, Élektrokhimiya **30**, 1086 (1994).

Translated by T. Galkina

Doklady Physics, Vol. 45, No. 9, 2000, pp. 443–445. Translated from Doklady Akademii Nauk, Vol. 374, No. 2, 2000, pp. 184–186.

PHYSICS

Classical Autoionization of a Relativistic Two-Electron Atom

D. U. Matrasulov and Corresponding Member of the RAS P. K. Khabibullaev

Received May 5, 2000

Recently, properties of highly excited atoms have been subjected to intense study by methods of classical nonlinear dynamics [1–3]. One of the most interesting phenomena observed when studying the interaction of a Rydberg atom with a monochromatic electromagnetic field is the stochastization of the classical-electron motion, which results in the stochastic (or diffusion) ionization of the atom [4]. Use of stochastic-dynamics methods, in particular, the Chirikov stochasticity criterion, allows us to quite easily estimate the critical value of the external field corresponding to the onset of stochastization in analytical form.

A similar stochastization process is also possible in the case of a two-electron atom even in the absence of the external field [6]. The motion of an external electron can become stochastic due to the interaction with an internal electron. The field of the periodically moving internal electron is a periodical perturbance for the motion of the external electron. Thus, the mechanism of the resulting stochastic autoionization is similar to that of the stochastic ionization of a single-electron atom in the monochromatic field: under the action of periodic perturbances of the internal electron, the external electron can pass to more highly excited orbits and, as a result, approach infinity.

This autoionization mechanism was studied for the first time in [6]. In [7], a similar mechanism for autoionization of molecular Rydberg states was considered. In the present paper, we generalize the results of [6] for the case of a relativistic atom. It should be noted that, to date, the study of determinate systems with chaotic dynamics was constrained, as a rule, by the consideration of nonrelativistic ones. Relativistic systems were studied in only a few papers (see [8–10]). In [11], stochastic ionization of a relativistic hydrogenlike atom in a monochromatic field was considered.

Prior to considering the stochastic autoionization of a relativistic two-electron atom, we present a brief description for the relativistic Keplerian motion in terms of the action–angle variables. Henceforth, we use a system of units in which $m_e = \hbar = c = 1$. We also assume for simplicity that both electrons move in the same plane. The Hamiltonian for a relativistic three-dimensional single-electron atom in the action–angle variables has the form [12]

$$H_0 = \left[1 + \frac{Z^2\alpha^2}{(n - M + \sqrt{M^2 - Z^2\alpha^2})}\right]^{-1/2}, \qquad (1)$$

where $n = I_r + I_\phi + I_\theta$, $M = I_\phi + I_\theta$, I_r is the radial component, I_ϕ and I_θ are angular components of the action, and $\alpha = 1/137$.

The equation for the trajectory of a relativistic Keplerian electron has the form [13]

$$\frac{p}{r} + e\cos q\Phi = 1, \qquad (2)$$

where

$$p = \frac{M^2 - Z^2\alpha^2}{EZ\alpha},$$
$$q = \sqrt{1 - \frac{Z^2\alpha^2}{M^2}}, \quad e = \sqrt{1 - \frac{M^2 - Z^2\alpha^2}{n^2}}, \qquad (3)$$

and E is the electron energy.

The presence of the factor q shows that the trajectory of the Keplerian electron is nonclosed [13]. In the case of

$$M \gg Z\alpha = \frac{Z}{137}, \qquad (4)$$

the Hamiltonian (1) can be written out as

$$H_0 = \left[1 + \frac{Z^2\alpha^2}{(n - M + M)^2}\right]^{-1/2} \approx \frac{n}{\sqrt{n^2 + Z^2\alpha^2}}. \qquad (5)$$

In this approximation, $q \approx 1$ and the trajectories become closed. The radius r and polar angle ϕ can be expressed in terms of the action–angle variables in the following form:

$$r = \frac{n\sqrt{n^2 + Z^2\alpha^2}}{Z}(1 - e\cos\psi), \qquad (6)$$

Department of Thermal Physics,
Academy of Sciences of the Republic of Uzbekistan,
ul. Katartal 28, Chilanzar, Tashkent, 700135 Uzbekistan

1028-3358/00/4509-0443$20.00

$$\cot\phi = \frac{n}{\gamma}\tan\frac{\psi}{2}, \quad (7)$$

where $\gamma = \sqrt{M^2 - Z^2\alpha^2}$.

We now consider a relativistic two-electron atom. We assume for simplicity that both electrons move in the same plane. The electrons interact with an atomic nucleus having the charge $Z\alpha$. The Hamiltonian of this two-electron atom can be written out as

$$H = T_1 - \frac{Z}{r_1} + T_2 + \frac{Z}{r_2} + \frac{1}{|\mathbf{r}_1 - \mathbf{r}_2|}. \quad (8)$$

Here, T_i are the kinetic energies of the relativistic electrons and r_1 and r_2 are distances between the atomic nucleus and the external and internal electrons, respectively. The last term in expression (8) describes the interelectron repulsion. Assuming $r_1 \ll r_2$, we write out this term in the form

$$\frac{1}{|\mathbf{r}_1 - \mathbf{r}_2|} \approx \frac{1}{r_1} - \frac{\mathbf{r}_1\mathbf{r}_2}{r_2^3}. \quad (9)$$

Substituting (9) into (8), we obtain

$$T_1 - \frac{Z}{r_1} + T_2 + \frac{Z'}{r_2} + V, \quad (10)$$

where

$$V = \frac{\mathbf{r}_1\mathbf{r}_2}{r_2^3}\cos(\phi_1 - \phi_2),$$

$Z' = Z - 1$, and ϕ_1, ϕ_2 are azimuth angles of the electrons in the plane of their motion.

In order to simplify further calculations, we assume, following [6], that the internal electron moves in a circular orbit, i.e., without the eccentricity. Then, we have from (6)

$$r_1 = \frac{n_1\sqrt{n_1^2 + Z^2\alpha^2}}{Z}, \quad (11)$$

$$\phi = \omega_1 t = \frac{Z^2\alpha^2}{(n_1^2 + Z^2)^{2/3}}. \quad (12)$$

Admitting, as in [6], that $M_2/I_2 \ll 1$ and $\cos\psi \approx 1$, we can obtain for the external electron

$$r_2 = \frac{2n_2\sqrt{n_2^2 + Z'^2\alpha^2}}{Z'}\left(\sin^2\frac{\psi}{2} + \frac{a^2}{4}\right),$$

where $a = \gamma^2/n_2^2$.

Thus, the perturbance can be written out in the form

$$V = \frac{Z'^2\alpha^2}{4n_2^2(n_2^2 + Z^2\alpha^2)}r_1\left(\sin^2\frac{\psi}{2} + \frac{a^2}{4}\right)^{-2}\cos\omega t.$$

Using the Fourier expansion for the dipole moment (see [6])

$$d = \sin^2\left(\frac{\psi}{2} + \frac{a^2}{4}\right)^{-2} = \sum d_k\cos(k\theta_2),$$

where $d_k = 26.3/(a^6k^{5/3})$, we can rewrite the complete Hamiltonian as

$$H = \frac{n_2}{\sqrt{n_2^2 + Z'^2\alpha^2}} + \epsilon\cos\omega_1 t\sum d_k\cos(k\theta_2), \quad (13)$$

where

$$\epsilon = \frac{Z'^2\alpha^2}{4n_2^2(n_2^2 + Z^2\alpha^2)}r_1.$$

This Hamiltonian is equivalent to that describing the interaction of a relativistic hydrogen-like atom with a monochromatic field. For the resonance-curve width (see [11]), we have

$$\Delta\omega = 2\left(2\frac{\omega}{dn}r_1r_2d_k\right)^{1/2}. \quad (14)$$

The distance between the resonances is determined to be

$$\delta\omega = \frac{\omega_1}{k^2}. \quad (15)$$

The Chirikov criterion for overlapping the resonances can be written out in the form [6]

$$2.5\frac{\Delta\omega}{\delta\omega} > 1.$$

Using (14) and (15), we obtain from this criterion the condition (in terms of the action and angle) for the onset of the stochastization of the external electron, which results in diffusion ionization:

$$400Z'^{-2/3}Z^{-1/3}n_1n_2^5\gamma^{-6} > 1. \quad (16)$$

Similarly to [6, 11], we can calculate the diffusion coefficient

$$D = \frac{\pi}{2}\frac{r_1^2r_2^{-4}k^2d_k^2}{\omega_2^2}.$$

Expressing r_1, r_2, d_k, and ω_2 in terms of the charge and action, we obtain

$$D \approx D_{\text{nonrel}}\left(1 + 3\frac{Z^2\alpha^2}{n_1^2}\right)\left(1 + 6\frac{Z^2\alpha^2}{M_2^2}\right)\left(1 - \frac{Z'^2\alpha^2}{n_2^2}\right), \quad (17)$$

where

$$D_{\text{nonrel}} \approx \frac{68Z'^{8/3}Z^{-14/3}n_1^8n_2^6}{M_2^{12}}$$

is the diffusion coefficient corresponding to a nonrelativistic atom.

As is seen from (17), the relativistic corrections to the diffusion coefficient are caused by three factors: The first correction arises due to increasing the rotation frequency for the internal electron in the relativistic case and can be rather significant. The second one is associated with the ratio $Z\alpha/M_2$, which can also be significant at low values of the orbital moment. Finally, the third correction appears due to the relativistic nature of the external-electron motion. This last correction is negligible for highly excited states.

The ionization probability per time unit is given by the relation

$$\Gamma = \frac{2D}{n_2^2} \approx \Gamma_{\text{nonrel}}\left(1 + 3\frac{Z^2\alpha^2}{n_1^2}\right)$$
$$\times\left(1 + 6\frac{Z^2\alpha^2}{M_2^2}\right)\left(1 - \frac{Z'^2\alpha^2}{n_2^2}\right).$$

Thus, we have studied the stochastization of a relativistic two-electron atom, which results in its diffusion autoionization. The formulas obtained show that, in the relativistic case, corrections to the diffusion coefficient, probability, and time of ionization can be significant (in contrast to the case of a relativistic atom placed in a monochromatic field [11]). It should be noted that, in the case under consideration, we assumed that $M \gg Z\alpha$. In the case of $M > Z\alpha$, the Hamiltonian (1) becomes imaginary, and a necessity appears to take into account the finite size of the atomic nucleus [14, 15].

REFERENCES

1. N. B. Delone, V. P. Kraĭnov, and D. L. Shepelyanskiĭ, Usp. Fiz. Nauk **140**, 355 (1983) [Sov. Phys. Usp. **26**, 551 (1983)].
2. R. V. Jensen, Phys. Rev. A **30**, 386 (1984).
3. G. Casati, I. Guarneri, and D. L. Shepelyansky, IEEE J. Quantum Electron. **24**, 1420 (1988).
4. J. E. Bayfield and P. M. Koch, Phys. Rev. Lett. **33**, 258 (1974).
5. R. V. Jensen, S. M. Sussckind, and M. M. Sanders, Phys. Rep. **201**, 1 (1991).
6. A. L. Belov and V. P. Kraĭnov, Zh. Éksp. Teor. Fiz. **92**, 456 (1987) [Sov. Phys. JETP **65**, 257 (1987)].
7. F. Benvenuto, G. Casati, and D. L. Shepelyansky, Phys. Rev. Lett. **72**, 1818 (1994).
8. A. A. Chernikov, T. Tel, G. Vattay, and G. M. Zaslavsky, Phys. Rev. A **40**, 4072 (1989).
9. D. G. Luchinsky, P. V. McClintock, and A. B. Neiman, Phys. Rev. E **53**, 4240 (1996).
10. Kim Jung-Hoon and Lee Hai-Woog, Phys. Rev. E **53**, 4242 (1996).
11. D. U. Matrasulov, V. I. Matveev, and P. K. Khabibullaev, Dokl. Akad. Nauk **367**, 321 (1999) [Dokl. Phys. **44**, 420 (1999)].
12. M. Born, *The Mechanics of the Atom* (G. Bell and Sons, London, 1927; ONTI, Moscow, 1934).
13. L. D. Landau and E. M. Lifshitz, *The Classical Theory of Fields* (Nauka, Moscow, 1973; Pergamon, Oxford, 1975).
14. V. D. Mur and V. S. Popov, Yad. Fiz. **28**, 837 (1978) [Sov. J. Nucl. Phys. **28**, 429 (1978)].
15. V. S. Popov, D. N. Voskresenskiĭ, V. L. Eletskiĭ, and V. D. Mur, Zh. Éksp. Teor. Fiz. **76**, 431 (1979) [Sov. Phys. JETP **49**, 218 (1979)].

Translated by G. Merzon

Doklady Physics, Vol. 45, No. 9, 2000, pp. 446–448. Translated from Doklady Akademii Nauk, Vol. 374, No. 3, 2000, pp. 321–323.

PHYSICS

"Tunneling" of Autowaves

A. Yu. Dovzhenko, S. V. Maklakov, and É. N. Rumanov

Presented by Academician A.G. Merzhanov December 27, 1999

Received December 12, 1999

To ensure the propagation of an autowave in an active medium, parameters of this medium should exceed certain threshold values. Such a threshold was first found by Ya.B. Zel'dovich [1] as applied to combustion waves. The problem concerning this wave with the heat loss taken into account has two solutions: the steady-state and the non-steady-state. The merging of these solutions corresponds to the propagation threshold; there are no wave solutions below the threshold. Later on, a similar threshold was found for the model of a nerve impulse [2, 3] and other autowaves [4]. In this paper, we study the propagation of autowaves in a subthreshold region of a finite length. It is shown that the length of the region passed by the autowave can exceed its wavelength by much more than a factor of ten.

We will characterize the active medium by parameter d with a threshold value d_{th}. Let $d(x < 0) = d_1 > d_{\text{th}}$, $d(0 < x < x_0) = d_2 < d_{\text{th}}$, and $d(x > x_0) = d_3 > d_{\text{th}}$. A solitary wave traveling from the left to the right has in the region $x < 0$ a constant amplitude and velocity. Then, it decays at the subthreshold region. Can such a damping excitation initiate a wave propagation in the region $x > x_0$? To answer this question, we consider the simplest case, namely, a wave of exothermal reaction, which propagates along a tube with a narrow region in which the diameter is smaller than the threshold diameter. The reaction is accelerated with temperature according to the activation law $\exp(-E/T)$. The wave propagates uniformly in the tube with a constant diameter; its velocity u and amplitude (a peak temperature) T can be found on the basis of approximate equalities [1]:

$$(T_b - T_0)u = (k_+ - k_-)(T - T_0),$$
$$k_+ \approx u\left[1 + \left(\frac{\chi}{ud}\right)^2\right], \quad k_- \approx -u^{-1}\left(\frac{\chi}{d}\right)^2, \tag{1}$$

$$\left(\frac{u_0}{u}\right)^2 = \exp[ET_b^{-2}(T_b - T)]. \tag{2}$$

Here, $T_b = T_0 + Qc^{-1}$, T_0 is the temperature of the surrounding medium, Q is the heat of reaction, c is the specific heat of the reacting mixture, χ is its heat diffusivity, d is the effective diameter of the tube (with account of the features of the heat exchange, the Nusselt number, etc.), and u_0 is the wave velocity as $d \longrightarrow \infty$. In (1), we took into account that the ratio $\chi(ud)^{-1}$ is small at $d \geq d_{\text{th}}$. In the narrow region (in a reference system linked to the wave), balance (1) is violated and the reaction heat becomes insufficient to counterbalance the heat dissipation; hence, amplitude T decreases. If, as we assume below, the difference $d - d_{\text{th}}$ is small at this region, the quasi-steady-state approximation is valid: kinetic coupling (2) between u and t is retained, and, instead of (1), we have

$$a\left(\frac{dT}{dt}\right) = (T_b - T_0)u - (k_+ - k_-)(T - T_0). \tag{3}$$

The dependence of k_+, k_- on u is taken in a previous form and a is the characteristic spatial scale of the temperature variation (the effective width of the wave).

Eliminating T from (2) and (3) and passing to the new variables

$$a\xi = \int^t u(t')dt', \quad v = \left(\frac{u_0}{u}\right)^2, \tag{4}$$

we obtain

$$\frac{dv}{d\xi} \approx \frac{v}{2}(Z\delta v - \ln v), \tag{5}$$

where $\delta = (2\chi/u_0 d)^2$ and $Z = E(T_b - T_0)T_b^{-2}$ is Zel'dovich's number. In (5), only the main terms in small parameters δ and Z^{-1} are retained. The merging of steady-state solutions (5) occurs at $\delta_{\text{th}} = 2(Ze)^{-1}$. For a tube with a narrow region, we write

$$\delta(x) = \delta_{\text{th}}(1 + \delta_i), \quad i = 1, 2, 3, \tag{6}$$

and $\delta_2 > 0$, δ_1 and δ_3 being negative.

Assuming $v = e(1 + w)$, we have instead of (5)

$$\frac{dw}{d\xi} = \delta_i + \frac{w^2}{2}. \tag{7}$$

Institute of Structural Macrokinetics and Problems of Materials Science, Russian Academy of Sciences, Moscow oblast, Chernogolovka, 142432 Russia

1028-3358/00/4509-0446$20.00

When the wave approaches the narrow region, its velocity corresponds to the steady-state solution for region *1*, $w = w_- = -\sqrt{-2\delta_1}$. On the other hand, the non-steady-state solution for region *3*, $w_+ = \sqrt{-2\delta_3}$, can be considered as the boundary of the basin of attraction for the steady-state solution in this region. Therefore, the length of the narrow region $x_0 = a\xi_0$, at which the wave can penetrate region *3* and attain there a steady-state mode of the uniform motion, is limited by the condition

$$\xi_0 < \xi_m = \sqrt{\frac{2}{\delta_2}}\left(\arctan\sqrt{-\frac{\delta_1}{\delta_2}} + \arctan\sqrt{-\frac{\delta_3}{\delta_2}}\right). \quad (8)$$

It is essential that any indications of the specific parameters characterizing this model (exothermal reaction) disappear from relationships (7) and (8). These formulas take into account only the parabolicity of $\delta(v)$ near the threshold (the coincidence of the steady-state and non-steady-state branches); thus condition (8) is valid for any autowave. Quasi-steady-state Eq. (3) is valid if the wave velocity varies only slightly at distances on the order of $\sim a$. With the help of (7), we obtain the estimate (bearing in mind the subthreshold region in which $\delta > \delta_{th}$)

$$\frac{\Delta u}{u_0} \sim \frac{\delta}{\delta_{th}} - 1.$$

Thus, our consideration is valid at small distances from the threshold, as it was assumed above.

The wave propagation in the subthreshold region was also studied by computer simulation. We used the set of equations

$$\frac{\partial\theta}{\partial\tau} = \frac{\partial^2\theta}{\partial\xi^2} + (1-\eta)\exp\left[-\frac{Z(1-\theta)}{\theta + \epsilon(1-\theta)}\right] - \delta\theta, \quad (9)$$

$$\frac{\partial\eta}{\partial\tau} = (1-\eta)\exp\left[-\frac{Z(1-\theta)}{\theta + \epsilon(1-\theta)}\right], \quad (10)$$

which describe the exothermal reaction and the heat transfer. As a time scale t_s, we take the time of reaction for the temperature T_b. Here, the length scale is $x_s = \sqrt{\chi t_s}$, temperature θ is measured from T_0 in units of $T_b - T_0$, η is the concentration of the reaction product, and $\epsilon = T_0 T_b^{-1}$. The calculation was performed for $\delta_1 = \delta_3$, $\epsilon = 0.23077$, and $Z = 7.6923$ (so that $\delta_{th} \approx 0.09565$). We used the implicit difference scheme with a variable step in ξ at large $\frac{\partial\theta}{\partial\xi}$. As the initial condition within the range $0 < \xi < 150$, we took the solution corresponding to the steady-state wave. The dependence of ξ_m on δ_2 for four values of δ_1 is shown in Fig. 1. The "non-regular" behavior seems likely to be caused by the low stability of calculations near the threshold, where even small variations of δ induce a significant variation in the wave velocity. A comparison with (8) allows us to estimate the value of a in (3), $a \sim \sqrt{\chi t_s}$. According to Fig. 1, the autowave can overcome the subthreshold region, whose length exceeds its own size by much more than a factor of ten. The length ξ_m decreases with the increase in δ_2. The computer simulations demonstrated a faster decrease than that following from the asymptotic (in terms of δ_2) estimate (8). At the same time, the curves come closer together at $-\delta_1 \gg \delta_2$, and this fact agrees well with (8). A more detailed comparison with this formula will be given after the accumulation of data and their statistical treatment.

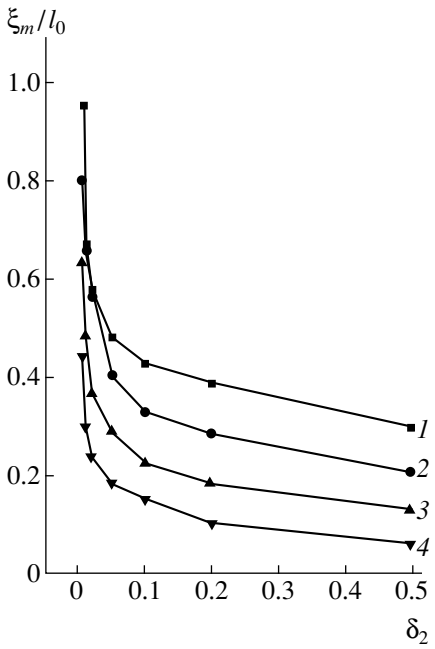

Maximum length ξ_m of the region passed by the autowave as a function of δ_2. δ_1 = (*1*) 0.5, (*2*) 0.2, (*3*) 0.1, and (*4*) 0.01.

Certainly, the similarity of this phenomenon with quantum tunneling is rather limited. During tunneling, the amplitude of the passed wave is always smaller than the amplitude of the incident wave (except in the case of reflectionless barriers [5]). In an active medium, the feed after passing the "barrier" results in the complete restoration of the initial amplitude. The damping of autowaves is caused by a dissipation rather than by a reflection. At the same time, the ability to penetrate through the "unattainable" regions can form a basis of the method for the study of nonuniform active media (just as with tunnel microscopy and spectroscopy).

The "tunneling" sends us back to the analysis of measurements concerning the threshold of the autowave propagation. A two-dimensional or three-dimensional active medium having mean values of parameters close to threshold, should consist of chaotically located above-threshold and subthreshold regions. Wave propagation in such a medium is a percolation process [6]. Owing to tunneling, the threshold lowers

since it is sufficient to have small but closely located clusters instead of a continuous cluster penetrating the entire system. Near the threshold, the consumption of an activator feeding the wave should vary depending on the random tunnel contacts.

ACKNOWLEDGMENTS

This work was supported by the Russian Foundation for Basic Research, project no. 98-03-32132a.

REFERENCES

1. Ya. B. Zel'dovich, Zh. Éksp. Teor. Fiz. **11**, 159 (1941).
2. B. C. Casten, H. Cohen, and P. A. Lagerstrom, Q. Appl. Math. **32**, 305 (1975).
3. A. V. Kudryashov and V. G. Yakhno, in *Dynamics of Biological Systems* (Gorki, 1978), Vol. 2, p. 15.
4. A. G. Merzhanov and E. N. Rumanov, Rev. Mod. Phys. **71**, 1173 (1999).
5. S. Novikov, S. V. Manakov, L. P. Pitaevskii, and V. E. Zakharov, *Theory of Solitons: The Inverse Scattering Method* (Nauka, Moscow, 1980; Consultants Bureau, New York, 1984).
6. A. Yu. Dovzhenko and É. N. Rumanov, in *Chemical Physics of Combustion and Explosion* (Chernogolovka, 1996), Vol. 1, Part 2, p. 209.

Translated by T. Galkina

Doklady Physics, Vol. 45, No. 9, 2000, pp. 449–453. Translated from Doklady Akademii Nauk, Vol. 374, No. 1, 2000, pp. 35–39.

TECHNICAL PHYSICS

Synthesis of Plane Radiating Systems on the Basis of Atomic Functions

E. G. Zelkin*, V. F. Kravchenko*,
Corresponding Member of the RAS V. I. Pustovoĭt, and V. V. Timoshenko****

Received December 10, 1999

In this paper, proceeding from the notions and results obtained in [1–4], we propose a new mathematical method based on the theory of atomic functions, which is applicable to problems of synthesizing plane radiating antennas. According to [1], the following relations hold for a rectangular antenna (see Fig. 1):

$$N_x(\alpha, \beta) = \iint_S F_x(x, y) e^{ik(x\sin\alpha + y\sin\beta)} dx\, dy,$$
$$N_y(\alpha, \beta) = \iint_S F_y(x, y) e^{ik(x\sin\alpha + y\sin\beta)} dx\, dy. \quad (1)$$

We describe the directivity pattern as a function of the angles α and β (i.e., the angles between the direction to the observation point and the *xy* and *yz* planes, respectively):

$$\sin\beta = \sin\theta\sin\psi, \quad \sin\alpha = \sin\theta\cos\psi. \quad (2)$$

We assume that

$$\mu = \frac{L}{\lambda}\sin\alpha, \quad \eta = \frac{L}{\lambda}\sin\alpha,$$
$$t_1 = \frac{2\pi x}{L}, \quad t_2 = \frac{2\pi y}{L}, \quad R_{x,y} = N_{x,y}L^2. \quad (3)$$

In this case, we have the equation

$$R(\mu, \eta) = \frac{1}{(2\pi)^2}\int_{-\pi}^{\pi}\int_{-\pi}^{\pi} F(t_1, t_2) e^{i(t_1\mu + t_2\eta)} dt_1\, dt_2,$$
$$\mu, \eta \in \left[-\frac{L}{\lambda}, \frac{L}{\lambda}\right]. \quad (4)$$

Here, $R(\mu, \eta)$ is the directivity pattern for a plane radiating system (the polarization indices *x* and *y* are omitted) and *L* is the characteristic scale for the opening. When solving the problem of synthesizing the directivity pattern for the plane antenna mouth given by (4), it is important to specify the conditions that must be satisfied by the directivity pattern in order to be exactly reproducible. A directional diagram $R(\mu, \eta)$ is realizable if it satisfies the Plancherel–Polya theorem [2]. In this case, the field distribution over the antenna mouth is related to the directivity pattern by the inverse Fourier transformation

$$F(t_1, t_2) = \int_{-\infty}^{\infty}\int_{-\infty}^{\infty} R(\mu, \eta) e^{-i(t_1\mu + t_2\eta)} d\mu\, d\eta, \quad (5)$$

where $R(\mu, \eta) \in W_{\pi,\pi}$ belongs to the class of entire functions of the exponential type with the index π. The antenna-mouth field $F(t_1, t_2)$ must satisfy the radiation condition [3]. The function $F(t_1, t_2)$ and its derivative are continuous everywhere and vanish at the mouth boundary:

$$F(t_1, t_2)|_{\partial S} = 0, \quad dF(t_1, t_2)|_{\partial S} = 0. \quad (6)$$

Statement of the problem and the method for its solution. Let the directivity pattern $R_0(\mu, \eta)$ be given,

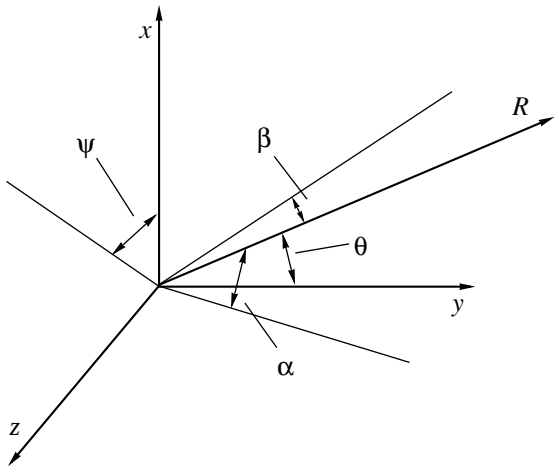

Fig. 1. Coordinate system in the problem of synthesizing the directivity pattern for the plane radiating antenna.

* *Institute of Radio Engineering and Electronics, Russian Academy of Sciences, ul. Mokhovaya 11, Moscow, 103907 Russia*
** *Scientific and Technological Center of Unique Instrument Making, Russian Academy of Sciences, ul. Butlerova 15, Moscow, 117342 Russia*

1028-3358/00/4509-0449$20.00

which, possibly, is unrealizable and does not satisfy radiation conditions (6). A realizable directivity pattern $R(\mu, \eta)$ satisfying the radiation conditions and having the minimum root-mean-square deviation from the values $R_0(\mu_m, \eta_n)$ at the given points μ_m and η_n must be constructed. We also require that the lateral lobes of the directivity pattern $R(\mu, \eta)$ have low intensities tending exponentially to zero as $|\mu| \longrightarrow \infty$ and $|\eta| \longrightarrow \infty$. We construct the directivity pattern $R(\mu, \eta)$ satisfying these conditions as a series of Fourier transforms for the atomic functions [4–11]:

$$R(\mu, \eta) = \sum_k \sum_p a_{kp} \Phi(\mu - kd) \Phi(\eta - pd). \quad (7)$$

Here, $\Phi(\mu)$ is the Fourier transform of the atomic function, d is the net step, and the coefficients a_{kp} are determined from the minimum condition for the functional

$$\sum_{m, n} (R_0(\mu_m, \eta_n) - R(\mu_m, \eta_n))^2 \longrightarrow \min. \quad (8)$$

In this case, the Fourier transform of the atomic function takes the form of an infinite product:

$$\Phi(z) = \prod_{n=1}^{\infty} \frac{T(za^{-n})}{P(za^{-n})}, \quad (9)$$

where $T(z)$ and $P(z)$ are trigonometric and algebraic polynomials, respectively. The lateral lobes of the Fourier transforms for the atomic functions have low intensities tending to zero more rapidly than an arbitrary power $|z|^{-k}$ as $|z| \longrightarrow \infty$ (properties of atomic functions or weight windows are thoroughly studied in [10]). For example, the intensity of the lateral lobes for the function

$$\mathrm{Up}(z) = \prod_{k=1}^{\infty} \frac{\sin(2^{-k}z)}{2^{-k}z}, \quad (10)$$

which is the Fourier transform of the simplest atomic function $\mathrm{up}(x)$, is ten times as low as the function $(\sin z)/z$ widely applied to problems of synthesizing antennas. Approximating properties of the Fourier transforms for the atomic functions were studied in [4, 9, 11]. It was proven in these papers that the directivity pattern of a linear antenna with a length of 2π can be interpolated by the series

$$R(\mu) = \sum_k R_0(2k) \mathrm{Up}(\pi(\mu - 2k)). \quad (11)$$

In this case, the approximation of the desired directivity pattern $R_0(\mu)$ is better (with respect to both root-mean-square and uniform deviations) than that given by the series

$$S(\mu) = \sum_k R_0(k) \frac{\sin(\pi(\mu - k))}{\pi(\mu - k)}. \quad (12)$$

The approximating properties of the Fourier transforms for the atomic functions can be improved by decreasing the main-lobe width and lowering the intensity of its lateral lobes. We can do this, for example, by multiplying the function $\mathrm{Up}(\pi z)$ by the algebraic polynomial [10]:

$$W(\mu; b) = \mathrm{Up}(\pi\mu)(1 - b\mu^2). \quad (13)$$

The function $W(\mu)$ obtained belongs to the class of atomic functions, because its Fourier transform can be written in the form

$$w(t; b) = \int_{-\infty}^{\infty} W(\mu) e^{-i\mu t} d\mu = 2\left(\mathrm{up}(t/\pi) + b \frac{d^2 \mathrm{up}(t/\pi)}{dt^2}\right). \quad (14)$$

By properly choosing the parameter b, we can significantly decrease the intensity of the lateral lobes and, thereby, improve the approximating properties of the series

$$R(\mu; b) = \sum_k R_0(2k) W(\mu - 2k; b). \quad (15)$$

The synthesis of the directivity pattern for a plane radiating system can be carried out with the help of the two-dimensional generalization of interpolating series (15):

$$R(\mu, \eta) = \sum_m \sum_n R_0(2m, 2n) W(\eta - 2n; b) W(\mu - 2m; b). \quad (16)$$

It follows from (5) and (14) that directivity pattern (16) corresponds to the field distribution

$$F(t_1, t_2) = 4\left(\mathrm{up}(t_1/\pi) + b \frac{d^2 \mathrm{up}(t_1/\pi)}{dt_1^2}\right) \times \left(\mathrm{up}(t_2/\pi) + b \frac{d^2 \mathrm{up}(t_2/\pi)}{dt_2^2}\right) \sum_m \sum_n a_{mn} e^{-2i(nt_1 + mt_2)} \quad (17)$$

over the mouth, which is an amplitude modulation of the atomic functions for a superposition of running waves with the amplitudes a_{mn} and the phase velocities $2m$ and $2n$ along the coordinates t_1 and t_2, respectively.

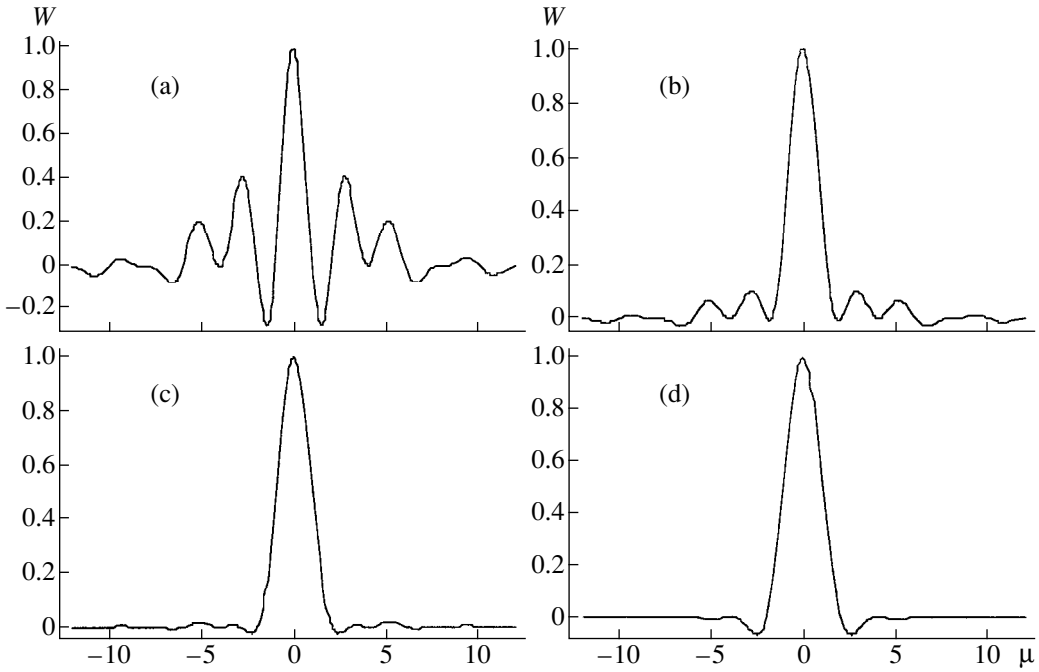

Fig. 2. Plots for atomic function (13). The parameter b is equal to (a) 1, (b) 1/3, (c) 1/9, and (d) 0.

Numerical simulation. We carried out a comparative analysis of atomic function (13) as a partial directivity pattern. The atomic functions are shown in Fig. 2a for $b = 1$, in Fig. 2b for $b = 1/3$, in Fig. 2c for $b = 1/9$, and in Fig. 2d for $b = 0$. We determine the following characteristics of the directivity pattern: the coefficient of directional action (CDA), the main-lobe half-width (*W1*) with respect to the radiation intensity, the main-lobe width (*W2*) with respect to the zero radiation intensity, the intensity level (*W3*) of the first lateral lobe, and the asymptotic rate of damping

$$W4 = 10\log\lim_{\mu\to\infty}\left(\frac{W(2\mu)}{W(\mu)}\right)^2$$

for the lateral lobes. Our analysis of the results obtained (Table 1) suggests that both the shape of the directivity pattern and its basic characteristics can be efficiently controlled by varying the parameter b of function (13). It follows from Table 2 that, provided that the parameter b is properly chosen, the directivity pattern can be obtained satisfying radiation conditions (6) and has an infinite rate of damping for its lateral lobes. We analyzed approximating properties of series (15). As a desired directivity pattern, we chose the function

$$R_0(\mu) = \begin{cases} 0, & |\mu| > 6 \\ 1, & -6 \le \mu < 0 \\ 1 - x/3, & 0 \le \mu < 6. \end{cases} \qquad (18)$$

The desired directivity pattern was approximated by (15) (for $b = 0$ and 1/9) and also by both formula (18) and the series

$$R_T(\mu) = \sum_k R_0(2k)\left(\frac{\sin(\pi(\mu-2k)/2)}{\pi(\mu-2k)/2}\right)^2 \qquad (19)$$

corresponding to the field distribution over the mouth with a triangular form of the amplitude modulation. The approximation results obtained according to formulas (15), (12), and (19) for directivity pattern (18) are shown in Fig. 3. Numerical errors of this approximation are listed in Table 3. Here,

$$A1[R] = 100\sqrt{\frac{\int_{-6}^{6}|R_0(\mu)-R(\mu)|^2 d\mu}{\int_{-6}^{6}|R_0(\mu)|^2 d\mu}}\,\%$$

is the relative mean-square error; $\delta[R] = \max|R_0(\mu) -$

Table 1. Characteristics of the function $W(\mu; b)$ as a directivity pattern for different values of the parameter b

b	CDA	*W1*	*W2*	*W3*, dB	*W4*, dB
1	0.730	0.454	1.000	−11.26	−∞
1/3	0.770	0.614	1.732	−20.21	−∞
1/9	0.673	0.712	2.000	−32.58	−∞
0	0.618	0.778	2.000	−23.29	−∞

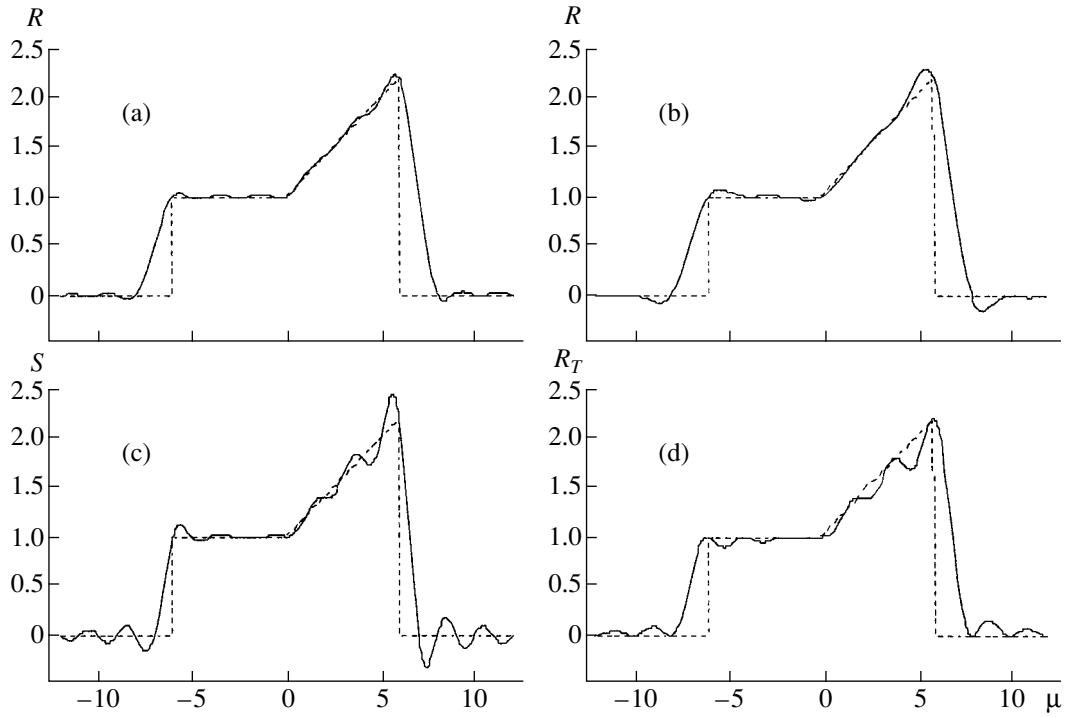

Fig. 3. Directivity pattern of the linear radiating system for the desired directivity pattern given by (18) (dashed line). The plots correspond to (15) with (a) $b = 1/9$ and (b) $b = 0$, (12) (c), and (19) (d).

$R(\mu)|$ with $|\mu| \le 6$ being the uniform error; and $A2[R] = 100\varepsilon[R]/\varepsilon[S]\%$ and $A3[R] = 100\delta[R]/\delta[S]\%$ are the ratios of the mean-square and uniform errors, respectively, for this approximation and those given by series (12).

We also synthesized the directivity pattern by means of series (16) with $b = 1/9$ for the desired directivity pattern of the form

$$R_0(\eta, \mu) = \begin{cases} 0, & |\mu|, |\eta| < 6 \\ 1, & -6 \le \eta < 0 \\ 1 - \eta/3, & 0 \le \eta \le 6. \end{cases} \quad (20)$$

The approximation of directivity pattern (20) by formula (16) is shown in Fig 4a. Directivity pattern (20)

Table 2. Characteristics of conventional directivity patterns and those based on atomic functions

Field distribution over the antenna mouth, $F(x)$	Directivity pattern, $R(\mu)$	CDA	*W1*	*W2*	*W3*, dB	*W4*, dB
$2\mathrm{up}\left(\frac{x}{\pi}\right)$	$\mathrm{Up}(\pi\mu)$	0.673	0.778	2.000	−23.29	−∞
$2\mathrm{up}\left(\frac{x}{\pi}\right) + \frac{2}{9}\mathrm{up}''\left(\frac{x}{\pi}\right)$	$\left(1 - \left(\frac{\mu}{3}\right)^2\right)\mathrm{Up}(\pi\mu)$	0.618	0.712	2.000	−32.58	−∞
$1, \lvert x\rvert \le \pi$	$\frac{\sin(\pi\mu)}{\pi\mu}$	1.000	0.443	1.000	−13.26	−3
$2\left(1 - \frac{\lvert x\rvert}{\pi}\right), \lvert x\rvert \le \pi$	$\frac{\sin^2(\pi\mu/2)}{(\pi\mu/2)^2}$	0.750	0.638	2.000	−26.52	−6
$2\cos^2\frac{x}{2}, \lvert x\rvert \le \pi$	$\frac{\sin(\pi\mu)}{\pi\mu(1 - (\mu/2)^2)}$	0.666	0.720	2.000	−31.46	−9

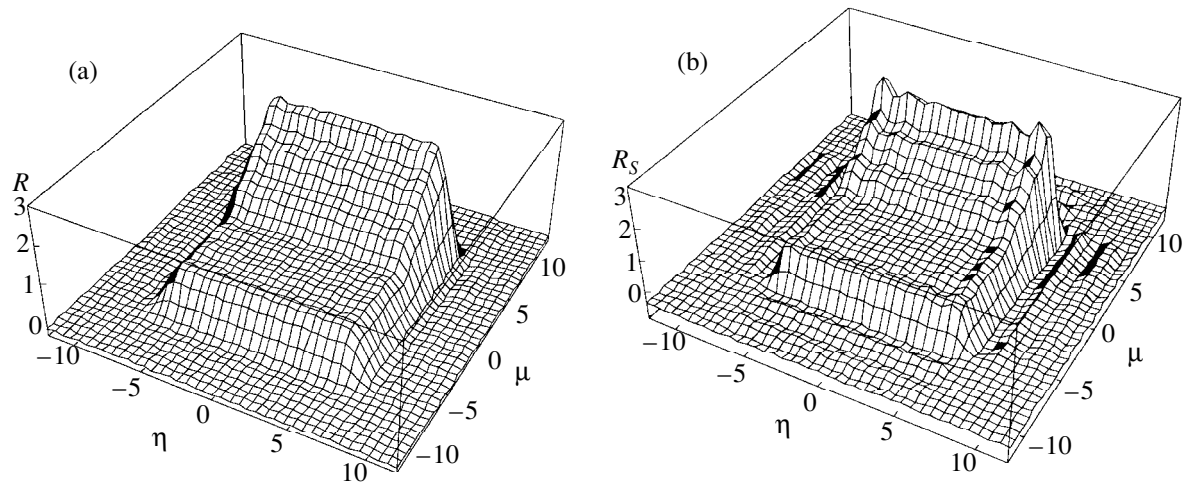

Fig. 4. Directivity pattern of the rectangular radiating system with the desired directivity pattern given by (20). The plots correspond to (a) (16) with $b = 1/9$ and (b) (21).

was also interpolated, for comparison, by the function

$$R_s(\mu, \eta) = \sum_m \sum_n R_0(m, n) \times \frac{\sin(\pi(\eta - n))}{\pi(\eta - n)} \frac{\sin(\pi(\mu - m))}{\pi(\mu - m)} \quad (21)$$

(see Fig. 4b). Hence, it follows that series (16) based on the atomic functions allows more precise approximation of the directivity pattern than conventional series (21).

Thus, for the first time, we have proposed and substantiated a new method of synthesizing directivity patterns for plane antenna mouths, which is based on the theory of atomic functions. The method proposed for plane mouths allows us to construct the directivity patterns that approximate a desired directivity pattern more precisely compared to the known methods for the cases of both mean-square and uniform errors. This method is supposed to be employed in solving problems of radars with lateral surveillance, because their resolutions need improvement by choosing the optimum field distribution over the antenna mouth.

The results of this paper were reported in part at the 2nd International Conference in Dubna, Russia [12].

Table 3. Approximation errors for desired directivity pattern (18) in the cases of conventional methods (12) and (19) and a method based on atomic functions (15)

Directivity pattern	*A1*, %	*A2*, %	δ	*A3*, %
$R(\mu; b = 1/9)$	1.919	31	0.082	25
$R(\mu; b = 0)$	3.975	64	0.188	59
$S(\mu)$	6.202	100	0.319	100
$R_T(\mu)$	6.464	104	0.283	88

ACKNOWLEDGMENTS

The authors are grateful to Corresponding Member of the RAS L.D. Bakhrakh, Academician of the NAS of Ukraine V.L. Rvachev, and Professor Ya.S. Shifrin for valuable discussions of the results obtained.

REFERENCES

1. E. G. Zelkin and V. G. Sokolov, *A Method of Antenna Synthesis* (Sov. Radio, Moscow, 1980).
2. B. M. Minkovich and V. P. Yakovlev, *Theory of Antenna Synthesis* (Sov. Radio, Moscow, 1969).
3. *Problems of Antenna Engineering*, Ed. by L. D. Bakhrakh (Radio i Svyaz', Moscow, 1989).
4. V. F. Kravchenko and V. V. Timoshenko, Élektromagn. Volny Élektron. Sist. **4** (5), 21 (1999).
5. V. F. Kravchenko and A. A. Zamyatin, Dokl. Akad. Nauk **365**, 340 (1999) [Dokl. Phys. **44**, 171 (1999)].
6. V. F. Kravchenko and A. A. Zamyatin, Dokl. Akad. Nauk **365**, 475 (1999) [Dokl. Phys. **44**, 216 (1999)].
7. V. F. Kravchenko, V. I. Pustovoĭt, and V. V. Timoshenko, Dokl. Akad. Nauk **368**, 184 (1999) [Dokl. Phys. **44**, 610 (1999)].
8. V. F. Kravchenko, in *Proceedings of the III International Conference on Antenna Theory and Techniques, Sevastopol, 1999*, p. 55.
9. V. F. Kravchenko, E. G. Zelkin, and V. V. Timoshenko, in *Proceedings of the III International Conference on Antenna Theory and Techniques, Sevastopol, 1999*, p. 124.
10. V. F. Kravchenko, V. L. Rvachev, and V. A. Rvachev, J. Commun. Technol. Electron. **40** (12), 118 (1995).
11. E. G. Zelkin, V. F. Kravchenko, V. I. Pustovoĭt, and V. V. Timoshenko, Dokl. Akad. Nauk **371**, 42 (2000) [Dokl. Phys. **45**, 97 (2000)].
12. V. F. Kravchenko. *Proceedings of the Second Int. Conf. on Modern Trends in Computational Physics. July 24–29, 2000. Dubna, Russia*, p. 106.

Translated by V. Chechin

Doklady Physics, Vol. 45, No. 9, 2000, pp. 454–456. Translated from Doklady Akademii Nauk, Vol. 374, No. 2, 2000, pp. 187–189.

TECHNICAL PHYSICS

Mechanism of Electron Detonation in Solid Dielectrics at High Discharge Speeds

Corresponding Member of the RAS Yu. N. Vershinin and D. S. Il'ichev

Received April 14, 2000

In [1], we proposed a model for the process of electron detonation (ED) where it was assumed that the source of the specific energy Q maintaining the detonation wave is related to the Joule loss in the energy release zone. From quantitative analysis of the electric parameters of this process, it follows that the model does not contradict the experimental data at the velocities of electron detonation and discharge meeting conditions $v_{ED} < 10$ km/s and $v_d < 150$ km/s, respectively. However, at higher values of v_d, which in KCl can be as high as 1100 km/s [2] at $U = 315$ kV and $v_{ED} \simeq 26$ km/s, the model under consideration should be modified.

This stems from the fact that the quadratic dependence of the enthalpy change Δh on the velocity v_{ED} results in a corresponding increase in temperature of the substance and, as a consequence, in its electric conductivity. Under these conditions, the Joule loss cannot provide the release of the required specific energy Q. In addition, it is worth noting that a steep increase in the velocity v_d (Fig. 2 in [1]) occurs in alkali-halide crystals at the pulse voltage $100 < U < 150$ kV. The latter fact can be related to a change in the mechanism of the energy release in the ED wave.

We estimate the composition of the material in the ED wave at velocities $v_{ED} > 15$ km/s using the method applied earlier in [1] in combination with the plasma chemical model and the main concepts of dense nonideal plasma [3].

In the velocity range of interest $v_{ED} > 15.0$ km/s, the polytropic index $n \simeq 1.9$ remains nearly constant. Hence, using the detonation approximation [4], we can evaluate pressure p and specific energy Q in the energy release zone of the ED wave:

$$p = \frac{\rho_0 v_{ED}^2}{n+1}, \quad Q = \frac{v_{ED}^2}{2(n^2-1)}. \tag{1}$$

Institute of Electrophysics, Ural Division, Russian Academy of Sciences, ul. Komsomol'skaya 34, Yekaterinburg, 620049 Russia

We extend to the ED process the method of thermal cycles, which is commonly used in the case of detonating explosives to calculate the heat Q released in the course of an explosion-like transformation [5]. Suppose that, under standard conditions, the energy consumption ΔH^0 for the transformation of the dielectric substance in the detonation wave to another phase state is compensated by the electric energy Q_e, i.e., $Q_e = \Delta H^0$. For the velocity range in KCl $14.5 < v_{ED} < 22.0$ km/s, it is easy to find that the values of Q determined by (1) lie within the range $38.8 \times 10^6 \le Q \le 94.1 \times 10^6$ J/kg, and the plasma composition corresponds to the degree of ionization $1 \le x_e \le 2$, i.e.,

$$\mathrm{KCl_{solid}} \xrightarrow{Q_1} \mathrm{K^+ + Cl^+ + 2e},$$

(P1) ($x_e = 1.0$; $Q_e = 38.8 \times 10^6$ J/kg);

$$\mathrm{KCl_{solid}} \xrightarrow{Q_2} \mathrm{K^+ + Cl^{2+} + 3e},$$

(P2) ($x_e = 1.5$; $Q_e = 52.7 \times 10^6$ J/kg);

$$\mathrm{KCl_{solid}} \xrightarrow{Q_3} \mathrm{K^{2+} + Cl^{2+} + 4e},$$

(P3) ($x_e = 2.0$; $Q_e = 94.1 \times 10^6$ J/kg).

Simultaneously solving the approximation equations of state for the dense nonideal plasma [3, 6]

$$\frac{U}{Nk} = -0.8\Gamma, \qquad \frac{U}{NkT} = a\Gamma + b\Gamma^{3/2} + c\Gamma^2, \tag{2}$$

we determine the plasma temperature and then the parameters of nonideality

$$\Gamma = \frac{z_1 z_2 e^2}{kTa}, \tag{3}$$

for ion

$$\theta = \frac{kT}{E_F} \tag{4}$$

and electron plasma components, respectively. In (2)–(4), z are the charges of the interacting particles, a =

1028-3358/00/4509-0454$20.00

Table 1

Plasma	U_0, kV	v_{ED}, 10^3 m/s	T, 10^3 K	Γ (3)	θ (4)	σ, 10^5 Ω^{-1} cm^{-1}	p, 10^{10} Pa	
							(1)	(5)
P1	175	14.5	6.33	15.6	0.11	5.13	13.5	15.6
P2	220	16.6	20.3	11.0	0.27	11.0	18.3	10.8
P3	315	22.0	36.2	10.9	0.40	20.7	32.5	50.0

$(0.75\pi n_e)^{1/3}$ is the mean interparticle distance; $E_F = \hbar^2(3\pi^2 n_e)^{2/3}(2m_e)^{-1}$ is the Fermi energy; and a, b, and c are the empirical coefficients [6] depending on θ. The calculated parameters of this plasma are presented in Table 1.

According to the classification given in [3, 7], the electron subsystem of such a plasma is degenerate and the ion subsystem can be considered to be classical. Both systems are characterized by strong interactions. Then, using the relationship for the pressure of the degenerate Fermi gas

$$p = \frac{(3\pi^2)^{2/3}\hbar^2}{5m_e} n_e^{5/2}, \quad (5)$$

we determine the electrical conductivity of plasma using the well-known Spitzer–Harm formula for the Coulomb logarithm at $\Gamma > 1$ [3]:

$$\ln\Lambda = \frac{1}{2}\ln\left[1 + \left(\frac{3\sqrt{2}}{\Gamma}\right)^2\right]. \quad (6)$$

As was mentioned in [3], fully ionized nonideal dense plasma can be considered as a disordered ionic lattice with ions localized in a spatial structure similar to the cubic or face-centered lattice. This structure arises owing to strong interparticle interactions. The equation describing the state of such a plasma can be written as [3]

$$U = U_0(n) + U_T(n, T). \quad (7)$$

It involves two components. The first, potential energy $U_0(n)$, depends only on ion density n and has a negative sign also corresponding to negative pressure in the ion subsystem. The total pressure is positive due to high pressure caused by the electron subsystem. The positive energy $U_T(n, T)$, also depending on the temperature, characterizes the thermal excitation of the ion subsystem in the plasma.

At discharge velocities $v_d \simeq 10^6$ m/s and length of the energy release zone $\Delta \simeq 10^{-5}$ m, such plasma exists during $\tau \simeq 10^{-11}$ s that is compatible with the eigenfrequency of ion oscillations $1/\omega = 10^{-11}$–10^{-12} s.

Therefore, one can argue that dense nonideal plasma under these conditions is in the state of a physical cluster [8] being stable within the medium where it was formed. The medium itself is characterized by the specified parameters (n, p, T). The disappearance of this medium or variation of its parameters leads to the spontaneous decay of the cluster, which is accompanied by to release of stored energy $U_0(n)$.

In the process of the electron detonation, the cluster decay can be caused by such a factor as high pressure of the electron gas initiating the fracture of solid dielectric in the vicinity of the discharge channel. In this case, the flow conditions in the electron detonation wave are changed compared to the similar process at small velocities v_d (see figure).

Correspondingly, this manifests itself in the equation for energy [1], which for the first section of the energy release zone takes the form (if we neglect the Joule loss)

$$h_1 = \frac{1}{2}v_{ED}^{-2}(1 - \delta^{-2}) + \frac{l_0 E_0 j}{\rho_0 v_{ED}} + U_T. \quad (8)$$

Here, U_T is the thermal energy of the physical cluster (6) in J/kg, l_0 is the length of the region in a solid dielectric with field E_0. Then, the total specific energy Q_1 responsible for maintaining the detonation wave is equal to

$$Q_1 = \frac{l_0 E_0 j}{\rho_0 v_{ED}} + U_T. \quad (9)$$

It is assumed here that the energy Q_2 released due to the decay of physical cluster produces secondary effects and causes mechanical failure of the dielectric. The observed features of this failure lend indirect support to such an assumption. Thus, the solid substance of the dielectric in the vicinity of the discharge channel having a radius r_0 [9] at the distance $r \le 10r_0$ is in the

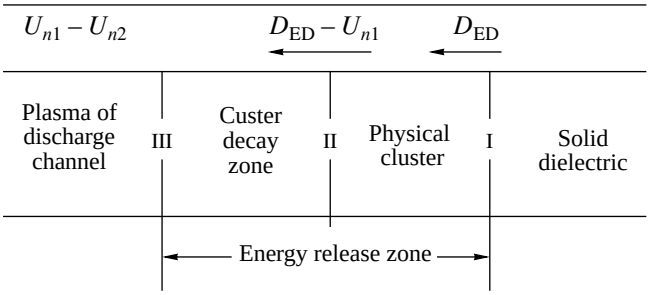

Figure.

Table 2

U, kV	v_d, 10^3 m/s	v_{ED}, 10^3 m/s	E_0, 10^3 V/s	$r_0 = l_0$, 10^{-6} m	l_n, 10^{-6} m	σ, Ω^{-1} m^{-1} [3]	Q, 10^6 J/kg (9)	U_T, J/kg [3]	j_0, 10^{10} A/m^2	i, A	
										calculations	experiment
50	6.0	5.5	2.86	0.5	5.0	2.5	1.0	–	0.23	1.8×10^{-3}	$\sim 10^{-3}$
220	890	20.0	1.90	9.0	–	1.1×10^6	75.0	4.6	33	42.0	60.0

fine-dispersed state. The value of r depends only on the velocity v_d and is independent of energy W stored in the pulse generator. At $v_d < 10^5$ m/s, this range becomes optically unresolvable, i.e., $r \longrightarrow 0$. Outside this near-field fracture zone, the crack propagation is observed. In contrast to r, the crack length does not depend on v_d and increases with the growth of energy W and the duration of the steady current.

In Table 2, the calculated values of the parameters for the ED process in KCl are given as an example of the use of the relationships discussed above at two values of discharge velocities: 5.5 and 890 km/s. The former velocity $v_d = 5.5$ km/s is the minimum velocity for the given dielectric. The formation of the quantity Q is related in this case to the Joule loss [1].

At $v_d = 890$ km/s, the parameters of the process were found according to (8) and (9), and the relation between v_d and v_{ED} was determined similarly to [1].

In the one-dimensional model (see figure), the length of the layer l_0 with field E_0 is infinite. This is inconsistent with the actual distribution of the field in the initial part of the discharge channel. In this connection, we assume that the phase surface is a sphere of radius r_0. Taking into account the fact that the electric field near such a surface varies as $E \sim r^{-2}$, we assume for further estimations that $l_0 \simeq r_0$.

The field E_0 was calculated similarly to [1] but with the help of a formula from [10] for the probability of creating the electron–hole pairs, taking into account the dependence of baric coefficient a_p on the compressibility K at $p > 10^{10}$ Pa and the degree of ionization $x_e = 5 \times 10^{-2}$.

It must be emphasized that the data presented in Table 2 should be considered to be estimates accurate within an order of magnitude. This is due to not only the use of the one-dimensional model of the process and the assumptions employed. The calculations of parameters were performed based on the assumption that the detonation obeys the Chapman–Jouguet conditions [4]. However, this is not evident. It is quite possible that the energy Q_2 released during the decay of the physical cluster can promote secondary compression waves. These waves will play the role of the piston affecting the products of electron detonation. In this case, the process of the detonation may be "overcompressed" [4].

Undoubtedly, the further improvement of the approach proposed for describing the mechanisms of electric discharge propagation in solid dielectrics requires undertaking a large body of specially formulated theoretical and experimental studies. Nevertheless, this method seems to be promising, since it for the first time provides an opportunity to reveal the interrelation between parameters of the voltage pulse (U, $\frac{dU}{dt}$, i), space-time characteristics of the electric discharge (v_p, r_0), individual properties of dielectrics (ε, ρ_0, δ, K, E_g), and thermal and other properties of the material in the discharge channel (p, T, U, h, x_e, σ).

REFERENCES

1. Yu. N. Vershinin and D. S. Il'ichev, Dokl. Akad. Nauk **365**, 617 (1999) [Dokl. Phys. **44**, 220 (1999)].
2. Y. N. Vehshinin, G. A. Mesyats, A. L. Mironov, and A. A. Podrezov, in *Proceedings of the IEEE International Puls. Power Conference* (San Diego, 1991), p. 353.
3. V. E. Fortov and I. T. Yakubov, *Physics of Nonideal Plasma* (Chernogolovka, 1984).
4. Ya. B. Zel'dovich and A. S. Kompaneets, *Theory of Detonation* (GITTL, Moscow, 1953).
5. F. A. Baum, K. P. Stanyukovich, and B. I. Shekhter, *Physics of Explosion* (Nauka, Moscow, 1959).
6. S. Tanaka, S. Mitake, X.-Z. Yan, and S. Ichumaru, Phys. Rev. A **32**, 1779 (1985).
7. N. I. Klyuchnikov and S. A. Triger, Zh. Éksp. Teor. Fiz. **52**, 276 (1967) [Sov. Phys. JETP **25**, 178 (1967)].
8. P. P. Kulik, G. É. Norman, and L. S. Polak, Khim. Vys. Énerg. **10**, 203 (1976).
9. Yu. N. Vershinin, Dokl. Akad. Nauk **347**, 614 (1996) [Phys. Dokl. **41**, 157 (1996)].
10. P. Feuer, Phys. Rev. **88**, 92 (1952).

Translated by Yu. Vishnyakov

Doklady Physics, Vol. 45, No. 9, 2000, pp. 457–462. Translated from Doklady Akademii Nauk, Vol. 374, No. 3, 2000, pp. 324–329.

TECHNICAL PHYSICS

Atomic Functions and Direct Methods for Solving the Fredholm Integral Equation of the First Kind in the Problem on Synthesis of Linear Antennas

M. A. Basarab*, V. F. Kravchenko,**
and Corresponding Member of the RAS V. I. Pustovoĭt***

Received March 23, 2000

INTRODUCTION

The antenna synthesis is known to be a problem in determining the field $y(t)$ in the antenna aperture D based on the given directivity diagram. This problem is reduced to finding a solution to the one-dimensional Fredholm integral equation of the first kind in the case of a rectilinear aperture

$$\int_{-a}^{a} y(t)e^{itx}dt = f(x), \qquad (1)$$

where $x = k\sin\theta$, $k = 2\pi/\lambda$ is the wave number, $f(x)$ is the directivity diagram, and $2a$ is the aperture length.

A large number of the existing synthesis methods [1–3] emphasize an unabated interest in the problem and partially stem from the difficulties in solving integral equation (1), which forms the basis of the synthesis theory. However, it is possible to set off two principal approaches. The first one, the most simple and obvious, consists in applying numerical methods with the preliminary regularization of an ill-posed problem (statistical approach by definition of Tikhonov and Lavrent'ev). Second, there exist widely used methods of implicit regularization, among which we should note first of all the partial-diagram method [3]. In this case, an expression for the field is sought in the form of a series in terms of a specially chosen system of functions. The most frequently used functions are $\mathrm{sinc}(x)$ (the Kotel'nikov series), the Bessel functions of integer or half-integer subscript, and also the eigenfunctions of the operator of problem (1), that is, the Mathieu and Lamé functions. Each system has its advantages and disadvantages and, thus, its domain of application. At the same time, the universal methods based on the approximation of an unknown solution and the right-hand side of problem (1) by finite functions become more and more popular. For example, the double-spline-approximation method for solving the Fredholm integral equations of the first kind is proposed in [4]. Recently, potentialities of the mathematical formalism of atomic functions were widely studied with respect to the problem of antenna synthesis [5–9].

In this paper, we use the approximation properties of a set of atomic functions $\mathrm{fup}_n(x)$ and study the problem associated with the implicit regularization arising in this case.

Formulation of the problem and a method of solution. We solve the Fredholm integral equation of the first kind

$$\int_{a}^{b} K(x, t)y(t)dt = f(x), \quad c \le x \le d. \qquad (2)$$

According to the partial-diagram method [3], we present an unknown solution and also the right-hand side of the equation in the form of a series corresponding to the complete system of functions $\{\varphi\}$ and $\{\psi\}$:

$$\tilde{y}(x) = \sum_{k=0}^{N} \tilde{u}_k\varphi_k(x), \qquad (3)$$

$$\tilde{f}(x) = \sum_{k=0}^{N} d_k\psi_k(x). \qquad (4)$$

Here, d_k are the known coefficients and $\tilde{u}_k$ are the coefficients to be determined. We introduce the notation

$$h^{(k)}(x) = \int_{a}^{b} K(x, t)\varphi_k(t)dt. \qquad (5)$$

* *Institute of Mechanical Engineering Problems, National Academy of Sciences of Ukraine, ul. Dm. Pozharskogo 2/10, Kharkov, 310046 Ukraine*
** *Institute of Radio Engineering and Electronics, Russian Academy of Sciences, ul. Mokhovaya 11, Moscow, 103907 Russia*
*** *Central Design Bureau of Unique Instrumentation, Russian Academy of Sciences, ul. Butlerova 15, Moscow, 117342 Russia*

1028-3358/00/4509-0457$20.00

The latter functions are expanded in terms of system $\{\psi\}$:

$$\tilde{h}^{(k)}(x) = \sum_{j=0}^{N} b_j^{(k)} \psi_j(x). \quad (6)$$

In this case, the algebraic system needed to determine unknown coefficients $\tilde{u}_k$ is

$$\sum_{k=0}^{N} \tilde{u}_k b_j^{(k)} = d_j, \quad j = 0, 1, \ldots, N,$$

or, in the matrix form,

$$B\tilde{U} = D. \quad (7)$$

We now analyze various methods allowing us to determine the elements of matrix B and vector D.

Collocation method. We determine the components of the column vectors of matrix B and vector D as

$$\Psi B^{\langle k \rangle} = H^{\langle k \rangle}, \quad \Psi D = F,$$

$$\Psi_{i,j} = \psi_j(x_i), \quad H_i^{\langle k \rangle} = h^{(k)}(x_i), \quad F_i = f(x_i),$$

$$x_i = c + i\frac{d-c}{N}, \quad i, j = 0, 1, \ldots, N.$$

It is easy to see that

$$\Psi B = H,$$

and, taking (7) into account, we obtain the following system for finding the unknown vector $\tilde{U}$:

$$H\tilde{U} = F, \quad (8)$$

where

$$H_{i,j} = \int_a^b K(x_i, t)\varphi_j(t)dt, \quad F_i = f(x_i), \quad i, j = 0, 1, \ldots, N. \quad (9)$$

Moments method. Introducing definitions

$$\Psi_{i,j} = (\psi_i, \psi_j), \quad F_i = (f, \psi_i), \quad H_i^{\langle k \rangle} = (h^{(k)}, \psi_i), \quad i, j = 0, 1, \ldots, N,$$

we obtain the system similar to (8) in which

$$H_{i,j} = \int_c^d \psi_i(x)dx \int_a^b K(x, t)\varphi_j(t)dt,$$
$$F_i = \int_c^d f(x)\psi_i(x)dx, \quad i, j = 0, 1, \ldots, N. \quad (10)$$

Method of least squares. In this case, the components of the matrix H and vector F are determined as

$$H_{i,j} = \int_c^d \left[\int_a^b K(x, s)\psi_i(s)ds \int_a^b K(x, t)\varphi_j(t)dt\right]dx,$$
$$F_i = \int_c^d f(x)dx \int_a^b K(x, t)\psi_i(t)dt, \quad i, j = 0, 1, \ldots, N. \quad (11)$$

We assume below that $\{\varphi\}$ and $\{\psi\}$ are the sets of functions with a bounded support set normalized in the form

$$\sum_{k=0}^{N} \varphi_k(x) \equiv 1, \quad \sum_{k=0}^{N} \psi_k(x) \equiv 1. \quad (12)$$

Let

$$\bar{y}(x) = \sum_{k=0}^{N} \bar{u}_k \varphi_k(x) \quad (13)$$

be an element of the closest approximation for an unknown solution $y(x)$. In this case, the following theorem holds.

Theorem. *For an error in approximate solution* (3), *whose coefficients are found from the solution to set* (8), *the following estimates are valid*:

(i) *for the collocation method* (9)

$$\|\tilde{y}(x) - y(x)\| \le \|\bar{y}(x) - y(x)\| \times (1 + (b-a)\|H^{-1}\|_\infty \cdot \|K(x, t)\|); \quad (14)$$

(ii) *for the moments method* (10)

$$\|\tilde{y}(x) - y(x)\| \le \|\bar{y}(x) - y(x)\| \times (1 + (b-a)(c-d)\|H^{-1}\|_\infty \cdot \|K(x, t)\| \cdot \|\psi(x)\|); \quad (15)$$

(iii) *for the method of least squares* (11)

$$\|\tilde{y}(x) - y(x)\| \le \|\bar{y}(x) - y(x)\| \times (1 + (b-a)^2(c-d)\|H^{-1}\|_\infty \cdot \|K(x, t)\|^2 \cdot \|\psi(x)\|). \quad (16)$$

Proof. We prove inequality (14). The validity of expressions (15) and (16) can be verified similarly. Using the triangle inequality, we have

$$\|\tilde{y}(x) - y(x)\| \le \|\tilde{y}(x) - \bar{y}(x)\| + \|\bar{y}(x) - y(x)\|. \quad (17)$$

From (3), (13), and (12), it follows that

$$\|\tilde{y}(x) - \bar{y}(x)\| = \left\|\sum_{k=0}^{N} (\tilde{u}_k - \bar{u}_k)\varphi_k(x)\right\| \le \max_k |\tilde{u}_k - \bar{u}_k| \left\|\sum_{k=0}^{N} \varphi_k(x)\right\| \le \|\tilde{U} - \bar{U}\|_\infty. \quad (18)$$

It is evident that

$$H\bar{U} = F - \Delta, \quad \Delta_i = \int_a^b K(x_i, t)(y(t) - \bar{y}(t))dt,$$
$$i = 0, 1, \ldots, N.$$

Thus,

$$\tilde{U} - \bar{U} = H^{-1}\Delta$$

and

$$\|\tilde{U} - \bar{U}\|_\infty \le \|H^{-1}\|_\infty \cdot \|\Delta\|_\infty$$
$$\le \|H^{-1}\|_\infty \cdot (b-a)\|K(x,t)\| \cdot \|\bar{y}(x) - y(x)\|.$$

Substituting the last estimate into (18) and, then, (18) into (17), we obtain inequality (14), which proves the theorem.

From (14)–(16), it is clear that the accuracy of the approximate solution depends on the norm of the inverse matrix H^{-1}, and it is not a simple task to find its analytical estimate. When N increases, the value of $\|\tilde{y}(x) - y(x)\|$ tends to zero, whereas $\|H^{-1}\|_\infty$ tends to infinity. The problem is to find such a partition parameter N (for simplicity, we assume its uniformity), for which a stable approximate solution corresponding to the least error can be found.

As we already mentioned, one of the most promising lines of research in the theory of approximations (including the solution of ill-posed problems) is the use of the mathematical formalism of atomic functions [10].

Atomic functions up(x) and fup$_n$(x). The function up(x) is the simplest atomic function satisfying the following functional differential equation:

$$\mathrm{up}'(x) = 2\mathrm{up}(2x+1) - 2\mathrm{up}(2x-1),$$
$$\mathrm{supp\,up}(x) = [-1; 1], \quad \mathrm{up}(x) \in C^\infty(-\infty; \infty).$$

The function up(x) is even, up(0) = 1. The function increases at [–1; 0], decreases at [0; 1], and up(1 – x) = 1 – up(x). The following recurrent relations are obtained for the moments of up(x):

$$a_0 = 1, \quad a_{2n} = \frac{(2n)!}{2^{2n} - 1}\sum_{k=1}^{n}\frac{a_{2n} - 2k}{(2n-2k)!(2k+1)!},$$

$$b_{2n+1} = \frac{1}{(n+1)\times 2^{2n+3}}\sum_{k=0}^{n+1} a_{2n+2},$$

where

$$a_{2n} = \int_{-1}^{1} x^{2n}\mathrm{up}(x)dx, \quad b_n = \int_0^1 x^n \mathrm{up}(x)dx.$$

Values of the function up(x) at points $k/2^n$ are rational numbers, in particular,

$$\mathrm{up}(-1 + 2^{-n}) = \frac{b_{n-1}}{2^{n(n-1)/2}(n-1)!}.$$

For finding up(x) at an arbitrary point, it is possible to use the rapidly converging series of the form

$$\mathrm{up}(x-1) = \sum_{k=1}^{\infty}(-1)^{s_k+1}p_k$$
$$\times \sum_{j=0}^{k}\frac{2^{((j+1)j-(k-j)(k-j-1))/2}b_{k-j-1}}{(k-j-1)!\,j!}(x-0, p_1\ldots p_k)^j,$$
$$0 \le x < 1,$$

where

$$b_{-1} = 1, \quad 0! = 1, \quad s_k = \sum_{j=1}^{k} p_j,$$

while $x = 0$, $p_1\ldots p_k$ is the representation of x in the binary number system.

The recurrent functional differential relationships determining atomic function fup$_n$(x) are similar to the equations for the Schoenberg B_n-splines

$$y_n'(x) = K\left\{y_{n-1}\left(x - \frac{1}{2}\right) - y_{n-1}\left(x + \frac{1}{2}\right)\right\},$$
$$y_0(x) = \mathrm{up}(x),$$

where K is the normalization factor. From these equations, it follows that

$$\mathrm{supp\,fup}_n(x) = \left[-\frac{n+2}{2}, \frac{n+2}{2}\right].$$

Within this interval, function fup$_n$(x) can be expressed as

$$\mathrm{fup}_n(x) = \sum_{i=0}^{m+1}\alpha_i^{(m)}\mathrm{up}\left[2^{-m}\left(x - 2^m + \frac{m}{2} + 1 - i\right)\right],$$

$$\alpha_0^{(m)} = 1, \quad \alpha_i^{(m)} = (-1)^i C_{m+1}^i - \sum_{j=0}^{i-1}\alpha_j^{(m)}\delta_{i-j+1},$$
$$\delta_1 = 1, \quad \delta_{2k} = -\delta_k, \quad \delta_{2k-1} = \delta_k.$$

We consider the approximation for the function $f(t) \in C^r[-\pi; \pi]$ specified at a uniform net Δ_N: $t_i = ih$, $h = \pi/N$, $i = \overline{-N, N}$ by elements $\mathrm{UP}_{N,r}$ of the space of linear combinations of translations–contractions of the functions up(x):

$$\sum_k d_k \mathrm{up}\left(\frac{x+\pi}{2^r h} - k\times 2^{-r}\right).$$

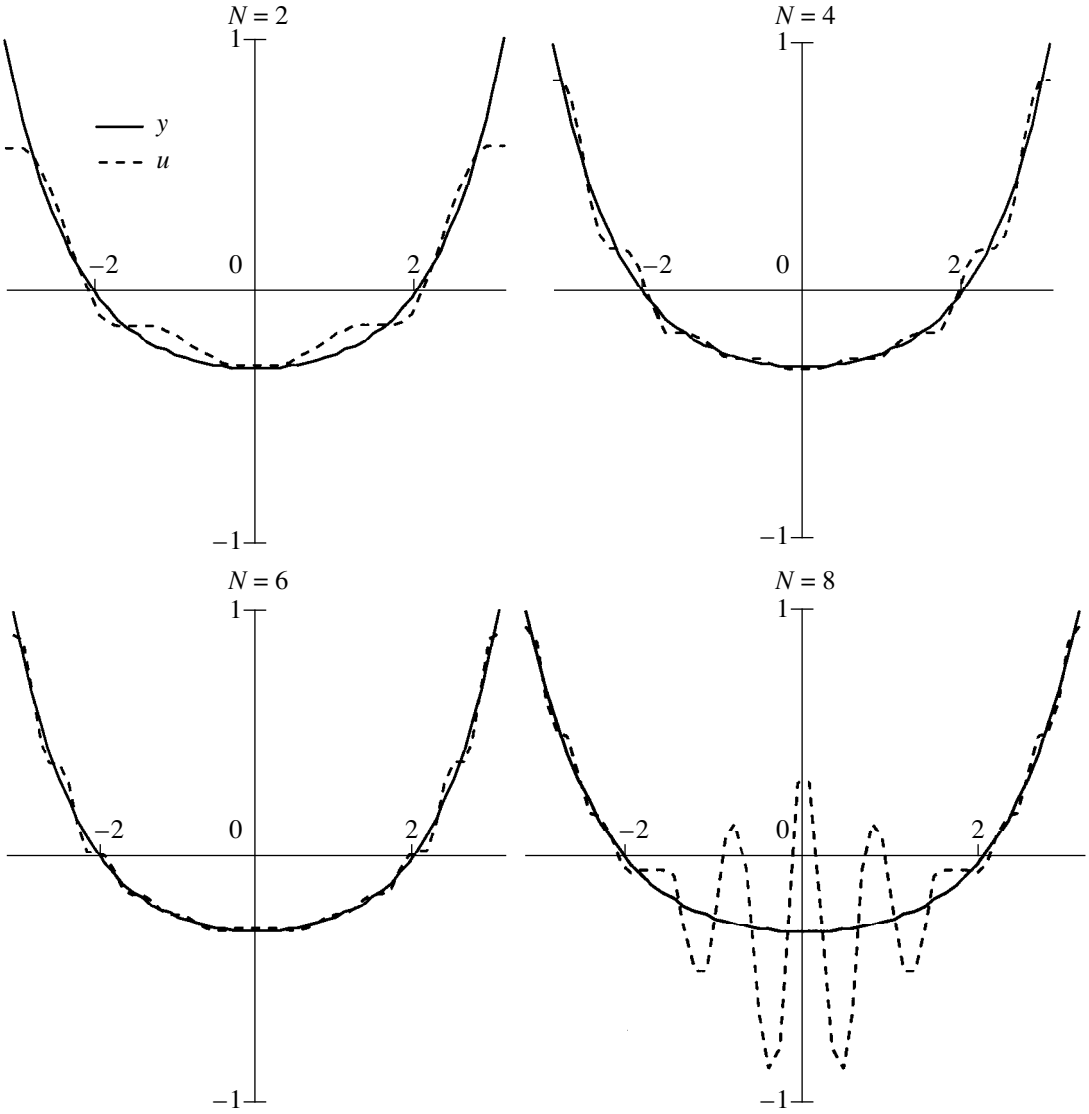

Fig. 1. Exact solution to problem (21) and its approximation using the basis of translations–contractions for the functions up(x).

We assume that r is even and the values of functions $f(t)$ are known at the points

$$\tau_k = kh, \quad k = \overline{-N - \frac{r}{2}, N + \frac{r}{2}}.$$

The space $\mathrm{UP}_{N,r}$ has the basis consisting of the translations–contractions of the finite function $\mathrm{fup}_r(x)$. The atomic approximation of the rth order for function $f(t)$ is given by the relationship

$$\Phi_{N,r}(f; t) = \sum_{k=-N-r/2}^{N+r/2} c_k \varphi_{r,k}(t), \qquad \Phi_{N,r}(f; \tau_k) = f(\tau_k), \tag{19}$$

where $\varphi_{r,k}(t) \equiv \mathrm{fup}_r\left(\frac{t+\pi}{h} - k\right)$ and support $\varphi_{r,k}(t)$ is determined by the inequality $|t - \tau_k| \le \frac{r+2}{2} h$. It is well known [10] that $\forall h > 0\ \exists c_k$ are such that

$$\| f(x) - \Phi_{N,r}(f; x) \|_{C^l[-\pi;\,\pi]} \le K_r h^{r-1} \omega_r(f; h), \tag{20}$$

where $\omega_r(f; h)$ is the continuity modulus of function $f^{(r)}(x)$ and K_r is independent of h (but depends on r).

Numerical simulations. According to [2], we have

$$\int_{-\pi}^{\pi} K(x, t) y(t) dt = f(x), \quad -\pi \le x \le \pi,$$
$$K(x, t) = e^{ixt}, \quad f(x) = 2\pi \frac{\sin(\pi\sqrt{1 + x^2})}{\pi\sqrt{1 + x^2}}. \tag{21}$$

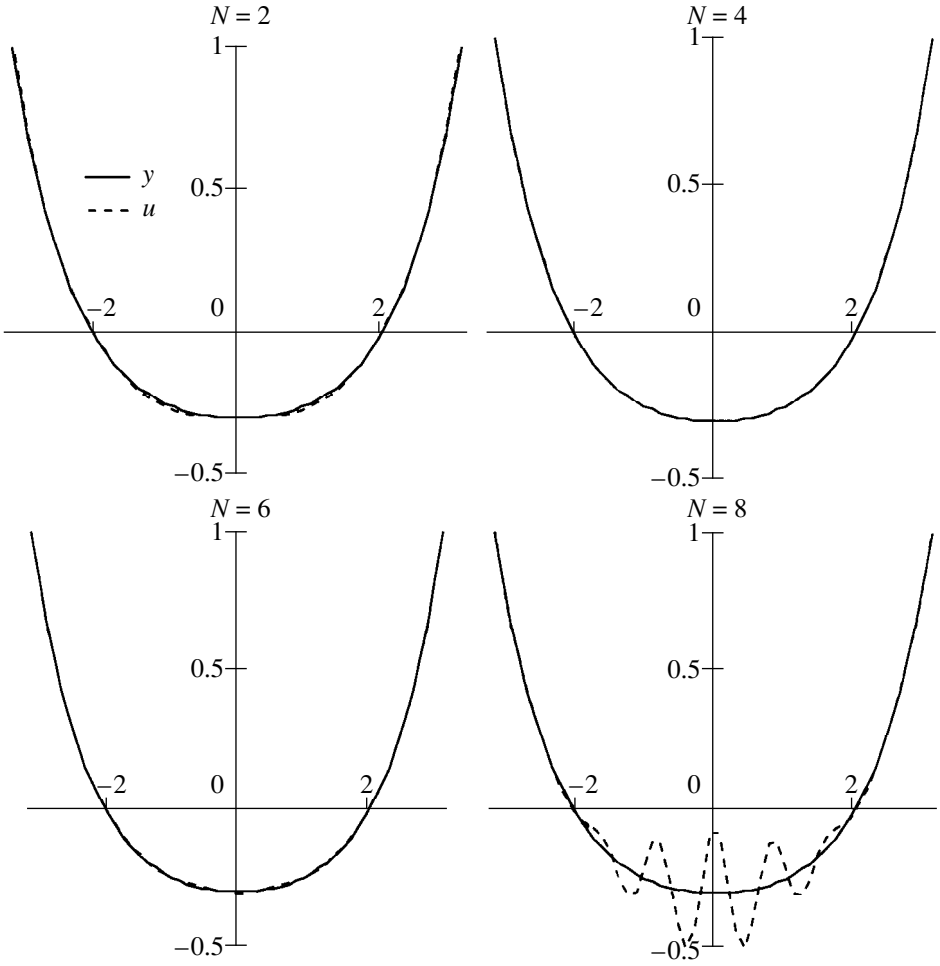

Fig. 2. Exact solution to problem (21) and its approximation using the basis of translations–contractions for the functions $\mathrm{fup}_2(x)$.

It is evident that, owing to the evenness of the desired solution, its kernel looks like $\cos(x, t)$. The approximate solution $u(x)$ was found by the collocation method (8), (9) with the help of the basis of atomic functions (19) and was compared with the known exact solution

$$y(t) = J_0\sqrt{\pi^2 - t^2}, \tag{22}$$

where J_0 are the Bessel zero-order function of the first kind. In Tables 1 and 2 and in Figs. 1 and 2, we presented the results of calculations for the system of the atomic functions $\mathrm{up}(x)$ and $\mathrm{fup}_2(x)$ corresponding to the values $r = 0$ and $r = 2$. In the figures, the solid lines correspond to exact solution (22) and the dashed lines correspond to the successive approximations to the exact solution. Note that the relative error gradually decreases (Figs. 1 and 2) with the increase in N up to a certain moment [$N = 7$ for $\mathrm{up}(x)$ and $N = 5$ for $\mathrm{fup}_2(x)$]. Upon a further increase in the N values, the stability of approximate solution (19) is violated. This fact is illustrated by the shape of curves in Figs. 1 and 2. From the analysis of the results listed in Tables 1 and 2, it follows that both optimum parameters N of the uniform-net partition can be found by means of the successive comparison of the differences between the approximate solutions. The minimum of this difference corresponds to the optimum values of N. The minimum error level

Table 1. Behavior of the norm of the inverse matrix and of relative errors in the approximate solution as functions of the partition parameter N [the case of $\mathrm{up}(x)$]

N	$\|H^{-1}\|_\infty$	$\dfrac{\|y-u\|_C}{\|y\|_C}$	$\dfrac{\|y-u\|_{L_2}}{\|y\|_{L_2}}$
1	19.75	8.84	18.6
2	1.58	0.43	0.29
3	1.2	0.2	0.17
4	5.54	0.15	0.13
5	343.9	0.11	0.11
6	3.2×10^4	0.09	0.10
7	5.3×10^6	0.08	0.11
8	6.7×10^7	0.61	0.65

Table 2. Behavior of the norm of the inverse matrix and relative errors in the approximate solution as functions of the partition parameter N [the case of $\mathrm{fup}_2(x)$]

N	$\|H^{-1}\|_\infty$	$\frac{\|y-u\|_C}{\|y\|_C}$	$\frac{\|y-u\|_{L_2}}{\|y\|_{L_2}}$
1	252.2	0.09	0.15
2	96.17	0.03	0.03
3	120.52	0.02	0.01
4	931.8	3×10^{-3}	2.7×10^{-3}
5	3.4×10^4	1.2×10^{-3}	1.4×10^{-3}
6	1.4×10^6	3.7×10^{-3}	5×10^{-3}
7	7.6×10^7	0.12	0.15
8	7.2×10^7	0.22	0.23

corresponds by an order of magnitude to the theoretical estimates of the expected error following from (20) and also to estimate (14) obtained in the theorem.

We may conclude that the method proposed in this paper has much in common with the partial-diagram method and represents, in fact, an implicit regularization of the ill-posed synthesis problem. This method is very flexible and convenient for its numerical implementation as compared to the methods of explicit regularization. The numerical simulations confirm the efficiency of the method. The proposed procedure can be extended to solving a wide class of ill-posed problems of a different physical nature.

ACKNOWLEDGMENTS

We are grateful to Academician of the National Academy of Sciences of Ukraine V.L. Rvachev, Professor E.G. Zelkin and Professor Ya.S. Shifrin for discussion of the results of this study.

REFERENCES

1. G. T. Markov and E. N. Vasil'ev, *Mathematical Methods of Applied Electrodynamics* (Sov. Radio, Moscow, 1970).
2. A. F. Verlan' and V. S. Sizikov, *Methods of Solution of Integral Equations with Computer Programs* (Naukova Dumka, Kiev, 1978).
3. E. G. Zelkin and V. G. Sokolov, *Methods of Antenna Synthesis* (Sov. Radio, Moscow, 1980).
4. A. I. Grebennikov, *Methods of Splines and Solution of Ill-Posed Problems in Approximation Theory* (Mosk. Gos. Univ., Moscow, 1983).
5. V. F. Kravchenko, Zarubezh. Radioélektron.: Usp. Sovrem. Radioélektron., No. 8, 23 (1996).
6. V. F. Kravchenko and V. A. Rvachev, in *Proceedings of PIERS'98, Nantes, 1998*, Vol. 3, p. 1186.
7. V. F. Kravchenko and A. A. Zamyatin, in *Proceedings of the III International Kharkov Symposium on Physics and Engineering of Millimeter and Submillimeter Waves, MSMW'98, Kharkov, 1998*, Vol. 1, p. 413.
8. V. F. Kravchenko and A. A. Zamyatin, Dokl. Akad. Nauk **365**, 475 (1999) [Dokl. Phys. **44**, 216 (1999)].
9. V. F. Kravchenko and V. V. Timoshenko, Élektromagn. Volny Élektron. Sist. **4** (5), 21 (1994).
10. V. L. Rvachev and V. A. Rvachev, *Non-Classical Methods of Approximation Theory in Boundary Problems* (Naukova Dumka, Kiev, 1979).

Translated by V. Bukhanov

Doklady Physics, Vol. 45, No. 9, 2000, pp. 463–466. Translated from Doklady Akademii Nauk, Vol. 374, No. 1, 2000, pp. 40–43.

ASTRONOMY, ASTROPHYSICS, COSMOLOGY

A Possible Mechanism of Solar Flare

Academician S. S. Grigoryan*, S. Ibadov, and F. S. Ibodov*****

Received May 23, 2000

Coronographic observations by SOLWIND, SMM (Solar Maximum Mission), and SOHO (Solar and Heliospheric Observatory) missions indicate the presence of a continuous comet flow passing close to the solar surface or colliding with the Sun [1–5].

According to the celestial-mechanics calculations [4], such a situation occurs rather frequently. Indeed, about 10% of long-period comets with initially high-inclination orbits ($i = 90° \pm 15°$) and moderately small perihelion distances ($q \le 2$ AU) pass the sungrazer stage (with $q < 0.01$ AU) for the time corresponding to 500–1000 revolutions around the Sun, i.e., at least ten times shorter than the time scale of their dynamic ejection. The available observational data related to bodies approaching the Sun [1–3, 5] indicate that during a decade several collisions of such bodies, i.e., comets, with the Sun, do occur. [In the vicinity of the Sun, at a specific irradiation power more than 10^{10} erg/(cm^2 s), not only proper cometary nuclei in the form of a conglomerate of ice and solid particles, but also iron-stony asteroidal bodies are involved in a regime of intense evaporation, and thus, become bodies with continuously rejuvenating atmospheres, i.e., comets]. This implies (see also [6]) that the frequency of comet-like bodies moving near the solar surface and falling onto the Sun (large meteoroids, proper comets and asteroids that, following the tradition [1–5], we call further cometary nuclei) is hundreds times more than the collision frequency for such bodies with planets.

At the same time, the disintegration process of nuclei for sungrazing comets (sungrazers) being considered in the framework of the traditional sublimation model, i.e., under the action of the solar thermal radiation, leads to an insignificant decrease of the nucleus radius, attaining no more than 20 m [1, 3]. Meanwhile, comets passing near the solar photosphere turn out in severe extremal conditions, which is associated with high velocities of their motion (about 600 km/s) and the presence of an extended solar atmosphere, including together with the photosphere the chromosphere and corona. The results of analysis of this situation [7] show that, within the solar chromosphere, an intense aerodynamic fragmentation of cometary nuclei occurs, and the regime of their sublimation acquires a qualitatively different, meteorite-like character. At the same time, both the problem of a possibility of arising solar flares due to developing explosive phenomena of the Tunguska-type event [8–11] and that of the mechanisms of developing of such processes in themselves remain basically open [10–13].

In the present paper, the analytical approach [8, 9] is being developed to investigate the explosive phase of the evolution of cometary nuclei under conditions of their intense interaction with the atmosphere. On this basis, we consider the possibility of the generation of solar flares by nuclei having a short perihelion.

The solar atmosphere, as is well known (see, e.g., [14]), is strongly nonisothermal and can be approximately presented as a stratified multitemperature structure described by the exponential distribution of the matter density near the solar surface

$$\rho_a = \rho_0 \exp\left(-\frac{z}{H}\right). \quad (1)$$

Here, H is the local altitude scale (H = 600 and 150 km for the chromosphere and photosphere, respectively); z is the altitude for which the limb of the Sun disk with the optical density τ_λ (λ = 5000 Å) = 0.005 is taken as the reference point; and $\rho_0 = \rho(z = 0) = 10^{-8}$ g/cm^3.

As our calculation shows, the decrease in the radius of cometary nuclei with sizes more than several hundreds meters turns out to be relatively small while passing near the Sun, due to the decrease of the heat-transfer coefficient. This fact is associated with both screening the nucleus by ejected molecules and the gas opacity in the shock layer ahead of the nucleus. Under these conditions, the mass of the cometary atmosphere is relatively small. The deceleration of the nucleus in the induced magnetosphere, while moving the comet in the vicinity of the Sun, is also small. Thus, the motion of the sufficiently large nucleus in the solar atmosphere

* *Institute of Mechanics, Moscow State University, Michurinskiĭ pr. 1, Moscow, 117192 Russia*
E-mail: grigor@inmech.msu.su

** *Institute of Astrophysics, Academy of Sciences of Republic Tajikistan, ul. Bukhoro 22, Dushanbe, 734042 Tajikistan*
E-mail: subhon@ac.tajik.net

*** *Sternberg Astronomical Institute, Moscow State University, Universitetskiĭ pr. 13, Moscow, 119899 Russia*
E-mail: mshtf@sai.msu.su

1028-3358/00/4509-0463$20.00

may be considered on the basis of the physical theory for meteorites within the constant-mass approximation [7].

In the case of approaching the cometary nucleus to the solar photosphere with the orbital velocity $V = V_0 =$ 600 km/s, the ram aerodynamic pressure $P_a = \rho_a V^2$ at the nucleus surface rises exponentially according to expression (1). Assuming the strength of the nucleus material $\sigma_* = 10^4$ dyn/cm^2 [15] and $H = 6 \times 10^7$ cm, we have, according to [7], for the altitude of the onset of the nucleus fragmentation and the corresponding atmosphere density $z_* = 8H = 5000$ km and $\rho_* = 3 \times 10^{-12}$ g/cm^3, respectively. For the nucleus in the form of an iron-stony body with $\sigma_* = 10^8$ dyn/cm^2, we find $z_* = -H = -200$ km and $\rho_* = 3 \times 10^{-8}$ g/cm^3.

The rapid rise of aerodynamic pressure at the entry of the nucleus into more dense atmosphere layers leads to the situation when the destruction being started locally propagates through the nucleus body from the frontal surface to the rear surface. At the same time, the fragmented mass loses its integrity, spreading in the lateral direction under the action of the pressure gradient at the frontal surface. The equation for the deceleration of the completely fragmented transversely expanding nucleus in the constant-mass approximation can be presented according to [9] in the form

$$\int_{\tilde{V}}^{V} \frac{dV}{V} = -\frac{\rho_0 H}{2R_0^3 \rho_n \sin\alpha} \frac{b}{\nu} \int_{\tilde{r}}^{r} R^2 dr. \quad (2)$$

Here, $R = R[r(z)]$ is the law for the variation of the transverse radius for the fragmented mass:

$$\frac{R}{2R_0} = 1 + \frac{1}{C}\sqrt{\frac{b}{2}}(\sqrt{1+r} - \sqrt{1+\tilde{r}}); \quad (3)$$

R_0 and ρ_n are the initial radius and the density of the nucleus, respectively; α is the angle between the velocity of the nucleus entry into the atmosphere and the horizon;

$$b = \nu \exp\left(-\frac{z_*}{H}\right); \quad z_* = H \ln\frac{\rho_0 V_0^2}{\sigma_*};$$
$$\nu = \frac{3c_x \rho_0 H}{4\rho_n R_0 \sin\alpha}; \quad C = \left(\frac{3c_x R_0 \sin\alpha}{8H}\right)^{1/2}; \quad (4)$$

$$r = \exp\left(\frac{z_* - z}{H}\right) - 1; \quad \tilde{r} \approx \frac{4C^2}{b}. \quad (5)$$

Furthermore, c_x is the coefficient of the aerodynamic drag; $\tilde{r}$, $\tilde{z}$, and $\tilde{V}$ are the characteristic values of r, z and V, which correspond to the value $R = 2R_0$, i.e., to the time moment when the nucleus is completely fragmented and its radius is equal to the doubled value of the initial radius [9].

Under these conditions, for $R_0 \geq 100$ m, we have according to (4) that $b \ll \nu \ll 1$. Therefore, using (5), in the region close to the end-point of the deceleration trajectory, i.e., at $z_* \gg \tilde{z} \gg z$, we have for the fragmented nucleus that $r \gg \tilde{r} \gg 1$. Hence, according to (2) and (3), the law for the velocity variation of the fully fragmented nucleus in the region $z \ll \tilde{z} \ll z_*$ has the following form:

$$V = \tilde{V}\exp\left[-\frac{2b^2}{3c_x C^2}(r^2 - \tilde{r}^2)\right] = V_0 \exp\left(-\frac{2b^2}{3c_x C^2} r^2\right), \quad (6)$$

where V_0 is the initial orbital velocity of the nucleus.

From (5) and (6), it follows that the principal deceleration of the nucleus (the decrease in its velocity from $V_1 = 0.9V_0$ to $V_2 = 0.1V_0$) occurs at $r_2^2(z_2) = 9r_1^2(z_1)$, i.e., in the trajectory segment lying, according to (5), in the altitude range

$$|\Delta z| = |z_2 - z_1| = H \ln\frac{1+r_1}{1+r_2} \approx H \ln\frac{r_1}{r_2} \approx 0.7H. \quad (7)$$

Using (6), we can also obtain the explicit expression for the characteristic maximal ultimate value of $r = r_0$ [9] at which the velocity of the nucleus in the form of the fragmented mass falls to the value on the order of the sound velocity a_0 in the environmental atmosphere:

$$r_0 = \frac{C}{b}\left(\frac{3c_x}{2} \ln\frac{V_0}{a_0}\right)^{1/2}. \quad (8)$$

According to (4), (5) and (8), the minimum altitude corresponding to the value of $r = r_0$ is

$$z_0 = z_* - H\ln(1 + r_0)$$
$$= H \ln\left\{\frac{\nu}{C}\left[\frac{2}{3c_x \ln(V_0/a_0)}\right]^{1/2}\right\}. \quad (9)$$

Admitting $\sigma_* = 10^4$ dyn/cm^2, $R_0 = 1$ km $= 10^5$ cm, $\rho_n = 0.5$ g/cm^3, $c_x = 1$, $\sin\alpha = 0.5$, $H = 1.5 \times 10^7$ cm, $a_0 = 10^6$ cm/s from (1), (3)–(5), (8) and (9) we find $\nu = 4.5 \times 10^{-5}$, $z_*/H = 8$, $b = 1.3 \times 10^{-8}$, $C = 3.5 \times 10^{-2}$, $\tilde{r} = 4 \times 10^5$, $r_0 = 7 \times 10^6$, $R(r_0) = 12R_0$, $z_0 = -8H = -1200$ km, $\rho_a(z_0) = 3 \times 10^{-5}$ g/cm^3.

Thus, the aerodynamic fragmentation of the cometary nucleus and the spread of the fragmented mass in the transverse direction during the nucleus motion through the solar chromosphere and photosphere is completed near the point $z = z_0$. This occurs

by the deceleration of the fragments of the nucleus and thermalization of their kinetic energy in a relatively very thin sheet with thickness $\Delta z \approx 0.7H \approx 100$ km. This implies that the process of transformation of the nucleus in the zone under consideration with the thickness Δz has a pulsed, sharply explosive character with a duration of about 0.5 s. We can compare this time with the characteristic duration of the pulsed explosive phase of solar flares on the order of 1–10 s. This phase is associated with the initial phase period of the rearrangement of the magnetic field and electric currents in the active zone of the solar atmosphere (see [12, 13] and references therein).

Since the specific energy release in the region of the nucleus explosion near the solar surface, being on the order of $V_0^2/2 = 10^{15}$ erg/g, significantly exceeds the effective heat $Q_s = 10^{10}$–10^{11} erg/g of sublimation of the cometary matter, the process of sublimation of molecules from the fragments of the cometary nucleus cannot affect their temperature. Under these conditions, the deceleration of the fragmented flattened nucleus and transformation of its kinetic energy into thermal energy acquires a volume character and is accompanied not only by evaporation of the entire mass but also by ionization of atoms due to the strong rise of temperature of the entire mass. Estimations show that the initial temperature of plasma formed in the explosion region is $T_0 = 10^7$ K.

The energy E_e released in the explosion region is determined by the initial mass M_0 of the nucleus entering into the solar atmosphere and causing the explosion and by the mass ΔM_a of the initial atmospheric gas in the explosion region. The calculation of this mass, carried out on the basis of (1), (3), (5) and (7), shows that $\Delta M_a \approx M_0$, so that we have

$$E_e = \frac{0.8M_0\Delta M_a V_0^2}{2(M_0 + \Delta M_a)} = \frac{4}{15}\pi\rho_0 R_0^3 V_0^2. \qquad (10)$$

For a comet similar to the Halley 1986 III comet at the density and radius of the nucleus $\rho_n = 0.5$ g/cm^3 and $R_0 = 5 \times 10^5$ cm, respectively, we obtain, according to (10), $E_e = 10^{32}$ erg. This value corresponds to the total energy of large solar flares. The relevant power of the energy release in the explosion zone is on the order of 10^{32} and 10^{29} erg/s, respectively, for the pulsed phase while averaging over the characteristic duration of observable solar flares on the order of 10^3 s that corresponds to the characteristic size of the developing explosion region of 10^{10} cm.

It is noteworthy that the explosive-like release of the kinetic energy of the fragmented flattened nucleus in the thin subphotosphere layer Δz, being accompanied by arising hot plasma and high pressures (on the order of 10^6–10^7 bar, which exceeds the pressure of the surrounding gas 10^5–10^6 times), will also cause generation of strong shock waves, acceleration of electrons and ions at the fronts of these waves, ejection of the hot matter into the chromosphere and corona, and, hence, bursts of X-rays and radiowave radiation from the Sun. Supernova flares (the energy release of 10^{50}–10^{51} erg, the power on the order of 10^{44} erg/s) due to the pulsed release of the gravitational energy of stellar matter, extremely rapidly falling to the center down to the zone of abrupt stopping and generating a strong shock wave, are certain analogues of the solar-flare mechanism under consideration.

Similar processes, but at significantly lower energies, occurred at the explosion of a space body, a large meteoroid, in the Earth's atmosphere on June 30, 1908 (Tunguska event [8, 9]), and in the collision of the Shoemakers–Levy 9 comet with Jupiter on July 16–22, 1994 [10, 11]. In addition, explosive processes of such a kind can also serve, in principle, as a trigger for some observable solar flares associated with pulsed release of the energies of magnetic fields and electric currents generated and transformed into explosive energy not only in the chromosphere and corona near sunspots but also in the photosphere due to developing eruptive processes of different nature therein (see [13, pp. 3, 7]).

Thus, the intense aerodynamic fragmentation of comet-like bodies within the solar chromosphere is completed by the explosive evaporation of the fragmented flattened mass in the relatively very thin subphotosphere layer. The amount of energy of such an explosive high-temperature process and its expected observational manifestations correspond to those of solar flares. This implies that solar flares can occur not only according to known electrodynamic scenarios, i.e., by the pulsed release of the energy of magnetic field and electric currents in the vicinity of solar spots, but also by the explosive-like release of the kinetic energy of cosmic bodies penetrating the solar photosphere. Coordinated observations of the Sun and near-solar comet-like bodies with high space–time resolution in the wide range of the spectrum including the optical, X-ray, and radiowave ranges seem to be foremost in the further studying and solving of the problem of solar flares.

ACKNOWLEDGMENTS

The authors are grateful to Academician A.A. Boyarchuk for his interest and useful remarks.

REFERENCES

1. P. R. Weissman, Icarus **55**, 448 (1983).
2. B. G. Marsden, Astron. J. **98**, 2306 (1989).
3. R. M. MacQueen and O. C. St. Cyr, Icarus **90**, 96 (1991).
4. M. E. Bailey, J. E. Chambers, and G. Hahn, Astron. Astrophys. **257**, 315 (1992).

5. COSPAR Inf. Bull. **142**, 21 (1998).
6. A. M. Mikisha and M. A. Smirnov, Vestn. Ross. Akad. Nauk **69**, 327 (1999).
7. S. S. Grigoryan, F. S. Ibodov, and S. Ibadov, Dokl. Akad. Nauk **354**, 187 (1997) [Phys. Dokl. **42**, 262 (1997)].
8. S. S. Grigoryan, Dokl. Akad. Nauk SSSR **231**, 57 (1976) [Sov. Phys. Dokl. **21**, 603 (1976)].
9. S. S. Grigoryan, Kosm. Issled. **17**, 875 (1979).
10. S. S. Grigoryan, Dokl. Akad. Nauk **338**, 752 (1994) [Phys. Dokl. **39**, 713 (1994)].
11. V. E. Fortov, Yu. N. Gnedin, M. F. Ivanov, *et al.*, Usp. Fiz. Nauk **166**, 391 (1996) [Phys. Usp. **39**, 363 (1996)].
12. A. T. Altyntsev, V. G. Banin, G. V. Kuklin, and V. M. Tomozov, *Solar Flares* (Nauka, Moscow, 1982).
13. B. V. Somov, Izv. Akad. Nauk, Ser. Fiz. **59**, 2 (1995).
14. G. S. Ivanov-Kholodnyĭ and G. M. Nikol'skiĭ, *Sun and Ionosphere* (Nauka, Moscow, 1969).
15. J. M. Greenberg, H. Mizutani, and T. Yamamoto, Astron. Astrophys. **295**, L35 (1995).

Translated by S. Ibadov

Doklady Physics, Vol. 45, No. 9, 2000, pp. 467–471. Translated from Doklady Akademii Nauk, Vol. 374, No. 1, 2000, pp. 44–48.

MECHANICS

Numerical and Analytical Investigation of Steady-State Flow of Viscous Fluid in a Plane Confuser

L. D. Akulenko*, D. V. Georgievskiĭ, S. A. Kumakshev*, and S. V. Nesterov***

Presented by Academician D.M. Klimov February 21, 2000

Received February 22, 2000

1. We consider the Hamel (Jeffry Hamel) problem for the steady-state radial flow of an incompressible viscous fluid in a plane confuser [1–5]. This is one of a few non-one-dimensional problems, which admits an exact self-similar solution. Its complete investigation is of undoubted practical and theoretical interest.

Thus, let the flow of a fluid with the density ρ and kinematic viscosity ν occur in a plane domain $|\theta| < \beta$ (2β is the angle between the walls of a confuser) and let Q be the intensity of the outflow at the origin of a Cartesian coordinate system. It is more convenient to describe the motion in polar coordinates (r, θ). Because the dimensionalities of Q and ν coincide in the plane case, the maximum number of characteristic quantities with independent dimensionalities equals two. Therefore, it is impossible to completely reduce all the equations to the dimensionless form. The only dimensionless combination is the Reynolds number $\mathrm{Re} = Q/\nu$.

Then, the components v_r, v_θ of the velocity vector and v_{rr}, $v_{\theta\theta}$, $v_{r\theta}$ of the strain-rate tensor can be represented in the form

$$v_r = -\frac{Q}{r}V(\theta), \quad v_\theta \equiv 0,$$
$$v_{rr} = -v_{\theta\theta} = \frac{Q}{r^2}V(\theta), \quad v_{r\theta} = -\frac{Q}{2r^2}V'(\theta), \tag{1}$$

which provides for incompressibility. The components of the stress tensor σ_{rr}, $\sigma_{\theta\theta}$, σ_{zz}, $\sigma_{r\theta}$ have the following form:

$$\sigma_{rr,\theta\theta} = -p \pm \frac{2\rho Q^2}{r^2\mathrm{Re}}V(\theta), \quad \sigma_{zz} = -p,$$
$$\sigma_{r\theta} = -\frac{\rho Q^2}{r^2\mathrm{Re}}V'(\theta), \tag{2}$$

where p is pressure. An unknown function $V(\theta)$ appearing in (1) and (2) is determined as the solution to the nonlinear boundary problem with the additional integral condition of the constant flow rate [1–3]:

$$V'' + 4V - \mathrm{Re}V^2 = C,$$
$$V(\pm\beta) = 0, \quad \int_{-\beta}^{\beta} V(\theta)d\theta = 1. \tag{3}$$

The constant C in (3) is subject to our a choice. It enters into the expression for pressure

$$p(r, \theta) = \frac{1}{2}\frac{\rho Q^2}{\mathrm{Re}}r^{-2}(C - 4V(\theta)),$$
$$C = V''(\pm\beta), \tag{4}$$

where V and C depend on β, Re. The solution to problem (3) is symmetric with respect to $\theta = 0$.

2. There are analytical investigations of problem (3) [2, 3] in which elliptic functions and elliptic integrals were used as a basis. These investigations are related to the analysis of the behavior of roots of a cubic equation containing known and unknown parameters. Attempts to construct the explicit analytical solution to problem (3) for arbitrary values of β and Re have failed because of a need to determine roots for the system of two transcendental equations with respect to two unknown integration constants.

For the convenience of numerical and analytical calculations, we introduce a normalized argument x using the formula $\theta = \beta(2x - 1)$ and the function $y(x) = 2\beta V(\theta)$. As a result, problem (3) can be rewritten in the form

$$y'' + a^2y - by^2 = \lambda,$$
$$y(0) = y(1) = 0, \quad \lambda = 8\beta^3C;$$
$$z' = y - 1, \quad z(0) = z(1) = 0; \tag{5}$$
$$a^2 = (4\beta)^2, \quad b = 2\beta\mathrm{Re}.$$

The variable z appearing in (5) corresponds to the quadrature in (3). Boundary value problem (5) is equiv-

* *Institute of Problems in Mechanics, Russian Academy of Sciences, pr. Vernadskogo 101, Moscow, 117526 Russia*

** *Moscow State University, Moscow, 119899 Russia*

alent to the following isoperimetric variational problem [λ is the Lagrange multiplier, $y(0) = y(1) = 0$]:

$$J[y] = \frac{1}{2}\int_0^1 \left(y'^2 - a^2y^2 + \frac{2}{3}by^3\right)dx \longrightarrow \min_y,$$
$$I[y] = \int_0^1 y(x)dx = 1. \tag{6}$$

Variational estimates for $y(x)$ can be constructed on the basis of (6). Solutions to problems (5) and (6) are symmetric with respect to $x = 1/2$.

Initially, we derive approximate analytical expressions for $y(x)$ in the case of various values of parameters a and b, i.e., β and Re.

2.1. We consider a case where $\mathrm{Re} \ll 1$, which is realized in the slow motion of a very viscous material in various technological processes (extruding metallic plate and pressing out of various solutions, etc.). Using expansions in powers of Re^n or the successive approximation method, we can calculate approximate values of the unknowns $y(x)$ and λ at arbitrary β ($0 < \beta < \pi$). At each nth step, we need to solve a linear boundary value problem; in particular, we have [2]

$$y_0(x) = \alpha(l\cos\alpha f + m),$$
$$y_1(x) = \frac{l}{4}\left(\frac{l}{12}(\sin(2\alpha - 2\alpha\cos 2\alpha) + m(\alpha\cos\alpha - (1-\alpha^2)\sin\alpha)\right)y_0$$
$$-\frac{l\alpha}{4}\left(\frac{l}{6}(\cos 2\alpha f - \cos 2\alpha) + m\alpha(f\sin\alpha f - \sin\alpha)\right), \tag{7}$$
$$l = (\sin\alpha - \alpha\cos\alpha)^{-1}, \quad m = -l\cos\alpha,$$
$$\alpha = 2\beta, \quad f = 2x - 1.$$

Functions $y_n(x)$, $n \geq 2$, can be calculated in a similar manner. Unknown coefficients λ_n are derived from (7) by differentiation of $y_n(x)$ with respect to x at $x = 0, 1$ [for example, $\lambda_0 = y_0''(0) = 32\beta^3 m$, $\lambda_1 = y_1''(0)$]. Calculations are unreasonable at $n \geq 2$ because expressions for $y_n(x)$ become awkward and, if $\mathrm{Re} \sim 1$, inapplicable due to their low accuracy.

2.2. We now investigate the problem at $\mathrm{Re} \gg 1$ and $\beta \sim 1$. Formally, the discontinuous (at end points $x = 0, 1$) solution $y_\infty(x) \equiv 1$, $0 < x < 1$, takes place at $\mathrm{Re} = \infty$. This corresponds to passage to the limit of a perfect fluid. The existence of a large parameter b (or the small one b^{-1} at the higher derivative) requires the application of asymptotic methods [6, 7]. To the first approximation, singular perturbation methods allow us to construct the asymptotic solution [2] that can be represented in the very suitable form

$$y^{(1)}(x) = 1 - 6(1 + \cosh(\operatorname{arccosh} 5\sqrt{b/2}(1 \pm (2x-1))))^{-1},$$
$$y^{(1)'}(0) = \gamma^{(1)} = \sqrt{4b/3}, \tag{8}$$
$$y^{(1)''}(0) = \lambda^{(1)} = -b.$$

The upper (plus) and lower (minus) signs in (8) correspond to the intervals $0 \leq x \leq 1/2$ and $1/2 \leq x \leq 1$, respectively. It follows from (8) that, as $b \longrightarrow \infty$, the function $y^{(1)}(x) \approx 1 - 0$ almost everywhere in the interval $0 < x < 1$, the boundary conditions being met at $x = 0, 1$. Deviations of $y^{(1)}(x)$ from 1 are exponentially small values in $\sqrt{b}$. Expression (8) ensures satisfactory accuracy at $b \sim 10^4$; i.e., $\mathrm{Re} \sim 10^4$–10^5 if $\beta \sim 0.1$–1.

2.3. Let $\mathrm{Re} \sim 1$, $0 < \beta \ll 1$, which corresponds to a confuser with almost parallel walls. We have that in Eq. (5) $a, b \ll 1$; moreover, regular expansions in powers of β^n lead to the approximation of the solution $y(x)$ by polynomials in x:

$$y_0(x) = 6x(1-x),$$
$$y_1(x) = \frac{6\mathrm{Re}}{35}x(14x^5 - 42x^4 + 35x^3 - 9x + 2), \tag{9}$$

etc. The principal (of the zero order in β) term of expansion (9) corresponds to the Poiseuille flow, i.e., to the parabolic profile of the flow velocity. The degree N of the polynomial, $N = 2 + 4n$, increases very rapidly. We can also apply the method of successive approximations.

2.4. Let $\beta \ll 1$, but $\beta\mathrm{Re} \sim 1$. Then, to the first approximation, the boundary value problem (5) does not contain the term a^2y. However, integrating (5), as in the general case, we arrive at elliptic functions, and solving the problem calls for the application of numerical methods. A certain simplification consists in the fact that this solution depends on only one parameter b: $y = y_0(x, b)$, $\lambda = \lambda_0(b)$.

3. For practically important values of $\mathrm{Re} = \chi$, $\chi \sim 0.1 - 10^3$, $\beta \sim 0.1 - \frac{\pi}{2}$, the application of formulas (7)–(9) leads to large errors. This necessitates the development of an efficient numerical and analytical approach to solving problem (5). A modified method of the Newtonian type [8] is proposed for the accelerated convergence in combination with the procedure of the continuation over the parameters. This method makes it possible to obtain a high precision values of desired quantities by one to two iterations at relatively small computational expenditures. As a result, a practically

exact solution is obtained with relative accuracy on the order of 10^{-5}–10^{-7}, which can be improved, if necessary. The algorithm of the method consists in calculating deficient values $\gamma = y'(0)$ and $\lambda = y''(0)$, which determine the function $y(x)$ as the solution to the Cauchy problem (5) for fixed a and b, i.e., β and χ.

Sufficiently accurate estimates γ_0 and λ_0 of aforementioned quantities γ and λ are assumed to be known at the initial stage of the algorithm. They can be found with the use of the variational approach based on functionals (6) at the appropriate choice of the tentative function $y^*(x)$ [8]. As calculations show, the function $y(x, a, b)$ has a relatively simple form. The continuation procedure with respect to parameters β, χ (or a, b) is rather convenient. In particular, at a fixed value $a = 4\beta > 0$, it is recommended to take $\gamma_0 = 8\beta^2 l \sin 2\beta$, $\lambda_0 = 32\beta^3 m$ [see (7)] as initial approximations to $\gamma_0(\chi_1)$ and $\lambda_0(\chi_1)$ when $\chi_1 > 0$ is sufficiently small. The recurrence scheme with the accelerated convergence is used for the calculation of $\gamma_1 = \gamma(\chi_1)$, $\lambda_1 = \lambda(\chi_1)$ with the desired accuracy, which are adopted as initial approximations to $\gamma_0(\chi_2)$, $\lambda_0(\chi_2)$, etc. The existence of sets $\{\gamma_k\}$ and $\{\lambda_k\}$ of sufficiently accurate values for γ_k and λ_k ($k = 1,2,\ldots$) allows us to expand the interval $\delta\chi_{k+1} = \chi_{k+1} - \chi_k$ by a polynomial (usually, linear or quadratic) extrapolation of initial approximations $\gamma_0(\chi_{k+1})$ and $\lambda_0(\chi_{k+1})$.

The recurrence scheme for the refinement of desired quantities $\gamma(\chi)$ and $\lambda(\chi)$ at the first and subsequent steps consists in integration of two Cauchy problems for 6th-order systems or for one 9th-order system. Each of these two problems is described by Eqs. (5) with the conditions

$$y(0) = z(0) = 0, \quad y'(0) = \gamma_n(\chi), \quad \lambda = \lambda_n(\chi), \quad n = 0, 1, \ldots, \chi \in \{\chi_k\}, \tag{10}$$

and equations for the sensitivity functions v, w, and u, s, i.e., derivatives of the solutions $y(x)$, $z(x)$ with respect to γ and λ,

$$\begin{aligned} v'' + a^2 v - 2byv &= 0, \quad w' = v, \\ v(0) = w(0) = 0, &\quad v(0) = 1; \\ u'' + a^2 u - 2byu &= 1, \quad s' = u, \\ u(0) = u'(0) = s(0) &= 0. \end{aligned} \tag{11}$$

The Cauchy problems (5), (10), and (11) are integrated simultaneously or separately, thus, the functions $y_n(x)$ and $z_n(x)$ are determined. The refinement of the quantities $\gamma_n(\chi)$ and $\lambda_n(\chi)$ is possible if the functions y_n, z_n, v_n, w_n. u_n, and s_n are specified at the end point $x = 1$ for $\chi \in \{\chi_k\}$. The standard scheme of the Newtonian method has the form

$$\gamma_{n+1}(\chi) = \gamma_n(\chi) + \delta\gamma_n(\chi),$$

$$\lambda_{n+1}(\chi) = \lambda_n(\chi) + \delta\lambda_n(\chi),$$

$$\delta\gamma_n = -[y_n(1)s_n(1) - z_n(1)u_n(1)]\Delta_n^{-1}(1), \tag{12}$$

$$\delta\lambda_n = [y_n(1)w_n(1) - z_n(1)v_n(1)]\Delta_n^{-1}(1), \quad n = 0, 1, \ldots;$$

$$\Delta_n(x) = v_n(x)s_n(x) - u_n(x)w_n(x), \quad \Delta_n(1) \neq 0. \tag{13}$$

The recurrence process over n (12), (13) is continued until the required accuracy is attained; i.e., until the sufficient smallness of residues $y_n(1)$ and $z_n(1)$, is attained. At each step, a detailed check of the algorithm convergence is required, which he determinant $\Delta_n(1)$ [see (13)] of the matrix for the sensitivity coefficients (11). The distinctive feature of the modification proposed for the accelerated-convergence method is an additional check of the convergence over abscissas ξ_n and η_n, i.e., over quantities $|\varepsilon_n|$ and $|\mu_n|$:

$$\begin{aligned} \varepsilon_n &= 1 - \xi_n, \quad \mu_n = 1 - \eta_n; \\ \xi_n &= \arg y_n(x), \quad \eta_n = \arg z_n(x). \end{aligned} \tag{14}$$

Values of ξ_n, η_n are the roots (zeros) of the functions $y_n(x)$ and $z_n(x)$, which are nearest to $x = 1$. Constructively verified conditions $|\xi_0|, |\mu_0| \ll 1$; $|\varepsilon_n|, |\mu_n| \longrightarrow 0$ testify to both the existence of a desired solution to boundary value problem (5) and the convergence of algorithm (5), (10)–(13), which has an accelerated (quadratic) character. In this case,

$$\begin{aligned} y_n(1) &= -\gamma_n\varepsilon_n, \quad |\varepsilon_{n+1}| \sim \varepsilon_n^2, \\ |\mu_{n+1}| \sim \mu_n^2, &\quad z_n(1) = -\mu_n, \quad n = 0, 1, \ldots \end{aligned} \tag{15}$$

The convergence is determined by the smallness of the moduli of quantities $\varepsilon = \varepsilon_0$ and $\mu = \mu_0$, i.e., by the proximity of abscissas ξ_0 and η_0 to the point $x = 1$. This proximity is provided by the successful choice of the initial approximation $\gamma_0(\chi)$, $\lambda_0(\chi)$, $\chi \in \{\chi_k\}$, i.e., by the appropriate choice of the step $\delta\chi_k$ or by extrapolation. In addition, the fulfillment of the condition $|\Delta_n(1)| \geq D > 0$ [see (13)] is required. A noticeable violation of the results of estimates (14) and (15) calls for an additional analysis usually related to the degeneration property of standard algorithm (12): $\Delta_n(1) \approx 0$ (e.g., at $\beta \longrightarrow \frac{\pi}{2}$, see below). Simultaneous determination of residues $y_n(1)$, $z_n(1)$ and ε_n, μ_n allows us to carry out efficient high-accuracy calculations of the desired parameters $\gamma(\chi)$, $\lambda(\chi)$ for an arbitrary fixed value $0 < \beta < \frac{\pi}{2}$. Similarly, the continuation procedure with respect to the parameter β, $\beta \in \{\beta_j\}$ is realized. In the case of a necessity, the dependences $\gamma(\beta, \chi)$ and $\lambda(\beta, \chi)$ can be constructed by continuation over β, χ ($0 < \beta < \pi$, $0 \leq \chi \leq \mathrm{Re}^* < \infty$).

The calculations show that the solution to problem (5) can be found in several (usually 2–3) iterations with a

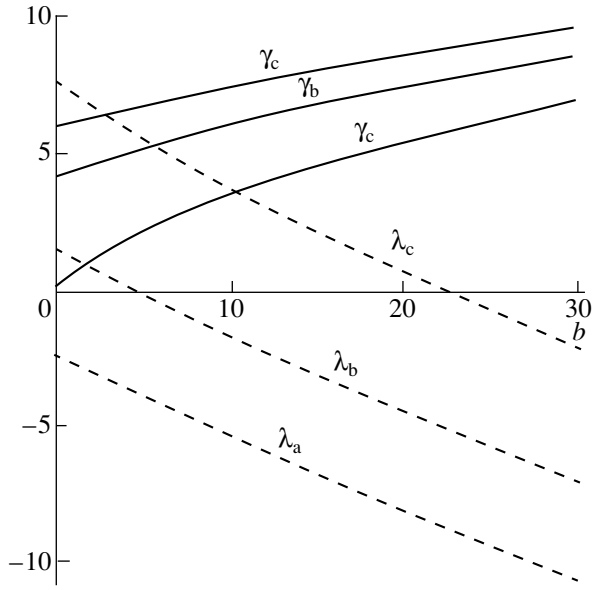

Fig. 1. Families of curves $\gamma(b)$ and $\lambda(b)$ for various values of the confuser aperture angle.

relative accuracy of 10^{-5}–10^{-7} without using extrapolation over χ_k. It should be noted that, at the beginning of the calculation, $\Delta_n(1) \approx 0.1$ (at $\chi \ll 1$); this requires the sufficiently small initial steps $\delta\chi_k \approx 0.01$ over χ. The value of $\Delta_n(1)$ increases with χ, which allows us to increase the step $\delta\chi_k \approx 0.1$–1 practically at once (at $\chi \sim 0.5$). The computational practice shows that the smallness of values ε_0 and μ_0 is a defining factor of the accelerated convergence for the iteration algorithm; usually, ε_0 and $\mu_0 \sim 0.1$ are sufficient.

4. Based on the recurrence algorithm (5), (10)–(12), we have calculated the desired quantities γ, λ and the function $y(x)$ for fixed values of the angle $\beta^\circ \in [1^\circ$–$89.999^\circ]$. The parameter $b = 2\beta\chi$ ($\beta = 2\pi\beta^\circ/360^\circ$) varied within the limits $b \in [0, 30]$ that corresponded to limiting values of the number Reynolds $\mathrm{Re} = b/(2\beta)$: $10 \le \chi^* \le 860$ (depending on taken value of β). The calculations were conducted with the aforementioned accuracy of 10^{-5}–10^{-7} using the residues $y(1)$, $z(1)$, and ε, μ. The results for characteristic values of $\beta^\circ = 1^\circ$, $\frac{180^\circ}{\pi}$, 89° are presented in Figs. 1 and 2. Curves $\gamma(b)$ for the indicated values of β are displayed in Fig. 1 by solid lines *a*, *b*, *c*. The functions $\lambda(b)$ are shown by dashed lines in the scale 1 : 5. Note that $\gamma(0) \longrightarrow 0$ as $\beta \longrightarrow \frac{\pi}{2}$, and $\lambda(0)$ increases as $\Delta(1) \longrightarrow 0$. The behavior of the functions γ and λ at small b completely corresponds to that predicted by analysis conducted in subsection 2.1 [see (7)]. When parameter b increases unlimitedly, curves for $\gamma(b)$ and $\lambda(b)$, in accordance with (8), tend to asymptotic values $\gamma \sim \sqrt{\frac{4b}{3}}$ and $\lambda \sim b$, respectively.

Families of curves $y(x)$ at $b = 0$, 10, 30, which are labeled by numbers *1*, *2*, *3*, respectively, are presented in Fig. 2. Curves *1* and *2* shown in Fig. 2a are close to curves corresponding to the Poiseuille flow [see subsection 2.3, formula (9)], because β and $\beta\chi$ are sufficiently small. The tending of $y^{(1)}(x)$ (8) to an asymptote is observed at $b \approx 30$.

It follows from expressions (5), (7), (8) and shapes of curve families shown in Fig. 2 that, in the case of $\beta < \frac{\pi}{4}$, the functions $y(x)$ are strictly convex upward for all $\mathrm{Re} \ge 0$ (see also the curve λ_a in Fig. 1). At the same time, if $\frac{\pi}{4} < \beta < \pi$, then the central parts of the curves are convex upward, while the parts symmetric with respect to $x = 1/2$ are convex downward near $x = 0.1$ for moderately great values of Re. In other words, there are two symmetric inflection points (see also the curves λ_b and λ_c in Fig. 1). With increasing Re, the entire curve $y(x)$, $0 \le x \le 1$, becomes convex upward due to an effect of the term by^2. Desired flow characteristics (1)–(4) are determined on the basis of known dependences $y(x)$.

Thus, the approach under discussion allows us to carry out the constructive investigation of viscous-fluid

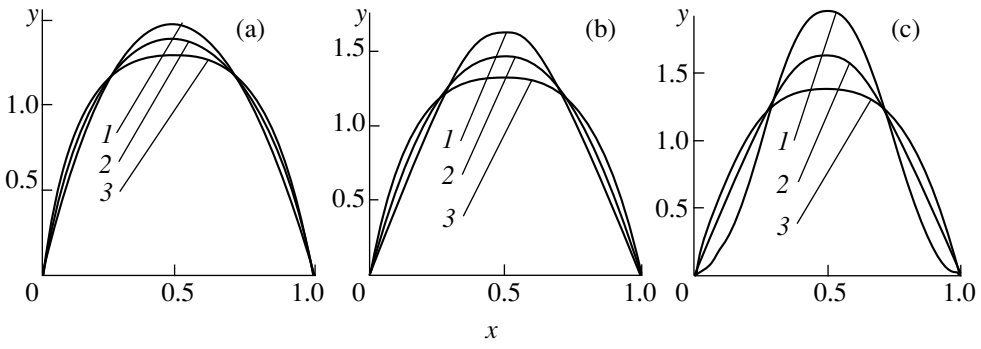

Fig. 2. Families of curves $y(x)$ for various values of both the confuser aperture angle and the Reynolds number.

flows in the wide range of defining parameters. This approach is applicable to the exotic case $\frac{\pi}{2} \le \beta \le \pi$. The results obtained are of independent interest to hydrodynamics of viscous fluids [1–5]. Note that the case of a diffuser ($b < 0$) requires similar detailed analysis. These flows can serve as reference (generating) motions in the case of approximate investigations of visco-plastic flows.

ACKNOWLEDGMENTS

This work was supported by the Russian Foundation for Basic Research, projects no. 99-01-00222, 99-01-00276, and 99-01-00125.

REFERENCES

1. G. Hamel, Jahr-Ber. Deutsch. Math. Ver. **25**, 34 (1916).
2. N. E. Kochin, I. A. Kibel', and N. V. Roze, *Theoretical Hydromechanics* (Fizmatgiz, Moscow, 1963), p. 2.
3. L. G. Loĭtsyanskiĭ, *Mechanics of Liquids and Gases* (Nauka, Moscow, 1978).
4. P. M. Eagles, J. Fluid Mech. **24**, 199 (1996).
5. F. J. Uribe, E. Díaz-Herrera, A. Bravo, and R. Peralta-Fabi, Phys. Fluids **9**, 2798 (1997).
6. M. van Dyke, *Perturbation Methods in Fluid* (Academic, New York, 1964; Mir, Moscow, 1967).
7. S. A. Lomov, *Introduction to the General Theory of Singular Perturbances* (Nauka, Moscow, 1981).
8. L. D. Akulenko and S. V. Nesterov, Prikl. Mat. Mekh. **63**, 646 (1999).

Translated by V. Devitsyn

Doklady Physics, Vol. 45, No. 9, 2000, pp. 472–477. Translated from Doklady Akademii Nauk, Vol. 374, No. 1, 2000, pp. 49–54.

MECHANICS

Simulation of a Possible Process Responsible for the Loss of the Martian Atmosphere

P. V. Plotnikov* and L. V. Shurshalov**

Presented by Academician G.G. Chernyĭ December 27, 1999

Received December 21, 1999

The possibility that Mars lost its dense atmosphere in the far past as a result of a catastrophic collision with a giant dust cloud is shown by methods of mathematical simulation and numerical experiment.

1. Introduction. The martian atmosphere is very rarefied nowadays. The pressure and the density near the planet surface amount to thousandth fractions of terrestrial values. It is generally recognized that the martian atmosphere was much denser in the far past (2–4 billions years ago) and slightly resembled the current terrestrial atmosphere but was composed predominantly of carbon dioxide. The martian climate was reasonably warm and humid. There was a great quantity of water in the stable state. Conserved beds of rivers and traces of extensive floods on the Mars' surface are convincing evidence of these facts. At a certain stage in its history, Mars lost its dense atmosphere by causes so far unknown, the planet temperature abruptly lowered and water in the free state disappeared. There exists an evolutionary scenario explaining the loss of atmosphere on Mars [1]. In the extremely concise and general form, the scenario is the following. At an early stage in the evolution of Mars, the planetary carbon-dioxide cycle was supported, on one hand, by dissolving CO_2 in water and forming carbonate depositions and, on the other hand, owing to a supply of CO_2 in the atmosphere as a result of intense volcanic activity. As far as this activity attenuated, the last-mentioned process acquired a more unidirectional character, the atmosphere became more rarefied, the greenhouse effect weakened, and the temperature lowered until the atmosphere came to its recent state. This theory is not generally recognized because it runs into severe difficulties in explaining certain facts and is not free of inherent contradictions. In particular, there is certain evidence that the change in the martian climate happened relatively fast instead of being a long-term and gradual evolution.

In this study, we propose a new possible explanation for why Mars lost its atmosphere and verify this explanation using a numerical experiment based on a proposed mathematical model. The calculations directly testify to the fact that the planet could have lost its atmosphere in the course of a certain cosmic-scale catastrophic process.

2. Formulation of the problem. The case in point is the simulation of a collision between Mars and a large cloud of small particles, the size of the cloud being comparable with that of the planet. Such a cloud could be formed on the outskirts of Mars as a result of a collision between reasonably large cosmic bodies, for example, asteroids. In the asteroid belt located between the orbits of Mars and Jupiter, there are plenty of such bodies even today, while they were much more plentiful and of still larger sizes in the far past because it is assumed the processes of collision and fragmentation of bodies have been proceeding perpetually in this belt [2]. A large dust cloud can also collide with the martian atmosphere when the nucleus of a certain comet passes in the immediate vicinity of the planet surface.

In the model experiment, we consider a cloud of small particles of identical sizes. To be more precise, we take spherical particles of a radius from 0.1 to 1 mm. In an actual situation, such a cloud could certainly represent a conglomerate of particles and fragments with a great variety of sizes and also have a significant gas component. However, this is not the principal moment for the current problem of the loss by Mars of its atmosphere as a result of interaction with the particle cloud.

In studies [3–8], we develop models and methods to calculate the interaction between large volumes of dust particles and the Earth's atmosphere. Basically, the one-dimensional and two-dimensional problems on the local interactions with the atmosphere were considered for the sizes of dust clouds, which were much smaller than the planet sizes. The currently studied planetary-scale interactions have a number of features making their numerical simulation rather difficult. Above all, there is a large difference in the scales of characteristic

* *Tambov State Technical University, Leningradskaya ul. 1, Tambov, 392620 Russia*

** *Computer Center, Russian Academy of Sciences, ul. Vavilova 40, GSP-1, Moscow, 117967 Russia*

1028-3358/00/4509-0472$20.00

regions to be resolved. On one hand, the development of the process, as a whole, envelopes the spatial region with a characteristic size up to several planet diameters, i.e., thousands of kilometers. On the other hand, there is a relatively thin atmosphere, whose thickness is several tens of kilometers. Moreover, it is necessary to describe and calculate the motion of particles with a size of tenth and hundredth fractions of a centimeter and to take into account the processes of their heating, sublimating, melting, and boiling proceeding at characteristic distances much longer than the atmosphere thickness (hundreds of meters). To overcome these difficulties, we developed an approach based on using nonstructurized finite-difference mesh, the so-called ENO-modification of the Godunov method with a second-order accuracy, and on the explicit isolation of the bow shock wave and the particle-cloud boundary [7].

In study [8], we calculated the model one-dimensional problems of the planetary-scale interactions and confirmed the possibility that the planet atmosphere could have been carried away by a large dust cloud.

In this study, we consider a more realistic two-dimensional axially symmetric formulation of the problem. The planet is taken in the form of a hard ball with the martian radius $R = 3400$ km. The atmosphere is taken in the form of the simplest isothermic exponential model with the pressure and density near the surface coinciding with their terrestrial values but with a different value of characteristic altitude $H_* \approx 22$ km specified by a different value of the martian gravity force. The atmospheric gas is assumed to be air for which its actual thermodynamic properties are taken into account. Particular details of the atmosphere model are not significant in this case. The calculations can be carried out with an arbitrary model of the atmosphere.

It is assumed that a cloud of particles in the form of a cylinder with the radius R_0 and the height L_0 and having the velocity v_0 directed along the cylinder axis approaches the planet center. As the material composition of the particle substance, we considered normal-density ice. In this calculation, we also took into account the processes of ablation, heating, melting, evaporation, and boiling of the particle substance [3, 4], although we ignored those of the radiation transfer. As was shown in [5], the latter are very significant in the quantitative respect, but they do not manifest themselves in the qualitative pattern of the flow. The initial volume fraction α_0 of the particles is taken within the range 10^{-9}–10^{-3}. According to the cosmic scales, these are very large values and exceed the usual concentration of the cosmic dust by many orders of magnitude. Such high values can arise either for a relatively short time as a result of the destruction of bodies, or, possibly, they exist in the most inner domains of the coma of certain comets.

3. The model and the method of investigation. For the model describing the interaction of a large quantity of small particles with an atmospheric gas, we used the well-known model of interpenetrating continua [9] under the assumption that the medium of particles has no proper pressure and the volume fraction of the particles is negligibly low. In this case, the flow of the heterogeneous medium is described by the set of equations for the mass, momentum, and energy of gas phases (the gas is assumed to be nonviscous and non-heat-conducting) and for the particles with allowance for the exchange terms in the right-hand sides of these equations, which describe the interphase interaction. The form of both these equations and the necessary additional relationships are presented in [3–5]. In the same studies, the principle method for solving the problems of the interaction between dust formations and planetary atmospheres is also described. In the two-dimensional variant, the calculation method is described in [7], where details of constructing the adaptive nonstructurized finite-difference mesh are also presented.

4. Results of the numerical experiment. The principal dimensionless parameters specifying the possibility of carrying away the atmosphere and the inverse process, i.e., increasing its mass, are

$$a = \frac{K_0}{|U_0 + U_{\text{atm}}|}, \quad b = \frac{M_0}{M_{\text{atm}}},$$

where K_0 is the initial kinetic energy of the particle cloud, U_0 and U_{atm} are the initial potential energies of the cloud and the atmosphere in the gravitational field, and M_0 and M_{atm} are the initial masses of the particle cloud and the atmosphere, respectively. For large a, it is possible to suggest the probable carrying away of the atmosphere and, for $a < 1$ and not very small b, to suggest a marked increase in its mass.

We consider two sets of initial parameters. In both cases, $R_0 = 1.1R$ (that exceeds the planet radius by approximately a thickness of its atmosphere). The initial radius of each particle amounts to 1 mm. In case (a), $L_0 = 2R$, $v_0 = 40$ km/s (that corresponds approximately to the midpoint of the possible range of relative velocities for cosmic bodies in the Solar system), and $\alpha_0 = 10^{-4}$. In case (b), $L_0 = R$, $v_0 = 5$ km/s, and $\alpha_0 = 10^{-5}$. The calculation begins from an altitude of 400 km above the surface. The parameters a and b turn out to be $a = 65$, $b = 6.8$, and $a = 0.25$, $b = 0.34$, respectively.

Certain results of these calculations are shown in Figs. 1–4. In Fig. 1, we show a fragment of the flow pattern at the initial stage of the interaction process [case (a), $t = 30$ s]. Here, x and r are the axial and radial coordinates, respectively. The center of the planet is placed in the origin of coordinates. The planet surface is shown in the form of a circumference arc. The dashed line indicates the initial altitude of 400 km. We show the distribution of pressure in the upper half-plane and

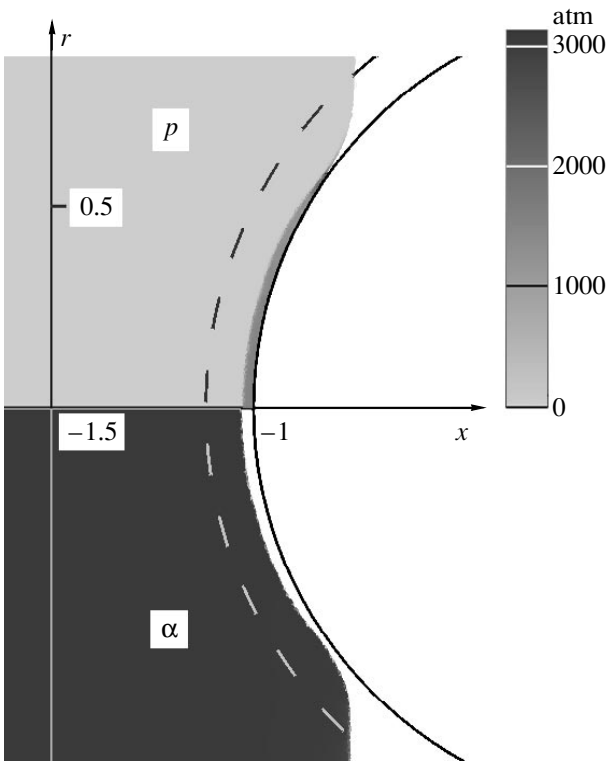

Fig. 1.

the distribution of relative volume fraction $\alpha = \alpha(x, r)/\alpha_0$ (the maximum value $\alpha_{max} = 1.02$) in the lower half-plane. The interaction between the gas and the particles takes place near the planet surface in a narrow region (100–300 m). Outside of this region, the velocities of both the gas and particles are equalized and, apparently, no interaction exists between them. Particles arriving at this region already interact not with the atmospheric gas but with the particle substance evaporated earlier. Therefore, this is the high-velocity gas flow formed as a result of evaporating the particles that, in fact, fall onto the planet and its atmosphere. The incoming flow somehow gathers the atmospheric gas and advances it along the planet surface, the characteristic gas pressure in this case attaining 1.5×10^3 atm. The particles do not reach the planet surface.

Figure 2 shows the same distributions at the time moment $t = 150$ s. Approximately 70% of the dust cloud is already evaporated. An intense shock wave propagates across the still unperturbed part of the atmosphere, being accelerated in the rarefied atmosphere layers. To time moment $t = 200$ s, this wave is collapsed behind the planet and begins to come towards its surface from the opposite side, while enhancing its intensity. In this case, the pressure near the planet surface attains 4 atm. The planet obtains an impact from the rear side. (This effect is curious and worthy of a special

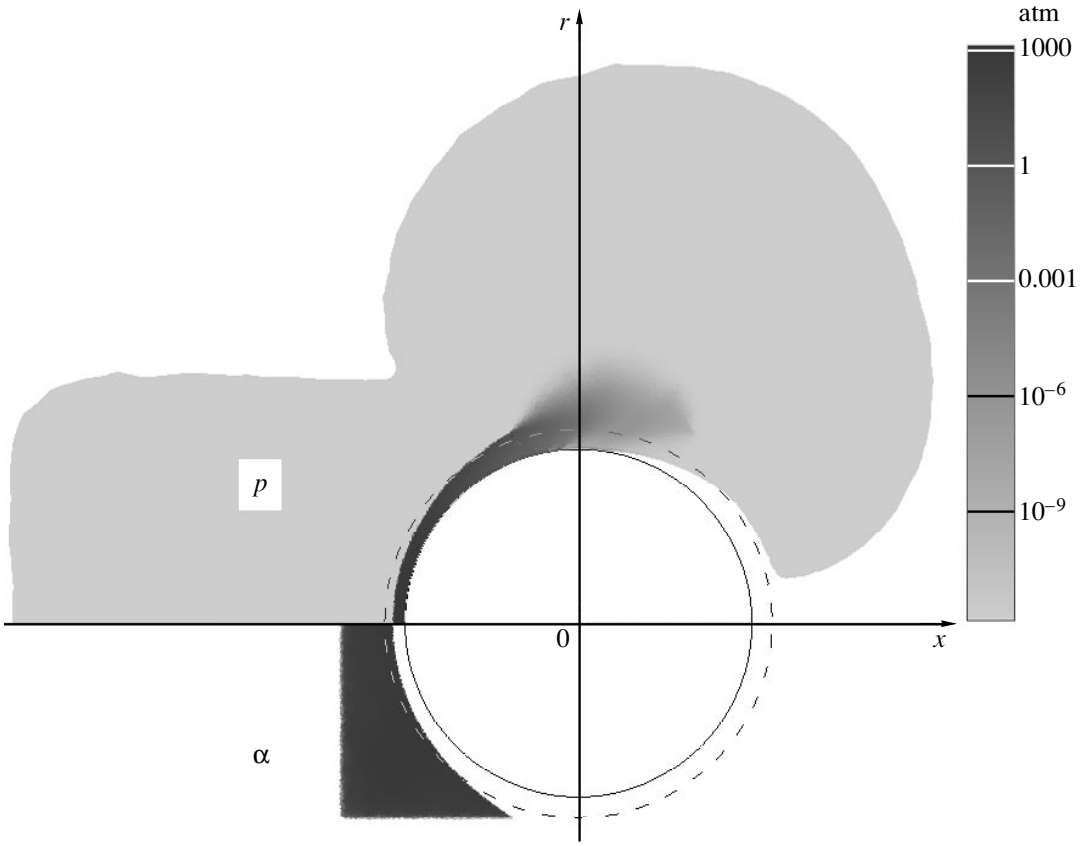

Fig. 2.

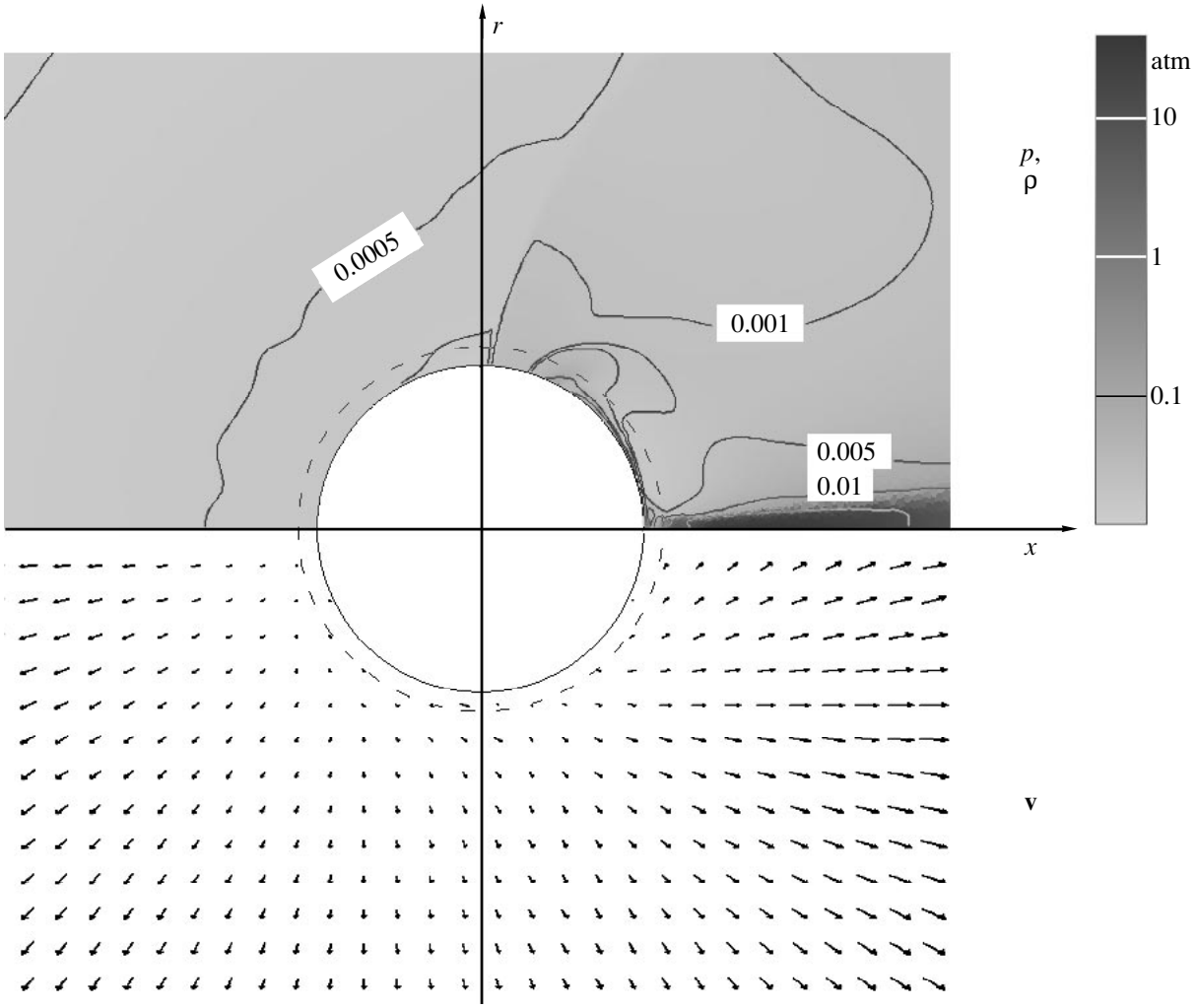

Fig. 3.

additional investigation, possibly, without the presence of the complicating factor of the atmosphere interaction with particles.) Up to this moment, the cloud of particles has lost 96% of its mass. We note that the cloud of particles does not undergo a severe strain in the flow under consideration; only the evaporation wave moves across this cloud.

In Fig. 3, we show the distribution of pressure and the gas-density isolines (in units of the normal atmospheric density) in the upper half-plane and the velocity field in the lower half-plane for $t = 600$ s. The maximum velocity in the region shown amounts to approximately 30 km/s, considerably exceeding the value of the second cosmic velocity (5 km/s) near the martian surface. Therefore, the scattered gas cannot already return to the planet. The density distribution shows that the carrying-away of the atmospheric mass proceeds primarily in the direction of the dust-cloud motion.

In later phases of the process, a complicated flow is observed around the planet with reflections from the symmetry axis and the values of pressure and density being gradually equalized near the surface.

Figure 4 corresponds to the case (b). In this figure, we show the same distributions as in Fig. 3 but for $t = 3000$ s. Here, the maximum velocities in gas (5.3 km/s) also exceed the escape velocity. However, the density distribution is such that an insignificant mass of gas is carried away, so that the atmosphere increases the mass instead of loosing it. Figures 3 and 4, corresponding to approximately the same stage of the process, show the flow after the action of the shock wave on the entire planet surface.

The mass of the remaining part of the atmosphere (not the initial mass but that in the mixture with vapors of particles) with respect to the initial mass of the atmosphere amounts to 1/3 in case (a) and 1.15 in case (b).

In principle, it is possible to formulate the following inverse problem: to find such parameters for the incoming dust cloud such that the given mass of the initial atmosphere could be carried away. In other words, it is

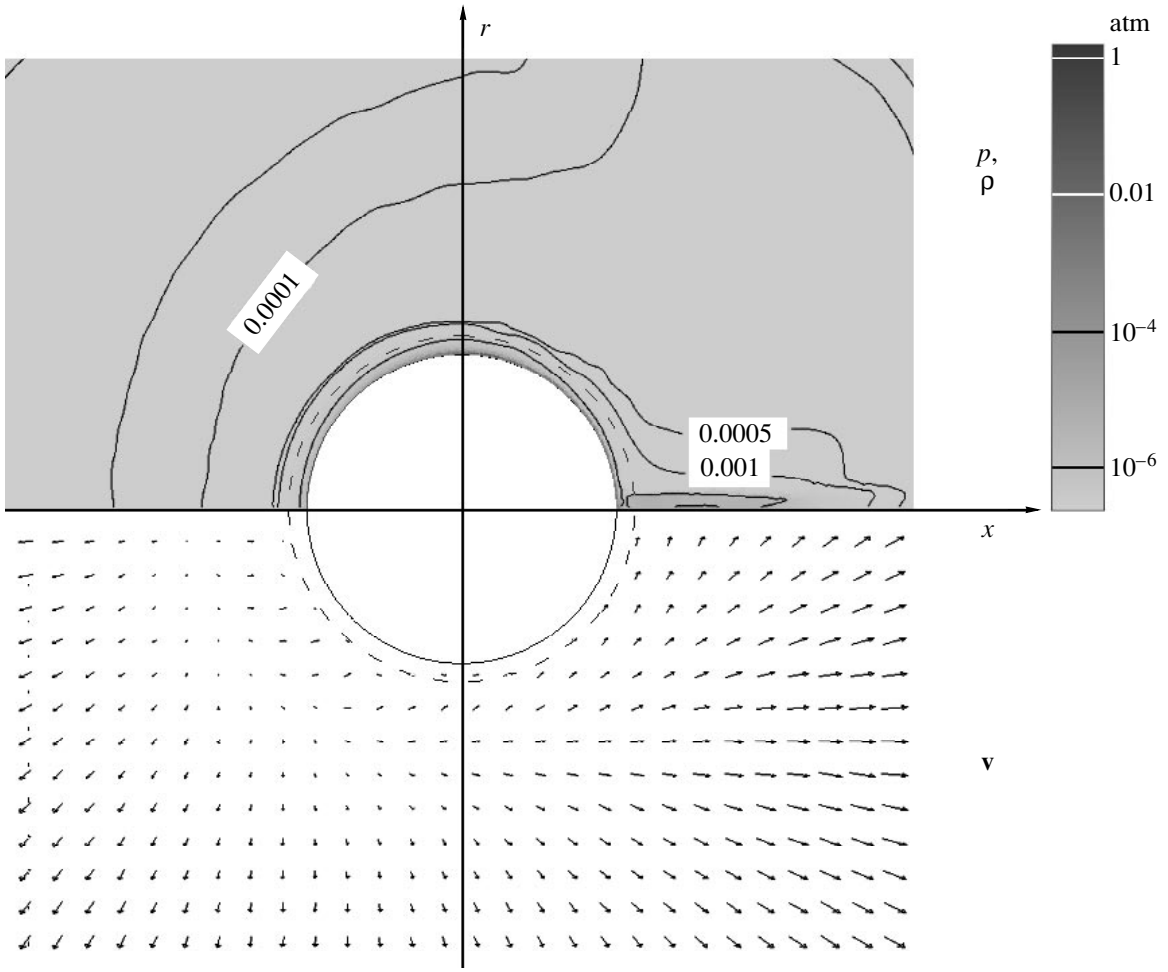

Fig. 4.

possible to find (although ambiguously) the parameters of the dust cloud that caused the loss of the martian atmosphere knowing the current parameters of the martian atmosphere and assuming that in the far past they were such as those on the Earth. After this, we can estimate what processes and bodies could give rise to such a dust cloud.

5. Conclusions. The calculations carried out have confirmed the possibility that a planet (in the case under consideration, Mars) can lose its atmosphere as a result of a collision with a large dust cloud. Although the model used involves many assumptions and rather arbitrary parameters (identical sizes of particles, their spherical shape and ice composition, the value of their initial temperature, the model of dense martian atmosphere, etc.), all these assumptions are not of principle character with respect to the problem formulated of a possibility for Mars to lose its atmosphere. The significant aspect is only the possibility of the appearance of a sufficiently large cloud of particles with a sufficiently high concentration in the vicinity of Mars and a reasonably high velocity of the cloud with respect to the planet. Therefore, it is now necessary to also consider such a possibility in the case of discussing probable mechanisms of the loss by Mars of its atmosphere.

For certain initial parameters of the incoming particle cloud (in particular, for lower velocities), the inverse situation is possible when the atmosphere of the planet can increase its volume and mass as a result of interaction with the cloud of particles. However, in this case, it is natural that the composition of the atmosphere can radically change.

It would be curious to discover at a certain time similar processes in the cosmos. As was shown in [5, 6], these processes must be accompanied by intense but very short, light flashes with a brightness sufficient for detection by modern instruments, even at interstellar distances.

ACKNOWLEDGMENTS

This work was supported by the Russian Foundation for Basic Research, project no. 97-01-00386.

REFERENCES

1. J. B. Pollack, J. F. Kasting, S. M. Richardson, and K. Poliakoff, Icarus **71** (2), 203 (1987).
2. V. S. Getman, *Solar Groundchildren: Asteroids, Comets, Meteoric Bodies* (Nauka, Moscow, 1989).
3. P. V. Plotnikov and L. V. Shurshalov, Zh. Vychisl. Mat. Mat. Fiz. **34**, 117 (1994).
4. P. V. Plotnikov and L. V. Shurshalov, Zh. Vychisl. Mat. Mat. Fiz. **35**, 1233 (1995).
5. P. V. Plotnikov and L. V. Shurshalov, Zh. Vychisl. Mat. Mat. Fiz. **36**, 120 (1996).
6. P. V. Plotnikov and L. V. Shurshalov, Astron. Vestn. **31**, 72 (1997).
7. P. V. Plotnikov, Zh. Vychisl. Mat. Mat. Fiz. **38**, 1943 (1998).
8. L. V. Shurshalov and P. V. Plotnikov, Tr. Mat. Inst. im. V. A. Steklova, Ross. Akad. Nauk **223**, 255 (1998).
9. R. I. Nigmatulin, *Principles of Mechanics of Heterogeneous Media* (Nauka, Moscow, 1978).

Translated by V. Bukhanov

Doklady Physics, Vol. 45, No. 9, 2000, pp. 478–480. Translated from Doklady Akademii Nauk, Vol. 374, No. 1, 2000, pp. 55–57.

MECHANICS

Numerical Simulations of an Effect Produced by a Cold Jet Propagating Opposite to the Incident Supersonic Flow on Resulting Aerodynamic Characteristics of a Blunted Body

Corresponding Member of the RAS V. M. Fomin*, N. D. Malmus, A. A. Maslov*, A. P. Shashkin*, T. A. Korotaeva*, V. F. Chirkashenko*, and Yu. N. Yudintsev***

Received March 3, 2000

Investigations of a supersonic flow of nonuniform gas around different bodies arouses a considerable amount of current interest. Nonuniform character of the incident flow can strongly affect the flow structure in front of the body and, thus, the local and global aerodynamic characteristics of the vehicle (see, e.g., [1–10]).

A jet injected from a body and propagating opposite to a free incident flow represents one of the possible methods of making the flow nonuniform. The effect of a jet propagating oppositely to a flow on its structure was reported in a number of experimental papers [3–7]. It was demonstrated that such a jet considerably affects the aerodynamic characteristics of a body in the flow. Possible regimes of penetration of a cold supersonic jet into the incident flow were studied in [5]. Countercurrent sonic plasma jets were considered in [3, 6]. Papers [5, 6] dealt with the flow around a model body (a cone attached to a cylinder). The blunted cone had a flat end face with the exit hole of the nozzle used for the gas injection. The experiments demonstrated that, for cold and hot jets meeting incident flows from the opposite direction, there exist a short penetration mode (SPM) and a long penetration mode (LPM). These penetration modes are characterized by a certain pressure redistribution along the lateral surface of the cone and by the related changes in the body drag.

Fragmentary experimental data call for generalization based on numerical models. Paper [8] presents an example of calculations for the SPM case. In our paper, we present the results of numerical simulations for formation of different jet-efflux modes and of their effect on the aerodynamic characteristics of bodies in a supersonic flow. The calculations were performed in the framework of the inviscid-gas model by the finite-volume method. We used a central-difference computational scheme, which was explicit with respect to time, implicit with respect to spatial variables, and ensured the second order of approximation [9]. The unsteady problem was solved by the time relaxation technique. As initial data, we used the preliminary solution corresponding to the absence of jet. Boundary conditions in the outer domain corresponded to the incident flow. At the outflow boundary, we take zero second derivatives of flow parameters along the velocity direction. The body was considered as impermeable. The exit jet parameters were calculated by solving the one-dimensional isentropic problem of gas efflux from a vessel for which the exit Mach number, the stagnation temperature, and the Pitot pressure were assumed to be known.

The calculations were performed for the circular cone with a half-angle $\theta_c = 10°$ and a blunted flat end face having a diameter d. A nozzle exit of diameter d_j was situated at the end face of the cut cone. For calculations, we used the incident-flow Mach number $M_\infty = 2.04$, the angle of incidence $\alpha = 0$, $\bar{d} = d/d_j = 3.08$, the Mach number in the nozzle section $M_a = 3.8$, and the relative jet head

$$3 \le (P = P_{0j}/P'_{0f}) < 90.$$

Here, P_{0j} and P'_{0f} are the Pitot pressures in the jet and in the incident flow behind the normal shock wave, respectively. Stagnation temperatures in the jet and in the free flow were considered to be equal.

For the same parameters, we performed experiments in the T-313 ITPM wind tunnel. The dimensions of its working part were 600 × 600 mm. All measurements were taken for the fixed operating mode of the wind tunnel: $M_\infty = 2.04$, $P'_{0f} = 2 \times 10^5$ Pa, and $Re_1 =$

* *Institute of Theoretical and Applied Mechanics, Siberian Division, Russian Academy of Sciences, ul. Institutskaya 4/1, Novosibirsk, 630090 Russia*

** *Rockwell Science Center, Thousand Oaks, CA 91358, USA*

1028-3358/00/4509-0478$20.00

2.5×10^7 m^{-1}. In the course of the experiments, we varied parameter P from 0 to 107. The experimental conditions are described in more detail in [5].

A numerical solution to the problem of penetration of a jet into a supersonic flow propagating oppositely to it and occurring around a blunted body allowed us to simulate two main flow modes, i.e., SPM and LPM. There are also transient modes corresponding to the range of parameters favoring the pulsating unstable penetration regimes.

The length of countercurrent jet L/d normalized by the end-face diameter as a function of parameter P is plotted in Fig. 1. The results of the calculations (curve *a*) are in good agreement with the experimental data from [5] (dots). Regions in Fig. 1 are numbered in the following way: (*1*) SPM; (*2*) SPM-to-LPM transient regime; (*3*) LPM; (*4*) LPM-to-SPM transient regime; and (*5*) SPM.

In Fig. 1 (solid curve *b*), we also show the calculated P dependence of the relative blunted-cone drag C_d/C_{dc}, where C_d and C_{dc} are the drags for the blunted cone with a jet and without it, respectively. This curve was calculated by taking into account the jet thrust. The dashed line in Fig. 1 corresponds to C_{dc}. We can see that the countercurrent jet reduces the cone drag. Moreover, in the SPM-to-LPM transient regime (region *2*), the cone drag decreases by 30% with respect to the jet-free case. Then, the cone and the fluid contour in front of it both form the surface that is close to the surface of minimum drag. In other regions, the cone drag is higher. The decrease in the cone drag in region *5* is explained by attaching a return flow to the end of the cone in the case of the model with the short conic part.

A number of parameters determine the length of jet penetration into the incident flow meeting the jet from the opposite direction: the Mach number in the nozzle section, the parameter P, the jet temperature, parameters characterizing the physicochemical properties of the jet, the angle of the nozzle opening, and ratio $\bar{d} = d/d_j$ of the nozzle exit diameter and that of the blunted region.

In the present paper, we study the P dependence of the jet penetration length. The parameter P can characterize the ratio of specific momenta of the jet and incident flow. At small P, a shock arising in the jet reduces its initial momentum. Hence, the SPM regime forms. In this regime, the jet cannot overpass the thickness of a shock layer between the body and the front shock. It generates a zone of return gas flow. As a result, the flow around the blunted part of the body turns out to be formed by a certain fluid contour. The SPM found by us is illustrated in Fig. 2. The isobaric curves shown in this figure correspond to one of the calculated versions. The calculated structure agrees with the pattern presented in [10], where its rather detailed description is given.

With increasing P, the SPM transforms to the LPM. Under such conditions, the cross-sectional area of the jet decreases and its specific momentum grows according to the relationship

$$P_{0j}^1 \approx \frac{P_{0j}F_a}{F}.$$

Here, F_a and F are the areas of the jet cross section at the nozzle exit and in a current position, respectively. The increased specific momentum allows the jet to pass through the front shock. After entering the free flow, the jet transforms to a periodic structure with a many-barrel shape stabilized by toroidal vortices. Figure 3 illustrates

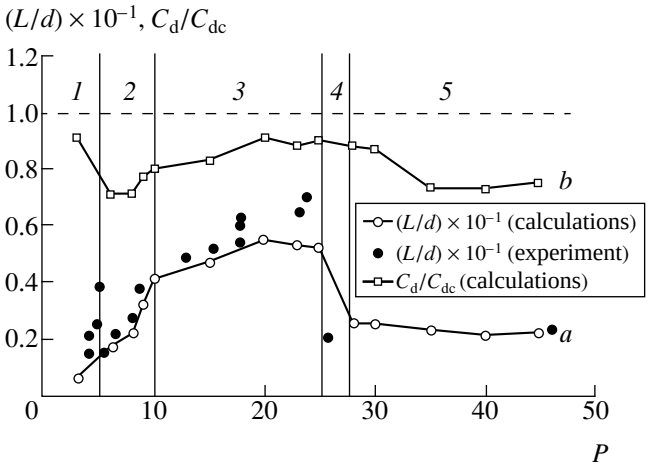

Fig. 1. Drag of a blunted cone with a jet injected oppositely to the flow (normalized to the drag of the blunted cone without a jet) and the length of the jet penetration as a function of parameter P.

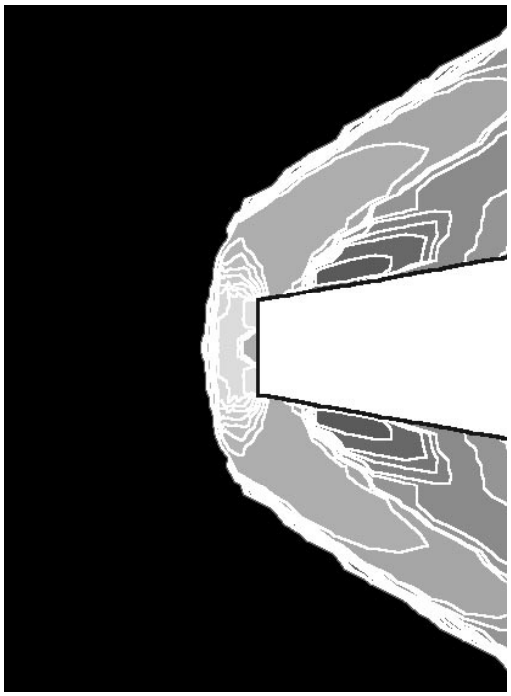

Fig. 2. Isobaric curves for the SPM regime (P = 3).

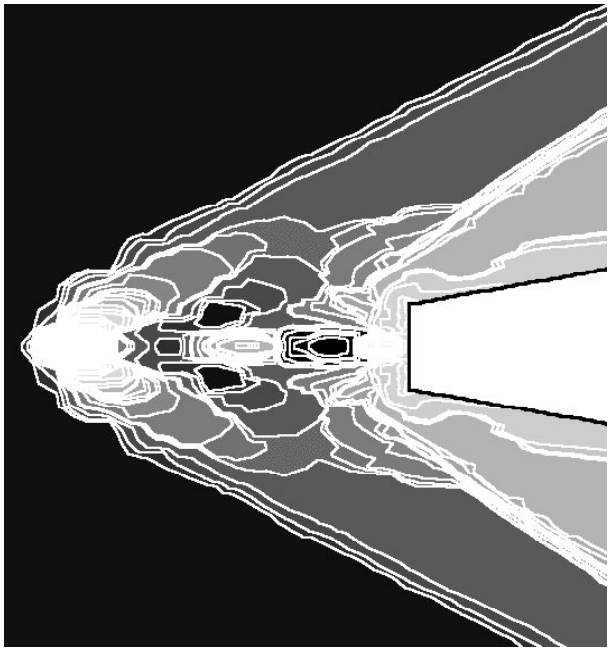

Fig. 3. Isobaric curves for the LPM regime (P = 15).

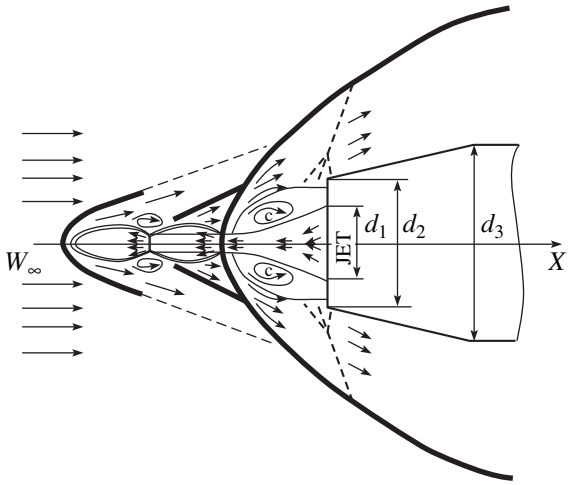

Fig. 4. The pattern illustrating the LPM regime.

the field of isobaric curves in the LPM regime, which were found by the numerical simulation for one of the calculated versions. The LPM flow pattern constructed based on numerous calculations is presented in Fig. 4.

The further increase in P causes the formation of underexpanded jet flow in front of the body. Then, the area of jet cross section grows and P_{0j}^1 becomes equal to P_{0f}', i.e., to the Pitot pressure behind a normal shock wave in the incident flow. In this case, we again observe the SPM.

Our calculations demonstrate that formation of the LPM is mainly determined by the ratio of average pressures $\tilde{n} = \tilde{P}_j / \tilde{P}$. Here, $\tilde{P}$ and $\tilde{P}_j$ are average pressures along the boundary of the jet and inside the jet, respectively. The values of $\tilde{n}$ should lie within the range $0.3 \le \tilde{n} \le 1$; i.e., the condition of jet overexpansion should be met.

In conclusion, we note that the numerical simulations of jet penetration into a supersonic flow met by the jet from the opposite direction allowed us to find the dominant regimes observed in the experiment and to reveal the mechanism of the long penetration mode (LPM) for the jet in the incident flow. The numerical simulations allowed us to show that it is more favorable to implement the SPM-to-LPM transient regime or the LPM with relatively short jet penetration in order to attain the maximum decrease in the wave drag. Our results demonstrate that we can control the structure of a flow around a body and produce a significant effect on its resulting aerodynamic characteristics by using the constitutive parameters of the problem to vary the length of the jet injected oppositely to a supersonic flow.

ACKNOWLEDGMENTS

This work was supported by the Rockwell company (USA) under contract no. B8S413840.

REFERENCES

1. P. K. Tretyakov, V. M. Fomin, and V. I. Yakovlev, in *Proceedings of ICMAR-96*, Novosibirsk, 1996, Part 2, p. 210.
2. G. G. Chernyi, in *Proceedings of the II Workshop on Weakly Ionized Gases* (AAIA, Norfolk, 1998), p. 1.
3. S. Leonov, in *Proceedings of the I Workshop on Weakly Ionized Gases* (USA Air Force Academy, Colorado, 1997), Vol. 1, p. J1.
4. A. Klimov, in *Proceedings of the I Workshop on Weakly Ionized Gases* (USA Air Force Academy, Colorado, 1997), Vol. 1, p. G1.
5. Yu. N. Yudintsev and V. F. Chirkashenko, in *Gas Dynamics and Acoustics of Jet Streams* (Novosibirsk, 1979), pp. 75–106.
6. V. M. Fomin, N. D. Malmut, A. A. Maslov, *et al.*, Dokl. Akad. Nauk **368**, 197 (1999) [Dokl. Phys. **44**, 638 (1999)].
7. J. S. Shang, B. Ganguly, R. Umstattd, *et al.*, in *Proceedings of the XXXVIII Aerospace Sciences Meeting* (Reno, 2000), Paper 2000-0447, p. 10.
8. H. Nomura, S. Aso, and M. Nishida, in *Proceedings of II Japan–Soviet Union Joint Symposium on Computation Fluid Dynamics* (Tsukuba, 1990), pp. 281–284.
9. T. A. Korotaeva, V. M. Fomin, and A. P. Shashkin, Preprint No. 1-96, ITAM SD RAN (Institute of Theoretical and Applied Mechanics, Siberian Division of Russian Academy of Sciences, Novosibirsk, 1996), p. 36.
10. P. J. Finley, J. Fluid Mech. **26**, 337 (1966).

Translated by Yu. Verevochkin

Doklady Physics, Vol. 45, No. 9, 2000, pp. 481–484. Translated from Doklady Akademii Nauk, Vol. 374, No. 2, 2000, pp. 190–193.

MECHANICS

An Efficient Method for Calculating Viscous Flows with a Pronounced Streamline Curvature

Corresponding Member of the RAS N. N. Kalitkin, B. V. Rogov, and I. A. Sokolova

Received May 19, 2000

In [1], the modification of the smooth-channel model was proposed. For viscous flows with moderate and high Reynolds numbers in channels and nozzles with a pronounced curvature of walls, the accuracy of this model is comparable to that provided by the complete Navier–Stokes equations. The set of smooth-channel equations is evolutionary in the longitudinal coordinate with respect to the adapted system of curvilinear coordinates. Therefore, this set can be efficiently solved by the marching methods. One of these methods based on the global iterations along the streamlines and along the longitudinal component of the pressure gradient [1] makes it possible to calculate the flow using a unified approach applicable both within subsonic and supersonic ranges.

In the present study, we propose a method based on the global iterations for the longitudinal component of the gradient of a function that specifies the transverse distribution of pressure. This method is algorithmically simpler [1] and requires approximately half as much memory and processor time for its computer realization. The efficiency of this method is illustrated by the computation of a viscous flow in the Laval nozzle where the gas flow is essentially subsonic at the inlet and supersonic at the outlet. The proposed method can be easily adapted to solving the problems of viscous-gas aerodynamics.

1. Model of flow. We consider the second-order laminar flow of viscous heat-conducting gas in the planar or axially symmetric Laval nozzle. The set of smooth-channel equations [1] in the adapted system of coordinates (ξ, η) with respect to the natural variables has the following form:

the equation for ξ projection of the momentum

$$y^\nu H_\eta\left(\frac{\gamma p u}{T}\frac{\partial u}{\partial \xi} + \frac{\partial p}{\partial \xi}\right) = \frac{1}{\mathrm{Re}_r}$$
$$\times\left\{\frac{\partial}{\partial \eta}\left[\mu y^\nu H_\xi\left(\frac{1}{H_\eta}\frac{\partial u}{\partial \eta} + K_\eta u\right)\right]\right.$$
$$\left. - \mu y^\nu H_\xi H_\eta K_\eta\left(\frac{1}{H_\eta}\frac{\partial u}{\partial \eta} + K_\eta u\right)\right\} \quad (1)$$
$$- y^\nu H_\xi H_\eta \frac{\gamma p \nu}{T}\left(\frac{1}{H_\eta}\frac{\partial u}{\partial \eta} - K_\eta u\right),$$

the energy equation

$$y^\nu H_\eta \frac{\gamma p u}{T}\left[(\gamma-1)u\frac{\partial u}{\partial \xi} + \frac{\partial T}{\partial \xi}\right]$$
$$= \frac{1}{\mathrm{Re}_r}\frac{\partial}{\partial \eta}\left\{y^\nu H_\xi\left[(\gamma-1)\mu u\left(\frac{1}{H_\eta}\frac{\partial u}{\partial \eta} + K_\eta u\right)\right.\right. \quad (2)$$
$$\left.\left. + \frac{\lambda}{\mathrm{Pr} H_\eta}\frac{\partial T}{\partial \eta}\right]\right\} - y^\nu H_\xi \frac{\gamma p \nu}{T}\left[(\gamma-1)u\frac{\partial u}{\partial \eta} + \frac{\partial T}{\partial \eta}\right],$$

the equation for η projection of the momentum

$$\frac{\gamma p u}{T H_\xi}\frac{\partial \nu}{\partial \xi} = -\frac{1}{H_\eta}\frac{\partial p}{\partial \eta} + (K_\xi \nu - K_\eta u)\frac{\gamma p u}{T}, \quad (3)$$

the continuity equation

$$\frac{y^\nu H_\eta}{T}\left[p\frac{\partial u}{\partial \xi} - \frac{p u}{T}\frac{\partial T}{\partial \xi} + u\frac{\partial p}{\partial \xi}\right] = -\frac{\partial}{\partial \eta}\left(y^\nu H_\xi \frac{p\nu}{T}\right)$$
$$+ H_\xi H_\eta\left(y^\nu K_\xi - \frac{\nu \eta y'_w(x)}{\sqrt{1+\eta^2 y'^2_w(x)}}\right)\frac{p u}{T}. \quad (4)$$

Here, H_ξ and H_η are the Lamé parameters of the orthogonal system of coordinates (ξ, η), the ξ-coordinate being longitudinal and the η coordinate being transversal; K_ξ and K_η are the curvatures of the coordinate lines $\xi = \text{const}$ and $\eta = \text{const}$; x and y are the Cartesian (for the plane flow, $\nu = 0$) or cylindrical (axially symmetric flow, $\nu = 1$) coordinates; $y = y_w(x)$ is the contour of the

Institute of Mathematical Modeling, Russian Academy of Sciences, Miusskaya pl. 4a, Moscow, 125047 Russia

1028-3358/00/4509-0481$20.00

nozzle wall; u and v are the projections of the vector of the mean-mass velocity onto the lines η = const and ξ = const; p and T are the static pressure and temperature of gas; and μ and λ are the coefficients of dynamic viscosity and heat conduction. Eqs. (1)–(4) are written on the basis of the equation of state $\rho = \gamma p/T$, where ρ is the density for an ideal gas. We use the dimensionless variables constructed according to the scales: ρ_0 and T_0 are the values on the axis in an initial nozzle cross section; u_0 is the velocity of sound $\sqrt{\gamma R T_0}$, where R is the gas constant; $p_0 = \rho_0 u_0^2$, r_0 is the radius of the critical cross section of the nozzle. We also used the dimensionless combinations $\mathrm{Re}_r = \rho_0 u_0 r_0/\mu_0$ is the Reynolds number, $\gamma = c_{p0}/c_{v0}$ is the ratio of specific heats, and $\mathrm{Pr} = \mu_0 c_{p0}/\lambda_0$ is the Prandtl number.

The set of Eqs. (1)–(4) is elliptic in the subsonic areas of flow and hyperbolic in the supersonic areas. With respect to the longitudinal coordinate ξ, Eqs. (1)–(4) are the first-order differential equations; with respect to the transversal coordinate η, Eqs. (1) and (2) are the second-order differential equations, whereas (3) and (4) are the first-order equations. The mathematical type of these equations specifies the formulation of the boundary conditions.

The domain under study was bounded by the symmetry axis $\eta = 0$ from below, by the hard curvilinear wall $\eta = 1$ from above, by the inlet cross section on the left, and by the outlet cross section on the right.

In the inlet cross section located in the subsonic area, we specify the following parameters for evolutionary Eqs. (1)–(4): the transverse profiles u/u_a (u_a is the velocity at the axis), v/u, T, and also a value of pressure p_a on the axis. The value of the axial velocity, the distribution of pressure in this cross section, and the gas flow rate are determined in the process of solving the problem.

The following boundary conditions are set for Eqs. (1) and (2): at the wall, the adhesion condition for the longitudinal velocity u and the heat-insulation condition $\dfrac{\partial T}{\partial \eta} = 0$; and, at the axis, the symmetry condition $\dfrac{\partial u}{\partial \eta} = \dfrac{\partial T}{\partial \eta} = 0$. For Eqs. (3) and (4), we set $v = 0$ at the wall and on the axis.

The aim of the problem is to find the critical flow rate through the nozzle and to calculate subsonic gas outflow from the nozzle corresponding to this flow rate [2].

2. Computational algorithm. The set of Eqs. (1)–(4) is elliptic in the subsonic areas; therefore, it is impossible to construct a purely evolutionary method with respect to the longitudinal coordinate. Global iterations [3, 4] are needed. Then, it is necessary to fix evolutionary derivatives responsible for the upstream transfer of information opposite to the flow in the subsonic flow regions at each of these iterations. We show that such a derivative is $\dfrac{\partial \alpha}{\partial \xi}$, where $\alpha(\xi, \eta) = \dfrac{p(\xi, \eta)}{p_a(\xi)}$ is the function characterizing the transversal distribution of pressure.

Instead of the desired pressure, we introduce two functions $p_a(\xi)$ and $\alpha(\xi, \eta)$ into the set of Eqs. (1)–(4). Then, the equation for α follows from (3):

$$\frac{\gamma \alpha u}{T H_\xi}\frac{\partial v}{\partial \xi} = -\frac{1}{H_\eta}\frac{\partial \alpha}{\partial \eta} + (K_\xi v - K_\eta u)\frac{\gamma \alpha u}{T}. \qquad (5)$$

For the axial pressure, we have the trivial equation

$$\frac{\partial p_a}{\partial \eta} = 0. \qquad (6)$$

For function α, the relation $\alpha = 1$ is the boundary condition on the axis and, for p_a, this is one of the conditions for the transverse velocity (on the axis or at the wall). In Eq. (1), the gradient of pressure is replaced by the expression $\alpha\dfrac{\partial p_a}{\partial \xi} + \omega p_a \dfrac{\partial \alpha}{\partial \xi}$. It is easy to show, using the method of characteristics, that if we take function $\omega(\xi, \eta)$ in the form

$$\omega = \min\left\{1, \sigma\frac{\gamma \mathrm{M}_\xi^2}{1 + (\gamma - 1)\mathrm{M}_\xi^2}\right\}, \quad 0 < \sigma < 1, \qquad (7)$$

where $\mathrm{M}_\xi = u/\sqrt{T}$ is the local value of the Mach number determined by the longitudinal component of the velocity, the set of Eqs. (1), (2), (4)–(6) is of the hyperbolic type within the entire range of variation of the Mach number. The elliptic properties of the original set of equations written with respect to the variables u, v, T, α, and p_a in the subsonic areas of the flow are related to a part of the pressure gradient $(1 - \omega)p_a\dfrac{\partial \alpha}{\partial \xi}$ Eq. (1) for the longitudinal momentum.

The solution can be found by global iterations with respect to the longitudinal component of the gradient of the function α characterizing the degree of inhomogeneity of the transversal distribution of pressure. At a current global iteration, we integrate the regularized set of Eqs. (1), (2), (4)–(6) by the marching method [5]. The regularization corresponds to replacing the longitudinal gradient of pressure in Eq. (1) by the expression

$$\alpha\frac{\partial p_a}{\partial \xi} + p_a\left[\omega\frac{\partial \alpha}{\partial \xi} + (1 - \omega)\left(\frac{\partial \alpha}{\partial \xi}\right)^0\right], \qquad (8)$$

where $\left(\dfrac{\partial \alpha}{\partial \xi}\right)^0$ is the longitudinal gradient calculated at the previous global iteration. The upstream transfer of perturbations in the subsonic areas is taken into account by using a value of α downstream along the current marching layer in the process of the difference approx-

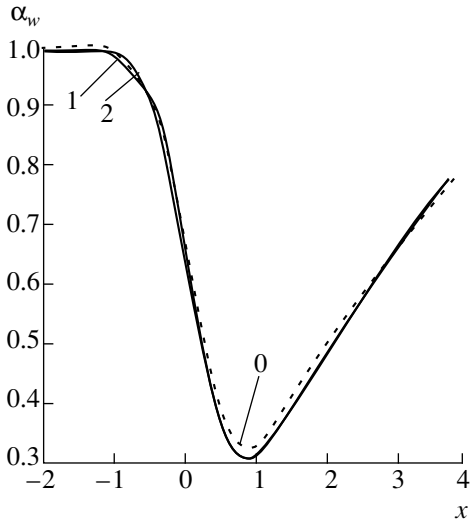

Fig. 1. Convergence of iterations for the distribution of α at the wall. Numbers of curves correspond to subsequent global iterations.

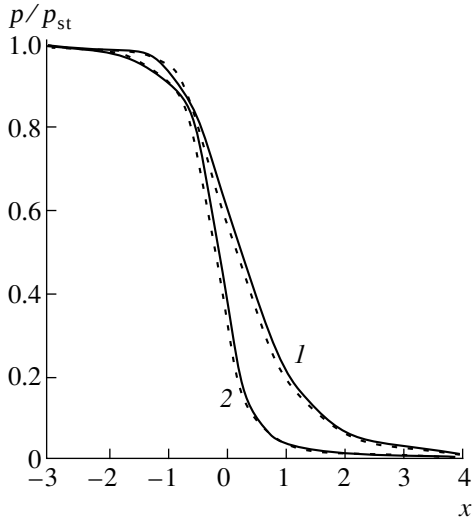

Fig. 2. Distributions of pressure (*1*) on the axis and (*2*) at the wall. Dashed and solid lines correspond to the zeroth and first iteration, respectively.

imation of the derivative $\left(\frac{\partial\alpha}{\partial\xi}\right)^0$ at this layer. In the outlet cross section, a soft boundary condition $\frac{\partial^2\alpha}{\partial\xi^2} = 0$ [6] is used in calculating $\left(\frac{\partial\alpha}{\partial\xi}\right)^0$. The safety factor σ in formula (7) is assumed to be equal to 0.97–0.99.

The distribution of α over the inlet cross section is determined from the condition that the longitudinal gradient α equal to $\left(\frac{\partial\alpha}{\partial\xi}\right)^0$ is given in this cross section.

At the initial (zeroth) iteration, the derivative $\left(\frac{\partial\alpha}{\partial\xi}\right)^0$ is assumed to be zero. Correspondingly, the longitudinal gradient of pressure in Eq. (1) was replaced by the expression

$$\frac{\partial p}{\partial\xi} = \alpha\frac{\partial p_a}{\partial\xi} + \omega p_a\frac{\partial\alpha}{\partial\xi}. \qquad (9)$$

The values of derivative $\left(\frac{\partial\alpha}{\partial\xi}\right)^0$ are used only in the subsonic flow regions where $1 - \omega \neq 0$; therefore, the initial iteration is a good approximation to the exact solution, if the following condition is met in subsonic regions:

$$\frac{\partial\ln\alpha}{\partial\xi} \ll \frac{\partial\ln p_a}{\partial\xi}. \qquad (10)$$

In turn, condition (10) of local similarity for transversal distributions of α is a good approximation for the flows in the channels with a small change in the longitudinal curvature of the wall. Thus, the hyperbolic model of viscous flows corresponds to approximation (9). This model is applicable for calculations of the flows in channels with moderate values of the wall curvature.

The finite-difference scheme [5] used for integrating is of the fourth order of accuracy with respect to coordinate η and of the second order with respect to ξ. In calculations, we take the nonuniform net becoming denser toward both the wall and the critical cross section of the nozzle.

3. Results. The efficiency of the method is demonstrated by the example of computations for the air flow with $\mathrm{Re}_r = 10^6$ in a conic nozzle with half-opening angles for narrowing and expanding cones equal to 30° and a throat curvature $K_w = 1.0$. The rate of convergence of global iterations over the field of the function α is illustrated in Fig. 1, where we show the distribution α_w of this function at the wall for the first three iterations. Abscissa $x = 0$ in the plots corresponds to a minimum nozzle cross section. It is clear that even zero iteration gives the solution close to the exact one in spite of the fact that α_w near the throat decreases by a factor of three.

In Fig. 2, we show the distributions of pressure at the axis and the wall for the first two iterations, the pressure being normalized to the stagnation pressure p_{st}. We may notice that the zero iteration also yields a good approximation for the pressure field. The convergence of the viscosity coefficient c_f at the wall is illustrated in Fig. 3. Even the first global iteration yields the distribution of c_f along the wall close to the exact one. In Fig. 4, we show the calculated (accurate to zeroth and first iterations) and measured [7] isolines of the

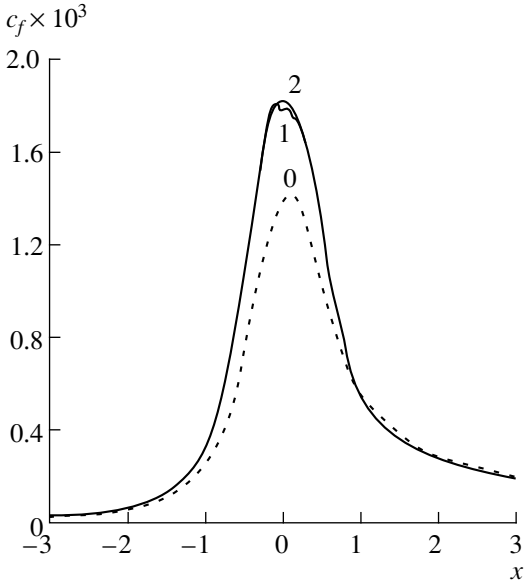

Fig. 3. Convergence of iterations for the distribution of the coefficient of friction at the wall. Numbers of curves correspond to subsequent global iterations.

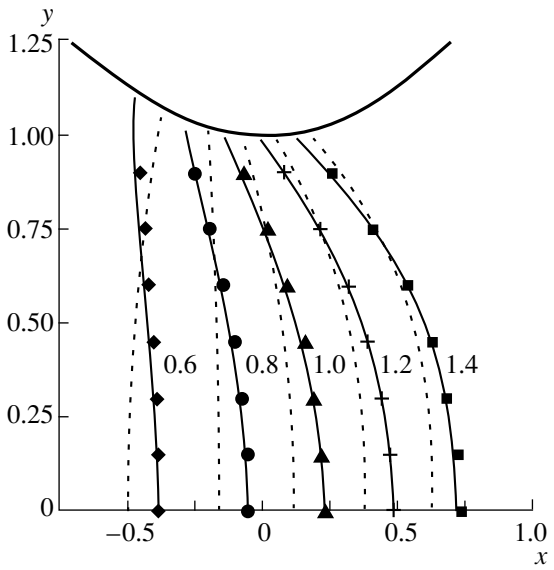

Fig. 4. Isolines of the Mach number. Dashed and solid lines correspond to zeroth and first iterations, respectively, dots are experimental data. The values of Mach number are indicated near the curves.

Mach number in the nonviscous region of the nozzle throat. Even the first iteration yields the solution for the velocity field close to the exact one.

Thus, for the model of viscous flow [1], we obtained an ultra-fast algorithm for computations of the entire flow field at moderate and high values of the Reynolds number and at arbitrary Mach numbers. A novel hyperbolic model is constructed, which reproduces the pressure field for an arbitrary streamline curvature. If we choose this model as the initial approximation, the algorithm converges in one iteration.

ACKNOWLEDGMENTS

This work was supported by the Russian Foundation for Basic Research, project no. 00-01-0151.

REFERENCES

1. N. N. Kalitkin, B. V. Rogov, and I. A. Sokolova, Dokl. Akad. Nauk **370**, 46 (2000) [Dokl. Phys. **45**, 33 (2000)].
2. U. G. Pirumov and G. S. Roslyakov, *Gas Flow in Nozzles* (Mos. Gos. Univ., Moscow, 1978).
3. D. A. Anderson, J. C. Tannehill, and R. H. Pletcher, *Computational Fluid Mechanics and Heat Transfer* (Hemisphere, New York, 1984; Mir, Moscow, 1990), Vol. 2.
4. V. L. Kovalev, A. A. Krupnov, and G. A. Tirskiĭ, Dokl. Akad. Nauk **338**, 333 (1994) [Phys. Dokl. **39**, 665 (1994)].
5. N. N. Kalitkin, B. V. Rogov, and I. A. Sokolova, Mat. Model. **11** (7), 95 (1990).
6. Yu. É. Egorov, M. Kh. Strelets, and M. L. Shur, Mat. Model. **2** (10), 3 (1990).
7. J. C. Dutton and A. L. Addy, AIAA J. **19**, 801 (1981).

Translated by V. Bukhanov

Doklady Physics, Vol. 45, No. 9, 2000, pp. 485–488. Translated from Doklady Akademii Nauk, Vol. 374, No. 2, 2000, pp. 194–197.

MECHANICS

Nonlinear Response of a Layer to Pulse Action in Diagnostics of Small Inhomogeneities

Corresponding member of the RAS O. V. Rudenko*, L. E. Sobisevich, A. L. Sobisevich**, and C. M. Hedberg*****

Received May 5, 2000

Nonlinear methods in acoustic diagnostics attract a particular interest owing to their potentialities in solving important applied problems [1, 2]. Giant nonlinear response, observed at acoustic irradiation of microscopic gas bubbles in liquids, cracks and fluid-filled pores in solids, and compressed contact of rough surfaces, is used in diagnostics of materials of industrial and geological structures [3–8]. For example, the magnitude of acoustic response of a bubble cluster in water corresponds to the nonlinearity parameter $\varepsilon \sim 10^3$, whereas for bubble-free water, this parameter is equal to 3.5, and for air, $\varepsilon = 1.2$. Among the applications of nonlinear methods to medical diagnostics, we outline the preparation of microbubble-based contrast agents of the Albunex type for the ultrasonic visualization of blood flow and development of distant elastometry methods to measure the shear elasticity of soft tissues [9, 10].

Generally speaking, reconstruction of characteristics of a scattering inhomogeneity requires an analysis of complicated inverse problems like those of computer tomography [11]. To succeed in solving them, we need direct data on the nonlinear reflection, transmission, and scattering of waves, but there is a lack of such data. This suggests generalizing solutions to classical linear problems by considering them in a nonlinear formulation.

The problem of the plane-wave incidence upon a layer is of particular interest. It is rather simple and could be solved analytically. In addition, it is closely related to the response of a shroud of bubbles floating up in water [4] or that of a rough planar contact [7]. Finally, the layer serves as a model for more complicated inhomogeneities; its response enables us to reconstruct the spectral composition and the field structure of other nonlinear scatterers.

We now consider the layer with plane boundaries located at $x = 0$ and $x = h$.

The medium within the layer is characterized by density ρ_0, velocity of the sound wave propagation c_0, and the nonlinearity parameter ε_0. The layer is surrounded by the medium with the corresponding parameters ρ_1, c_1, and ε_1. We assume that the impedance ratio and the wave thickness of the layer are small,

$$\zeta = \frac{\rho_0 c_0}{\rho_1 c_1} \ll 1, \quad \Delta = \frac{h}{2c_0 t_0} \ll 1. \tag{1}$$

Here, t_0 is the characteristic time, i.e., the inverse frequency of the pulse action. An exact solution to the linear problem [12] allows us to pass to limit (1); namely,

$$\left(\frac{d}{d\tau} + \frac{\zeta}{\Delta}\right)\begin{pmatrix} p_\pm \\ p_t \\ p_r \end{pmatrix} = \begin{pmatrix} \zeta/(2\Delta) \\ \zeta/\Delta \\ -d/d\tau \end{pmatrix} p_i(\tau), \tag{2}$$

which corresponds, for example, to a thin air layer in water or to a crack inside a solid. In (2), the following notation is accepted: $\tau = t/t_0$; p_i and p_t are the shapes of the pulse incident onto the layer (from the side of negative x onto the boundary $x = 0$) and for the pulse passed through the layer to the region of $x > h$, respectively; p_r is the shape of the reflected signal propagating towards the incident signal; and p_+ and p_- stand for two waves inside the layer propagating toward the positive and negative directions of the x-axis, respectively.

The profile of the transmitted signal can be expressed in terms of the incident signal by the relationship

$$p_t = \frac{\zeta}{\Delta}\int_{-\infty}^{\tau} p_i(\tau')\exp\left[-\frac{\zeta}{\Delta}(\tau - \tau')\right]d\tau'. \tag{3}$$

According to (2), the reflected signal is proportional (with the opposite sign) to the derivative of (3), or is

* *Department of Physics, Moscow State University, Vorob'evy gory, Moscow, 119899 Russia; e-mail: rudenko@uipe-ras.scgis.ru*

** *Schmidt Joint Institute of Physics of the Earth, Russian Academy of Sciences, ul. Bol'shaya Gruzinskaya 10, Moscow, 123810 Russia; e-mail: sobis@uipe-ras.scgis.ru, alex@uipe-ras.scgis.ru*

*** *Institutionen for Maskinteknik, 37179 Karlskrona, Sweden; e-mail: claes.hedberg@ima.hk-r.se*

1028-3358/00/4509-0485$20.00 © 2000 MAIK "Nauka/Interperiodica"

equal to the difference $p_r = p_t - p_i$. It can also be easily shown that profiles p_r and p_t are mutually orthogonal, the sum of energies transported by these waves is exactly equal to the energy of the incident pulse p_i. In addition, for a thin layer, the pressures in all three regions, $x < 0$, $0 < x < h$, and $x > h$, are mutually equal for any time moment: $p_i + p_r = p_+ + p_- = p_i$. Evidently, this equality remains valid for the nonlinear problem as well.

A similar approach with account taken of the nonlinear properties of the layer results in the following equation instead of (2):

$$\frac{d}{d\tau}f(p) + \frac{\zeta}{\Delta}p = \frac{\zeta}{\Delta}p_i(\tau). \tag{4}$$

Here, $p = p_+ + p_-$ is the internal field within the layer (its temporal variation reproduces the shape of the transmitted pulse). Expression

$$f(p) = c_0^2\rho = p - \frac{\varepsilon_0}{c_0^2\rho_0}p^2 + \frac{\chi_0}{(c_0^2\rho_0)^2}p^3 + \ldots \tag{5}$$

describes the pressure dependence of the density. The right-hand side of (5) is a power series expansion in terms of p, which is valid for a weakly nonlinear response; ε_0 and χ_0 are the quadratic- and cubic-nonlinearity coefficients, respectively. Note that, in many cases, the response cannot be treated as a weak one. Below, an example of the exact solution will be presented. Finally, under the necessity of taking into account the medium "memory" in the equation of state (5) (or in the analogous relation between tension and strain in solids), more general functional relations should be used instead of (5), e.g., the series of the Volterra–Frechet type.

In the case of the layer formed by the bubble shroud in water, the first terms in such a series can be easily calculated,

$$\rho = \int_0^\infty c^2(t_1)p(t-t_1)dt_1 - \iiint_0^\infty \varepsilon(t_1, t_2, t_3) \times p(t-t_1-t_2)p(t-t_1-t_3)dt_1dt_2dt_3, \tag{6}$$

where

$$c^2 = \frac{\rho_1 n\nu}{\omega_0}\sin(\omega_0 t_1),$$
$$\varepsilon = \frac{\rho_1 n g \nu^2}{\sqrt{\omega_0^2 - \delta^2}}e^{-\delta t_1}\sin(t_1\sqrt{\omega_0^2 - \delta^2})\sin(\omega_0 t_2)\sin(\omega_0 t_3), \tag{7}$$

and the following notation [13] is introduced:

$$\omega_0^2 = \frac{3c_0^2}{R_0^2}, \quad g = \frac{3\varepsilon_0}{4\pi R_0^3},$$
$$\nu = \frac{4\pi R_0^2}{\rho_0}, \quad \delta = \frac{1}{2}\nu\rho_1 c_1 nh. \tag{8}$$

Here, R_0 and n are the equilibrium radius of the bubbles and their number per unit volume, respectively; ω_0 is the resonance frequency of an individual bubble.

Usually, the Q factor $\omega_0/(2\delta)$ for oscillations in the layer is small, and the layer response can be described by (4), where factor ζ should be replaced by $\zeta/(\nu\Delta)$. In other words, the factor here differs from that in the previous case by the presence of the volume concentration $\nu = n(4\pi R_0^3/3)$ of the gas.

For the case of the contact between rough surfaces [6, 7], Eq. (4) takes the form

$$\frac{d}{dt}\left(p - \frac{\beta}{2K^2}p^2\right) - \frac{2K}{\rho_1 c_1}p = \frac{2K}{\rho_1 c_1}p_i, \tag{9}$$

where

$$K = E\int_{h_0}^\infty w(l)\frac{dl}{l}, \quad \beta = E\frac{w(h_0)}{h_0}. \tag{10}$$

Here, E is the Young modulus of the medium, $w(l)$ is the probability distribution for the heights of microscopic bumps on the rough surface, and $h_0(P)$ is the equilibrium thickness of the layer (in the absence of a probing signal), which depends on applied static pressure P.

Thus, the response of a given array of inhomogeneities obeys Eq. (4). Under approximation of weak quadratic nonlinearity, linear part $p^{(1)}$ of the response and nonlinear part $p^{(2)}$ can be calculated using a couple of equations following from (4):

$$\left(\frac{d}{d\tau} + \frac{\zeta}{\Delta}\right)\begin{pmatrix} p^{(1)} \\ p^{(2)} \end{pmatrix} = \begin{pmatrix} \frac{\zeta}{\Delta}p_i \\ \frac{\varepsilon_0}{c_0^2\rho_0}\frac{d}{d\tau}(p^{(1)})^2 \end{pmatrix}. \tag{11}$$

Note that the integral of $p^{(2)}$ should vanish.

In Fig. 1a, we show the linear $p^{(1)}$ (dashed curves) and the total (solid curves) response to the probing compression pulse (17). The curves were calculated for $\zeta/\Delta = 1$ at three values of parameter $b = 2\varepsilon_0 p_0/(c_0^2\rho_0)$: $b = 1.0$, 2.5, and 5.0.

In the case of the layer exposed to a periodic signal $p_i = p_0\sin(\omega t)$, under condition $\tau \gg \Delta/\zeta$, we obtained the

nonlinear response at a frequency of 2ω,

$$p^{(2)} = \frac{\varepsilon_0 p_0^2}{c_0^2 \rho_0} \frac{\Delta}{\zeta^2 + \Delta^2} \frac{1}{\sqrt{\zeta^2 + 4\Delta^2}} \cos(2\tau + 2\varphi_1 + \varphi_2), \quad \varphi_n = \arctan\left(\frac{\zeta}{n\Delta}\right). \tag{12}$$

The response attains its peak value $p_{\max}^{(2)}$ at $\zeta/\Delta \approx 2.2$ for $h \approx 0.14\lambda\zeta$. In the absence of inhomogeneities over the layer thickness h, the response at the second harmonic would have amplitude equal to $p_h^{(2)}$ [13]. The ratio of these amplitudes,

$$\frac{p_{\max}^{(2)}}{p_h^{(2)}} \approx 0.3 \frac{\varepsilon_0 p_0^2}{c_0^2 \rho_0} \frac{2c_1^3 \rho_1}{\varepsilon_1 p_0^2 \omega h} \approx \frac{2}{3} \frac{\varepsilon_0}{\varepsilon_1} \left(\frac{c_1^2 \rho_1}{c_0^2 \rho_0}\right)^2, \tag{13}$$

is determined, first of all, by the ratios of the densities of the media under study and of the sound velocities in them, but not by their nonlinearity ratio. For the air layer surrounded by water, estimate (13) yields the value of 5.4×10^7. In the case of a liquid layer involving air bubbles, the factor v should appear in expression (13). For the concentrations $v \sim 10^{-4}$, the ratio in (13) is on the order of several thousands. This result agrees well with the experimental data in [4].

We now consider a strong deformation of the layer using the nonpower dependence (5):

$$\frac{p}{p_*} = \exp\left[\frac{f(p)}{p_*}\right] - 1. \tag{14}$$

Model (14) provides a satisfactory description for the typical behavior of $\rho(p)$ for condensed media; namely, the slowing down of density increase with increasing pressure (induced by increased "rigidity" of the medium), a rapid decrease in the density under the applied stretching forces, and the existence of the limiting negative pressure $-p_*$.

The problem specified by (4) and (14) is solved exactly. For the unsteady (pulse) response, the solution has the form

$$\frac{p}{p_*} = \frac{\exp\left\{\frac{\zeta}{\Delta}\left(\tau + b\int_{-\infty}^{\tau} \varphi(x)dx\right)\right\}}{C + \int_{-\infty}^{\tau} \exp\left\{\frac{\zeta}{\Delta}\left(x + b\int_{-\infty}^{x} \varphi(x_1)dx_1\right)\right\}dx} - 1. \tag{15}$$

Here, C is the integration constant, $b = p_0/p_*$, and the shape of the probing pulse is given by the expression $p_i = p_0\varphi(t/t_0)$. The solution to (15) takes the simplest form

$$\frac{p}{p_*} = \frac{[(1+\tau^2)^{\pm b} e^{\tau}]^{\zeta/\Delta}}{1 + \frac{\zeta}{\Delta}\int_0^{\tau} [(1+x^2)^{\pm b} e^{x}]^{\zeta/\Delta} dx} - 1 \tag{16}$$

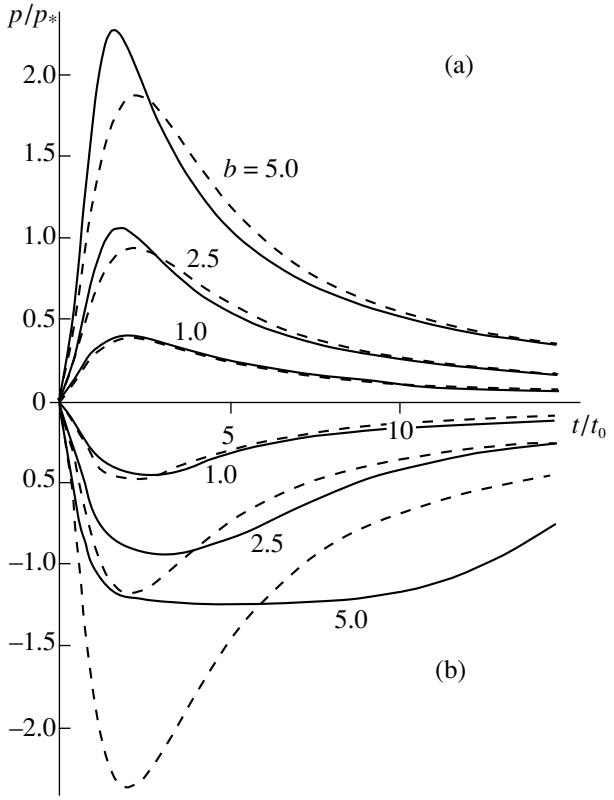

Fig. 1. Response of the layer exposed to the unit pulse of (a) compression and (b) decompression. Solid curves correspond to the total response, dashed lines correspond to the linear part $p^{(1)}$ of the response. The curves are calculated for $\zeta/\Delta = 1$ at three values of parameter b.

for the unipolar probing pulse

$$\varphi = \pm\frac{\tau}{1+\tau^2} H(\tau). \tag{17}$$

Here, H is Heaviside function and the signs "plus" and "minus" relate to the compression and decompression pulses, respectively. The shapes of the response for the layer exposed to the compression and decompression pulses are shown in Figs. 1a and 1b, respectively. The curves correspond to the values of parameters $\zeta/\Delta = 1$, $b = p_0/p_* = 1.0$, 2.5, and 5.0. We can see that increase in b results in the significant deviation of positive nonlinear response (solid curves) from the linear response, whereas the negative response (see Fig. 1b) becomes unrecognizably distorted. As we should expect, the negative pressure values are limited by $-p_*$.

In addition, it is very interesting to analyze the strongly nonlinear steady-state response to the harmonic signal, which can be considered to be a generalization of result (12). The corresponding exact solution to (4) and (14) has the form

$$\frac{p}{p_*} = \frac{\exp\left(-\frac{\zeta}{\Delta}\cos\tau\right)}{I_0\left(\frac{\zeta}{\Delta}b\right) + 2\sum_{n=1}^{\infty}(-1)^n I_n\left(\frac{\zeta}{\Delta}b\right)\frac{\zeta}{\sqrt{\zeta^2 + n^2\Delta^2}}\cos(n\tau - \varphi_1)} - 1, \quad (18)$$

where I_n are the modified Bessel functions, φ_1 was specified above (see (12)). The shape of response (18) is illustrated in Fig. 2a for $\zeta/\Delta = 1$ and $b = 1, 2, 5, 10$. It behaves as a periodic sequence of sharp compression peaks intermittent by smoothed decompressions not exceeding the limit $p = -p_*$. The spectrum presented in Fig. 2b for $b = 10$ consists of many multiple harmonics. The amplitudes of the second and the third harmonics are comparable to the response amplitude at the basic frequency of the probing signal. Similar behavior of profiles and spectra was observed in experiment [7].

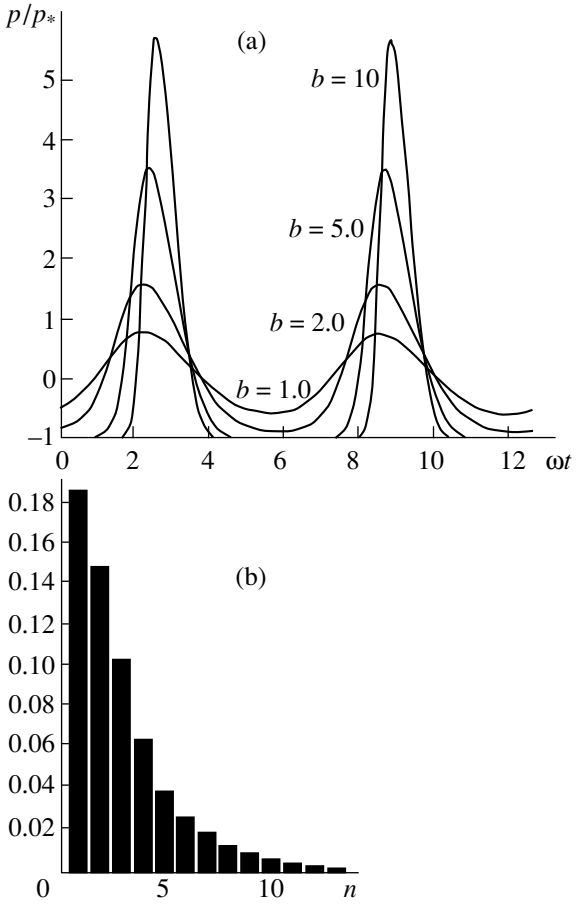

Fig. 2. (a) Shape of the steady-state response to the harmonic excitation for $\zeta/\Delta = 1$ at $b = 1, 2, 5, 10$. (b) Response spectrum for $b = 10$.

ACKNOWLEDGMENTS

This work was supported by the Russian Foundation for Basic Research, projects nos. 99-02-17198, 99-05-65599, etc., by INTAS and "Universities of Russia" programs, and by the Department of Mechanics of the Karskrona/Roneby University, Sweden.

REFERENCES

1. O. V. Rudenko, J. Nondestr. Test. **29**, 583 (1993).
2. R. A. Guyer and P. A. Johnson, Phys. Today, **52** (4), 30 (1999).
3. I. Shkolnik, L. Zarembo, and V. Krasilnikov, in *Frontiers of Nonlinear Acoustics* (Elsevier, London, 1990), pp. 589–594.
4. K. Naugolnykh and L. Ostrovsky, *Nonlinear Wave Processes in Acoustics* (Cambridge Univ. Press, Cambridge, 1988).
5. V. A. Robsman, Akust. Zh. **39**, 333 (1993) [Acoust. Phys. **39**, 176 (1993)].
6. O. V. Rudenko and A. V. Chin, Akust. Zh. **40**, 593 (1994) [Acoust. Phys. **40**, 593 (1994)].
7. I. Yu. Solodov, Ultrasonics **36**, 383 (1998).
8. A. M. Sutin and V. E. Nazarov, Izv. Vyssh. Uchebn. Zaved., Radiofiz. **38**, 435 (1995).
9. A. P. Sarvazyan, O. V. Rudenko, S. D. Swanson, *et al.*, Ultrasound Med. Biol. **24**, 1419 (1998).
10. O. V. Rudenko and A. P. Sarvazyan, Med. Biotekhnol., No. 3, 3 (2000).
11. V. A. Burov, I. E. Gurinovich, O. V. Rudenko, and E. Ya. Tagunov, Akust. Zh. **40**, 922 (1994) [Acoust. Phys. **40**, 816 (1994)].
12. L. M. Brekhovskikh, *Waves in Layered Media* (Nauka, Moscow, 1973; Academic, New York, 1980).
13. O. V. Rudenko and S. I. Soluyan, *Theoretical Foundations of Nonlinear Acoustics* (Nauka, Moscow, 1975; Plenum, New York, 1977).

Translated by O. Chernavskaya

Doklady Physics, Vol. 45, No. 9, 2000, pp. 489–492. Translated from Doklady Akademii Nauk, Vol. 374, No. 2, 2000, pp. 198–201.

MECHANICS

A Multistep Method for Acceleration of Bodies

Corresponding Member of the RAS V. M. Fomin, B. V. Postnikov, G. A. Sapozhnikov, and V. P. Fomichev

Received May 17, 2000

For enhancing the amplitude of shock waves, Zababakhin [1] proposed to employ a multilayer system of alternating bodies made of "light" and "heavy" materials with a thickness decreasing in the direction of the motion of the bow shock wave. Such a process is referred to as the unlimited cumulation effect. Laptev and Trishin [2] and Bolchan and Cowen [3] considered this effect in the multilayer obstacle with decreasing (increasing) acoustic stiffness. In 1978, the authors of the present paper, using mathematical simulation for solving the problem of high-speed expansion in a system of distributed coaxial cylindrical shells separated by layers of explosives, constructed another example of the unlimited cumulation effect, which was called the multistep method for acceleration of plates and shells [4]. As became apparent after a number of years [6], a similar scheme, referred to as the cascade scheme, had been proposed and considered by Zababakhin (1948) and Al'tshuler (1951) for shells converging to an axis of symmetry. The dominant mechanism for obtaining high velocities in the cascade scheme involves [6, 7] a pulsed interaction of plates (shells) with decreasing masses (the increase in their velocities follows from the law of the momentum conservation) and throwing the plates in cascades by explosion products produced within an overcompressed detonation regime. Nonetheless, employing the same mechanism, the authors of the present paper concentrated their attention mostly on the search for an efficient scheme to deliver the energy produced by an explosive from the peripheral regions of the explosive to a plate (shell) being thrown by the use of intercessory plates (shells). In the case of electrodynamic acceleration, the main emphasis was put on the active involvement of these plates (shells) in creating a high-performance plasma piston.

The efficiency of the explosive-energy delivery to a body (plate, shell) is known to be rather low for large values of the load parameter $\eta = m_{ex}/m_t \gg 5$, where m_{ex} and m_t are the masses of an explosive and a body being thrown, respectively. This is due to the fact that the energy almost does not arrive at the active part of a charge from regions of the explosive situated far from the bodies. For delivering this energy to a body being thrown, it was proposed to separate an explosive (according to a certain procedure) into a number of spatially distributed layers and to attach a plate-intermediary (stage) to each of them. In this way, it was possible to increase the efficiency of the energy transfer from peripheral regions of an explosive to a body being thrown. At this point, it is important to efficiently use the energy of the explosive stages. Namely, at the first stage (in the course of the explosive detonation near a free surface), the explosive-energy delivery to a plate being thrown is attained in the most efficient way for $\eta \approx 2.5$ [5], see Fig. 1a. At subsequent stages, the maximum efficiency can be found according to Fig. 1b (the estimate corresponds to the limiting case, i.e., a fixed wall). The calculations have shown that about 3–5% of the initial-explosive energy is left in each cascade after completion of the throwing process even for a reasonable trade-off in its parameters. The value of the gap between cascades was chosen in such a way as to pro-

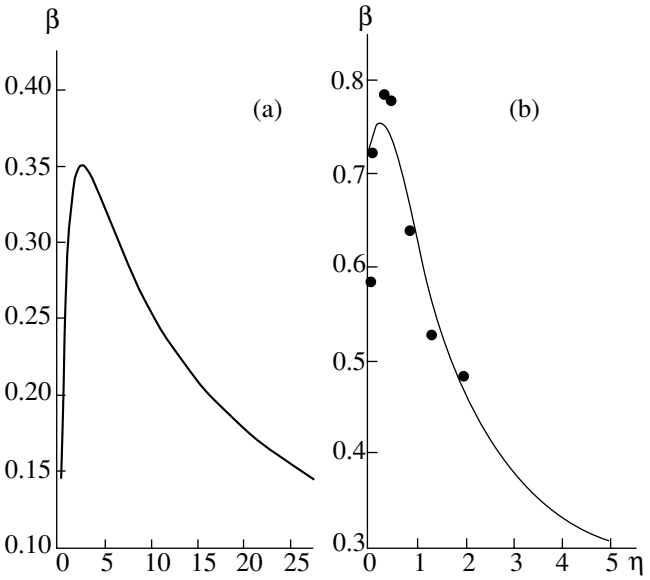

Fig. 1. Coefficient $\beta = E_t/E_{ex}$ of the explosive-energy transfer to the plate being thrown as a function of the loading coefficient: (a) initiation at a free boundary; (b) initiation at a rigid wall; points denote the data obtained by E.I. Bichenkov and V.A. Lobanov.

Institute of Theoretical and Applied Mechanics, Siberian Division, Russian Academy of Sciences, ul. Akademicheskaya 4/1, Novosibirsk, 630090 Russia

1028-3358/00/4509-0489$20.00

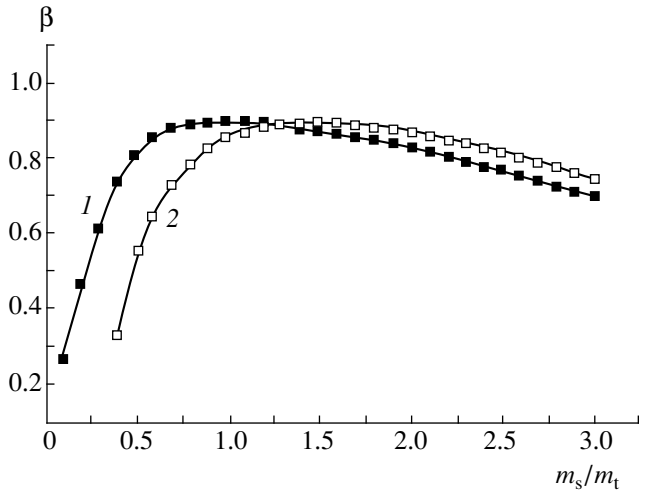

Fig. 2. The coefficient of the explosive-energy transfer to a body being thrown for (*1*) the Zababakhin scheme and (*2*) for the multistep scheme.

vide the maximum velocity in the plate acceleration process.

Two limiting interaction mechanisms for intercessory plates can be considered when the plates collide through the intermediate layer of the explosive: (1) The impact through "elastic" interlayer; in this case, if the explosive-layer mass is smaller by a factor of four than the mass of the thinner plate, then we have

$$V_t = \frac{2V_s k}{1 + m_t/m_s},$$

where V_t, V_s are the velocities of the plates being thrown and being struck with masses m_t and m_s, respectively; $k = 1$. (2) The bulk of the detonation-product power will be spent on plate throwing if the striker energy is higher than the explosive energy by a factor exceeding 2.5. In contrast to [8], in this case, coefficient k is not a constant. Based on numerical calculations for an inactive gas-dynamic interlayer with the adiabatic index γ and mass m_g, it was found that

$$k = 0.94 - \left(\frac{m_g}{m_g + m_s}\right)^{\gamma};$$

for the value of explosive mass m_{ex}, the following relationship can be used for a rapid estimate:

$$k = 0.94 - \left(\frac{m_{ex}}{m_{ex} + m_s}\right) + k_1\frac{E_{ex}}{E_{ex} + E_s}.$$

Here, $k_1 < 1$, $E_{ex}$is the total initial energy of an explosive, and E_s is the kinetic energy of a plate-striker.

The comparison between the results of calculations for a one-dimensional problem of collision of two plates of adjacent stages with either the intermediate gas layer (Zababakhin [1]) or an explosive of the same mass with equal initial energy consumption (in the case of an explosive, the striker energy is reduced by the corresponding amount) demonstrated that the maximum velocities of the body being thrown are the same for both the Zababakhin method and the multistep method for the parameters under consideration. However, in the case of the explosive, the plate-acceleration process evolves faster by an order of magnitude. Depending upon the aims of employing the methods, this fact can have either positive or negative implications. Figure 2 presents the energy-transfer coefficient as a function of ratio m_s/m_t for the Zababakhin method ($\beta = E_t/E_s$, where E_t is the kinetic energy of a plate being thrown) and the multistep method [$\beta = E_t/(E_{ex} + E_s)$].

In the outlined throwing scheme, the energy of the explosive layers is naturally released at the initial stage of the interaction of bodies for each stage, and it is not always possible to use this energy efficiently. The rail electrodynamic accelerator (railgun) is one of the efficient means for adding energy to a system during the throwing process.

From the late 1970s (see the pioneering paper [9]), obtaining hypervelocities (exceeding 10 km/s) by accelerating macroscopic bodies using a railgun in the plasma-piston regime has received much attention. Theoretical studies gave grounds for optimistic predictions; however, the throwing velocities actually attained for bodies with masses of 1–3 g did not exceed 6–7 km/s [10, 11]. The majority of investigators, one way or another, associate the limitation on the throwing velocity with the erosion paradigm, when the erosion of the channel-wall material brings about a variety of negative effects, among which are secondary breakdowns in the plasma-piston track, increase in the piston mass, turbulent flow, loss of stability, etc. [11–13].

We propose to employ the distributed laminated throwing schemes discussed above for the magnetoplasma acceleration of macrobodies by a railgun. The main part of such a system is of the "body–plasma–body" type. The distinctive feature of this system is the energy input into an intermediate plasma layer, which is distributed in time and actually controllable. Moreover, the "pinching" of a plasma piston between a striker and a body being thrown allows us to make the plasma piston compact in order to avoid, in part, the undesirable effects related to the electrode erosion and the loss of the plasma piston stability, to optimize the shock-wave mechanism of interaction for the system consisting of plasma and a body being thrown, and, eventually, to increase the throwing velocity.

This system was experimentally studied using a double-stage railgun plasma piston (the total length of the acceleration route is 0.7 m, the cross section is a square with a 10 mm side) having a capacitive power supply with 0.8 MJ of the total stored energy. Both stages (sections) are electrically decoupled; the capacitance of a capacitor battery for the first and second sections is 0.036 F and 0.0085 F, respectively; the operating voltage is 2.2 kV. The stages are separated by

a dielectric spacer 195 mm long made of caprolan; the active length of the copper electrodes of the second section is 230 mm. The striker is accelerated up to the velocity of 1.7 km/s at the first stage and interacts with a body being thrown through the plasma piston at the second section of the accelerator (Fig. 3c). The striker velocity is determined from discrete experiments with a shortened channel without the second section and, in addition, is controlled by magnetic sensors [14] (the base is 30 mm) located inside the channels at the exit of the first stage. The velocity of the body being thrown is determined by the conventional method employing loop targets (the base is 380 mm, the relative error in the velocity determination is no more than 1%) and is calculated for the channel cut by the formula $V_t = V\exp(\alpha x)$, where V is the velocity determined with loop targets; $\alpha = 0.11$ m^{-1} is the ballistic coefficient for a cubic body; and $x = 0.740$ m is the distance from the channel cut to the first loop target. The striker and the body being thrown are made of polycarbonate. The plasma piston is initiated by an explosion of a copper foil with mass 0.14 g. Comparative experiments were carried out on plasmadynamic acceleration of a body being thrown without wasting by a striker, with a start being performed from both a free boundary (Fig. 3a) and a rigid boundary (Fig. 3b). The current amplitude for the second section is 125 kA and is independent of the arrangement of the plasma piston rear boundary. The calculated instant for the beginning of the interaction between the striker and the plasma piston is chosen in the rising branch of the current for the second stage. The results of the experiment are summarized in the table (E is the energy stored in the capacitor battery). The energy-transfer coefficient is defined as $\beta_{tr} = E_t/E$ for the "plasma–body" scheme. Two limiting cases are possible for the "body–plasma–body" scheme: (1) the striker completely loses its energy as the result of the interaction, and then $\beta_{tr} = E_t/(E + E_s)$; (2) the velocities of bodies as they leave the second section are equal to $\beta_{tr} = \left(E_t + \frac{1}{2} m_s V_t^2\right)/(E + E_s)$. From the table, it follows that employing the distributed-acceleration scheme with the plasma piston "pinching" allows us to increase significantly the velocity of a body being thrown (by the factor 4 and by about 75%, as compared to the "plasma–body" case of, with a free rear boundary and with a rigid wall, respectively).

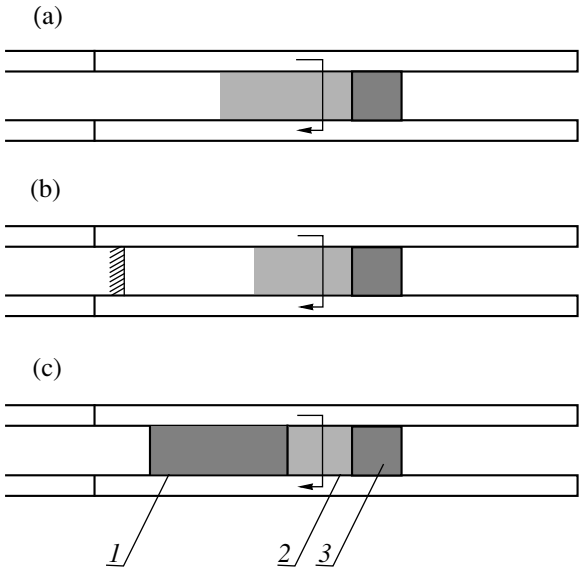

Fig. 3. The arrangement of the rear boundary of a plasma piston for the second section of the accelerator: (a) "plasma–body," free boundary; (b) "plasma–body," rigid boundary; (c) "body–plasma–body," movable boundary; (*1*) striker; (*2*) plasma piston (the arrow indicates the current direction); (*3*) the body being thrown.

The advantage of the acceleration scheme proposed is the possibility of cyclic accumulation of stages, and the first stage could be accomplished according to the gas-dynamic scheme of throwing. The process of acceleration of a body being thrown can be optimized by varying the striker velocity, its mass, the instant of the beginning of the interaction with the plasma piston, and the function of the power input. This gives the promise of exceeding the critical velocities (6–7 km/s) now attained by the railgun.

We may conclude that the implementation of intercessory plates (bodies) in the multistage throwing scheme provides an opportunity to enhance the active mass of an explosive. In the railgun, this allows us to improve the power performance of the plasma piston, including the formation of H pinched discharge, to eliminate the possibility of secondary breakdowns in the trace, and to enhance the throwing velocity through

Table

Striker			Plasma	Body being thrown			Rear boundary of the plasma piston	β_{tr}, %
m_s, g	V_s, km/s	E_s, kJ	E, kJ	m_t, g	V_t, km/s	E_t, kJ		
–	–	–	20.6	1.0	0.43	0.09	Free	0.45
–	–	–	20.6	1.0	1.0	0.50	Rigid	2.4
2.7	1.7	3.9	20.6	1.0	1.75	1.53	Movable	6.1–22.8

the transfer of kinetic energy stored by intercessory striking plates to the energetically active layer.

REFERENCES

1. E. I. Zababakhin, *Unlimited Cumulation Phenomena* in *Mechanics in the USSR for Passed 50 Years* (Nauka, Moscow, 1970), Vol. 2, pp. 313–342.
2. V. I. Laptev and Yu. A. Trishin, Prikl. Mekh. Tekh. Fiz., No. 6, 128 (1974).
3. Bolchan and Cowen, Rev. Sci. Instrum. **4** (8), 3 (1964).
4. V. M. Fomin, A. I. Gulidov, G. A. Sapozhnikov, *et al.*, *High-Velocity Interaction of Bodies* (Sib. Otd. Ross. Akad. Nauk, Novosibirsk, 1999).
5. F. A. Baum, L. P. Orlenko, K. P. Stanyukovich, *et al.*, *Physics of Explosion* (Nauka, Moscow, 1988).
6. L. V. Al'tshuler, R. F. Trunin, K. K. Krupnikov, and N. V. Panov, Usp. Fiz. Nauk **166**, 575 (1996) [Phys. Usp. **39**, 539 (1996)].
7. L. V. Al'tshuler, R. F. Trunin, V. D. Urlin, *et al.*, Usp. Fiz. Nauk **169**, 323 (1999).
8. A. G. Ivanov, E. Z. Novitskiĭ, V. A. Ogorodnikov, *et al.*, Prikl. Mekh. Tekh. Fiz., No. 2, 86 (1982).
9. S. C. Rashleigh and R. A. Marshall, J. Appl. Phys. **49**, 2540 (1978).
10. *Proceedings of the II All-Union Workshop on Dynamics of High-Current Arc Discharge in Magnetic Field* (Novosibirsk, 1992).
11. G. A. Shvetsov and V. M. Titov, in *Proceedings of the VII International Conference on Generation of Megagauss Fields and Related Experiments, Sarov, 1997*, Part 2, p. 866.
12. V. E. Ostashev, E. F. Lebedev, and V. E. Fortov, Teplofiz. Vys. Temp. **31**, 313 (1993).
13. A. V. Plekhanov, A. V. Kudryavtsev, V. B. Zheleznyĭ, and D. V. Khandryga, Prikl. Mekh. Tekh. Fiz. **37** (1), 15 (1996).
14. V. E. Podzin, G. A. Pozdnyakov, S. S. Pravdin, *et al.*, Teplofiz. Aéromekh. **2** (1), 89 (1995).

Translated by V. Tsarev

Doklady Physics, Vol. 45, No. 9, 2000, pp. 493–495. Translated from Doklady Akademii Nauk, Vol. 374, No. 3, 2000, pp. 330–332.

MECHANICS

Tearing off a Die Edge from the Surface of Elastic Basement

I. I. Argatov

Presented by Academician V.P. Myasnikov December 27, 1999

Received January 17, 2000

We analyze the problem of a single-sided contact of a circular die with a flat basement. The *a priori* unknown boundary of the contact area is assumed to be close to a circle. Based on asymptotic constructions, we derived a resulting problem for the function describing a contact-area variation. We also found the asymptotic solution to this problem.

1. It is well known [1] that the solution to the axially asymmetric contact problem concerning an inclined circular die with a plane basement exerting pressure without friction onto an elastic half-space was first found by V.M. Abramov [2]. For the contact pressure, the following expression was obtained:

$$p^0(x_1, x_2) = \frac{E}{\pi(1-\nu^2)}\frac{\delta_0 - 2\beta_2 x_1}{\sqrt{a^2 - x_1^2 - x_2^2}}. \qquad (1.1)$$

Here, E and ν are the Young modulus and the Poisson's ratio, a is the radius of the die basement, and δ_0 and β_2 are the translational displacement of the die and its angle of rotation about the Ox_2-axis. For $|\beta_2| > (2a)^{-1}\delta_0$, relationship (1.1) yields negative values and, thus, results in the necessity to introduce unilateral constraints in the calculation.

The structure of the solution to a contact problem for a significantly inclined die was investigated by V.L. Rvachev and V.S. Protsenko [3]. In monograph [4], the results of numerical calculations are presented. A related problem with a semi-known boundary of nearly circular contact area was studied by A.B. Kovura and V.I. Mossakovskiĭ [5] (see also review paper [6]).

In this paper, we construct an asymptotic solution to the problem for an inclined die using the method of S.A. Nazarov [7] and assuming that the contact is nearly circular. We derive a resulting problem allowing us to determine the boundary of contact area and present the asymptotic form of its solution.

2. Formulation of the problem. Let Γ be a circle in the plane $x_3 = 0$ of radius a with the center in the origin of coordinates. We consider the problem of a single-sided contact (see [8, 9], etc.) concerning a die with a disk-shaped flat foundation ω with the boundary Γ indented into the elastic half-space $x_3 > 0$. Using the Papkovich–Neĭber representation, we reduce the problem (see [10, 11]) to finding a harmonic function u vanishing at infinity and satisfying the boundary conditions

$$\partial_3 u(\mathbf{x}) = 0, \quad x_3 = 0, \quad (x_1, x_2) \notin \omega;$$
$$u(\mathbf{x}) \geq \delta_0 - \beta_2 x_1, \quad \partial_3 u(\mathbf{x}) \leq 0, \qquad (2.1)$$

$$[u(\mathbf{x}) - \delta_0 + \beta_2 x_1]\partial_3 u(\mathbf{x}) = 0,$$
$$x_3 = 0, \quad (x_1, x_2) \in \omega. \qquad (2.2)$$

The contact area ω_ε with boundary Γ_ε is determined by the condition that the contact pressures should be positive:

$$p(x_1, x_2) = -\alpha^{-1}\partial_3 u(x_1, x_2, 0),$$
$$\alpha \equiv 2(1-\nu^2)E^{-1}. \qquad (2.3)$$

We denote a small positive parameter as ε and put

$$\beta_2 = \beta_2^0 + \varepsilon\beta_2^1, \quad \beta_2^1 > 0; \quad \beta_2^0 = (2a)^{-1}\delta_0. \qquad (2.4)$$

In this case, contour Γ_ε is nearly circular and can be described by the equations

$$x_1 = (a - h_\varepsilon(\sigma))\cos\sigma,$$
$$x_2 = (a - h_\varepsilon(\sigma))\sin\sigma. \qquad (2.5)$$

Here, σ is the polar angle, and h_ε is the continuous function to be determined.

3. Asymptotic expansions near a sharp edge of the die. In the vicinity of Γ, we introduce local coordinates y_1, y_2, and σ related to the Cartesian coordinates by the formulas $x_1 = (a - y_1)\cos\sigma$ and $x_2 = (a - y_1)\sin\sigma$, and $x_3 = y_2$. In the planes normal to Γ, we introduce polar coordinates r and φ so that $y_1 = r\cos\varphi$ and $y_2 = r\sin\varphi$ with $\varphi \in [0, \pi]$.

Let v^0 be a solution to the limiting problem ($\varepsilon = 0$). It is known (see, e.g., [1, 7]) that the following

Admiral Makarov State Marine Academy,
Kosaya liniya 15A, St. Petersburg, 199026 Russia

1028-3358/00/4509-0493$20.00

representation is valid for function v^0:

$$v^0(\mathbf{x}) = \delta_0 - \beta_2^0 a\cos\sigma + \alpha(2\pi^{-1}r)^{1/2}\{K^0(\sigma) \times (1 - 4^{-1}\kappa r)\sin(\varphi/2) + 3^{-1}k^0(\sigma)r\sin(3\varphi/2)\} + \beta_2^0 y_1\cos\sigma + O(r^2), \quad r \longrightarrow 0, \tag{3.1}$$

where $K^0(\sigma)$ is the coefficient characterizing the intensity of compressing stresses and $\kappa = a^{-1}$ is the curvature of circle Γ. Correspondingly, for the density of contact pressures, we find, taking into account condition (2.3) as $r \longrightarrow 0$,

$$p^0(x_1, x_2) = -(2\pi r)^{-1/2}\{K^0(\sigma) + [k^0(\sigma) - 4^{-1}\kappa K^0(\sigma)]r\} + O(r^{3/2}). \tag{3.2}$$

Comparing (3.2) with the expansion of function (1.1), we obtain

$$K^0(\sigma) = -2\alpha^{-1}(\pi a)^{-1/2}(\delta_0 - 2\beta_2^0 a\cos\sigma),$$
$$k^0(\sigma) = -\alpha^{-1}(\pi a)^{-1/2}(a^{-1}\delta_0 + 2\beta_2^0\cos\sigma). \tag{3.3}$$

4. Asymptotic behavior of the stress-intensity coefficient. We denote the solution to the mixed problem as v^ε when (2.2) is replaced by the boundary condition

$$v^\varepsilon(x_1, x_2, 0) = \delta_0 - \beta_2 x_1, \quad (x_1, x_2) \in \omega_\varepsilon.$$

In papers [12, 13, 7], the principal terms of the asymptotic behavior for the stress-intensity coefficient correspond to v^ε at the Γ_ε edge. According to [7], we have

$$K^\varepsilon(\sigma) \sim K^0(\sigma) + \varepsilon K^1(\sigma) + B(K^0 h_\varepsilon; \sigma) + h_\varepsilon(\sigma)[b(\sigma) + 2^{-1}k^0(\sigma) + 4^{-1}K^0(\sigma)\kappa]. \tag{4.1}$$

Here,

$$K^1(\sigma) = 4\alpha^{-1}(\pi a)^{-1/2}\beta_2^1 a\cos\sigma \tag{4.2}$$

and B is the singular integral operator acting in accordance with the formula

$$B(H; \sigma) = \text{v.p.}\int_\Gamma [H(\tau) - H(\sigma)]Z(\tau, \sigma)ds_\tau. \tag{4.3}$$

In the case under study, $b(\sigma) \equiv 0$, $ds_\tau = ad\tau$, and the kernel of operator (4.3) has the form [13]:

$$Z(\tau, \sigma) = (2\pi)^{-1}(2a|\sin[(\tau - \sigma)/2]|)^{-2}. \tag{4.4}$$

5. Resulting problem for determining the contact-area boundary. We require that the contact pressures vanish at the disturbed section of boundary Γ_ε [see (2.2)]. This requirement implies the absence of singularities at points of Γ_ε lying inside ω:

$$h_\varepsilon(\sigma) > 0 \Rightarrow K^\varepsilon(\sigma) = 0. \tag{5.1}$$

The tensile stresses are prohibited by the relationship

$$h_\varepsilon(\sigma) = 0 \Rightarrow K^\varepsilon(\sigma) \le 0. \tag{5.2}$$

Finally, we must add the following condition to (5.1) and (5.2) since the contact area can only decrease:

$$h_\varepsilon(\sigma) \ge 0. \tag{5.3}$$

Substituting the asymptotic expression for $K^\varepsilon(\sigma)$, which was taken from (4.1) to (5.1) and (5.2) and taking into account (4.2) and (4.4), we obtain the following implications:

$$h_\varepsilon(\sigma) > 0 \Rightarrow \frac{\delta_0}{2a}h_\varepsilon(\sigma) + B(m^0 h_\varepsilon; \sigma) = \varepsilon m^1(\sigma) - m^0(\sigma); \tag{5.4}$$

$$h_\varepsilon(\sigma) = 0 \Rightarrow \frac{1}{2\pi a}\,\text{v.p.}\int_{-\pi}^{\pi}\frac{m^0(\tau)h_\varepsilon(\tau)}{4\sin^2[(\tau - \sigma)/2]}d\tau \ge \varepsilon m^1(\sigma) - m^0(\sigma). \tag{5.5}$$

Here, we have according to (3.3) and (4.2) that $m^0(\sigma) = \delta_0(1 - \cos\sigma)$ and $m^1(\sigma) = 2\beta_2^1 a\cos\sigma$.

Relationships (5.3)–(5.5) form the problem allowing us to determine function h_ε.

6. Asymptotic solution to the resulting problem. It is easy to see that in the case of a negative right-hand side of inequality (5.5), the necessary condition for $h_\varepsilon(\sigma) = 0$ is met. Neglecting the second term in (5.4), we find the first approximation

$$h_\varepsilon(\sigma) = a((\sigma_\varepsilon^0)^2 - \sigma^2), \quad |\sigma| \le \sigma_\varepsilon^0; \tag{6.1}$$

$$\sigma_\varepsilon^0 = \varepsilon^{1/2}\sqrt{2\beta_2^1/\beta_2^0}. \tag{6.2}$$

Thus, the tearing off occurs along the arc of length $2a(\sigma_\varepsilon^0 + O(\varepsilon))$. This fact agrees with the results of [14], where the parameter determining the gradient displacement of the contact boundary is found from the solution to a one-dimensional extremal problem. From (6.1), it immediately follows that the penetration depth for the front (free of stresses) surface of the elastic basement under the die obeys the following relationship at small values of parameter ε: $h_\varepsilon(0) = a(\sigma_\varepsilon^0)^2 + O(\varepsilon^{3/2})$.

7. The asymptotic behavior of the contact pressure can be easily obtained using the results from [7]. Note only that, in the neighborhood of a disturbed portion of boundary Γ_ε, the boundary-layer phenomenon arises. Problems similar to (5.3)–(5.5) were previously reported in [7, 15]; their solvability was investigated by reducing to the corresponding variational inequality. The application of the method reported in [7] to the

problem of tearing off a noncircular (for example, elliptic) die implies the necessity of having an explicit representation for the kernel of operator B. However, this information is unnecessary in obtaining results similar to (6.1) and (6.2).

ACKNOWLEDGMENTS

This work was supported by the Russian Foundation for Basic Research, project no. 98-01-00974.

The author is grateful to N.F. Morozov and S.A. Nazarov for their attention to this work and useful discussions.

REFERENCES

1. *Development of Contact Problem Theory in the USSR*, Ed. by L. A. Galin (Nauka, Moscow, 1976).
2. V. M. Abramov, Dokl. Akad. Nauk SSSR **23**, 759 (1939).
3. V. L. Rvachev and V. S. Protsenko, Dopov. Akad. Nauk Ukr. RSR, Ser. A: Fiz.-Tekh. Mat. Nauki, No. 11, 1023 (1970).
4. V. L. Rvachev and V. S. Protsenko, *Contact Problems of Elasticity Theory for Non-Classical Domains* (Naukova Dumka, Kiev, 1977).
5. A. B. Kovura and V. I. Mossakovskiĭ, Prikl. Mat. Mekh. **43**, 106 (1979).
6. V. I. Mossakovskiĭ and A. B. Kovura, Din. Prochn. Tyazh. Mash., No. 5, 74 (1980).
7. S. A. Nazarov, Izv. Akad. Nauk SSSR, Mekh. Tverd. Tela, No. 2, 152 (1989).
8. G. Fichera, *Existence Theorems in Elasticity. Boundary Value Problems of Elasticity with Unilateral Constraints* (Springer, Heidelberg, 1972; Mir, Moscow, 1974).
9. G. Duveau and J.-L. Lions, *Inequalities in Physics and Mechanics* (Nauka, Moscow,1980).
10. A. I. Lur'e, *Spatial Problems of Elasticity Theory* (Gostekhteorizdat, Moscow, 1955).
11. L. A. Galin, *Contact Problems of Elasticity Theory* (Gostekhizdat, Moscow, 1953).
12. I. S. Zakharevich, Prikl. Mat. Mekh. **49**, 961 (1985).
13. H. Gao and J. R. Rice, J. Appl. Mech. **54**, 627 (1987).
14. V. I. Kerchman, Izv. Akad. Nauk SSSR, Mekh. Tverd. Tela, No. 3, 66 (1988).
15. L. G. Kolton and S. A. Nazarov, Izv. Akad. Nauk SSSR, Mekh. Tverd. Tela, No. 3, 125 (1997).

Translated by V. Bukhanov

Doklady Physics, Vol. 45, No. 9, 2000, pp. 496–498. Translated from Doklady Akademii Nauk, Vol. 374, No. 3, 2000, pp. 333–335.

MECHANICS

Modeling of Boundary Conditions for Pressure and Total Head in Hydrodynamic Problems Using the Method of Fictitious Domains

Sh. S. Smagulov, N. M. Temirbekov, and N. T. Danaev

Presented by Academician A.A. Samarskiĭ December 1, 1999

Received December 28, 1999

A steady-state motion of a viscous incompressible fluid in a bounded domain $\Omega \subset R^2$ with the boundary S is reduced to the solution to a set of nonlinear partial differential equations [1]:

$$(v \cdot \nabla)v = \mu \Delta v - \nabla p + f, \quad \operatorname{div} v = 0, \tag{1}$$

$$v|_S = 0, \tag{2}$$

where v, p, and f are the fields of velocities, pressure, and mass forces, respectively; and μ is the viscosity (a positive constant). In problem (1), (2), no boundary conditions for pressure are present in the physical formulation. In turn, this fact hampers obtaining the numerical solution to the equation for a viscous incompressible fluid. The numerical solution to problem (1), (2) in the natural variables was studied in [2, 3], wherein the boundary conditions for pressure were approximately specified. Finding numerical values of pressure is reduced to solving the Poisson equation with the Neumann boundary conditions in which unknown velocity values are involved. As a result, it is difficult to analyze the stability of the proposed numerical algorithm and the correctness of solving a difference scheme. On the other hand, it is difficult to find the numerical solutions to problem (1), (2) in an arbitrary domain Ω with curvilinear boundaries S using the difference schemes proposed in [2, 3].

One of the methods for finding the numerical solution to problem (1), (2) in an arbitrary domain is the well-known method of fictitious domains [4, 5].

In this paper, we consider one of the versions of the fictitious-domain method for problem (1), (2). The essence of the method is the following. We set zero boundary conditions for the tangential component of the velocity vector and pressure at the boundaries of auxiliary domains. The latter condition makes it possible to reduce the problem of finding the pressure to the solution to the Dirichlet problem for the Poisson equation, which can be solved by an efficient numerical method [4, 6].

1. Modeling the boundary conditions for pressure. Let domain D envelope totally domain Ω, $\Omega \subset D$, $S \cap S_1 = \emptyset$, $D_1 = D/\Omega$, where S_1 is the boundary of domain D. In this case, we consider an auxiliary problem in D with a small parameter:

$$(v^\varepsilon \cdot \nabla)v^\varepsilon = \mu \Delta v^\varepsilon - \nabla p^\varepsilon + f - \frac{\xi(x)}{\varepsilon} v^\varepsilon, \quad \operatorname{div} v^\varepsilon = 0 \tag{3}$$

with the boundary conditions

$$v^\varepsilon \cdot \tau|_{S_1} = 0, \quad p^\varepsilon\big|_{S_1} = 0, \tag{4}$$

where τ is the tangent vector to boundary S_1,

$$\xi(x) = \begin{cases} 0 \text{ in } \Omega \\ 1 \text{ in } D_1 = D/\Omega. \end{cases}$$

Actually, domain D is assumed to be a rectangle in planar problems and a rectangular parallelepiped in spatial problems.

We introduce a set of infinitely differentiable vector functions $v(x)$ solenoidal in D and with zero tangential components at S_1:

$$m(D) = \{ v(x) \mid v(x) \in C^\infty(D), \operatorname{div} v = 0, v(x) \cdot \tau|_{S_1} = 0 \}.$$

We denote the spaces obtained by closing $m(D)$ in norms $L_2(D)$ and $W_2^1(D)$ as V and V_1 and their conjugate spaces as V^* and V_1^*, V and V^* are assumed being identical.

Al-Farabi State University of Kazakhstan, ul. Vinogradova 95, Almaty, 480012 Kazakhstan

1028-3358/00/4509-0496$20.00

Definition 1. The generalized solution to problem (3), (4) is the vector function $v(x) \in V_1$, which satisfies the integral identity

$$\mu(\nabla v^\varepsilon, \nabla\Phi)_D + \frac{1}{\varepsilon}(v^\varepsilon, \Phi)_{D_1} + ((v^\varepsilon \cdot \nabla)\Phi, v^\varepsilon)_D + \mu\int_{S_1} K(x)(v^\varepsilon, \Phi)dS_1 + \int_{S_1} (v^\varepsilon)^2 (v^\varepsilon \cdot n)\Phi dS_1 = (f, \Phi)_D \quad (5)$$

for each vector function $\Phi \in V_1$, where

$$(u, v)_D = \int_D uv\,dx,$$

$K(x)$ is the doubled curvature of the boundary S_1 and n is the external normal to the boundary S_1. The function f is continued by zero outside Ω. We assume that $K(x)$ is a nonnegative function.

Theorem 1. *Let domain $D \in R^3$, boundaries S and S_1 be smooth, and $K(x) \geq 0$. In this case, at least one generalized solution to problem* (3), (4) *exists and the following estimate takes place for this solution*:

$$\int_{S_1} K(x)|v^\varepsilon|^2 dS + \|v^\varepsilon\|_{V_1} + \frac{1}{\sqrt{\varepsilon}}\|v^\varepsilon\|_{L_2(D_1)} \leq C\|f\|_{V_1^*} \quad (6)$$

in the case of a reasonably small $\varepsilon > 0$.

Theorem 1 is proved by the Galerkin method. We seek an approximate solution to problem (3), (4) in the form

$$v_N^\varepsilon(x) = \sum_{j=1}^{N} \xi_j \omega_j,$$

where ω_j is the orthonormal basis of space V_1 and constants ξ_j can be found from the set of nonlinear algebraic equations

$$\mu(\nabla v_N^\varepsilon, \nabla\omega_j)_D + \frac{1}{\varepsilon}(v_N^\varepsilon, \omega_j)D_1 + ((v_N^\varepsilon\nabla)v_N^\varepsilon, \omega_j)_D + \mu\int_{S_1} K(x)(v_N^\varepsilon, \omega_j)dS_1 = (f, \omega_j)_D, \quad j = 1, 2, \ldots, N. \quad (7)$$

To prove the existence of a solution to nonlinear algebraic equations, we use the Braner lemma [7].

Theorem 2. *Let all the conditions of Theorem* 1 *be met. In this case, the generalized solution to problem* (3), (4) *converges to the generalized solution to problem* (1), (2) *as* $\varepsilon \longrightarrow 0$.

By virtue of relationship (7), we can select from sequence $\{v^\varepsilon\}$ the subsequences, for which we have:

$v^\varepsilon \longrightarrow v$ weakly in $W_2^1(\Omega)$,

$v^\varepsilon \longrightarrow v$ strongly in $L_4(\Omega)$,

$v^\varepsilon \longrightarrow v$ strongly in $L_2(S_1)$.

It is easy to see that v is the generalized solution to problem (1), (2).

Note. If $f \in L_2(\Omega)$ is reasonably small, it is possible to estimate the rate of convergence of the solution for $\varepsilon \longrightarrow 0$, namely, to obtain the estimate

$$\|v^\varepsilon - v\|_{W_2^1(\Omega)} \leq C\varepsilon^{3/4}.$$

In order to remove the condition of a reasonable smallness of ε, we propose a modified version of the fictitious domain method. For this purpose, we assume that the solution v to problem (1), (2) is bounded within domain Ω by a certain constant $M = \max_{\bar{\Omega}}|v|$. We construct the cutting function $\eta_M(u)$ continuously differentiable and vanishing outside the neighborhood $(-M-1, M+1)$:

$$\eta_M(u) = \begin{cases} u, & |u| \leq M \\ 0, & |u| \geq M+1. \end{cases} \quad (8)$$

We consider the following auxiliary problem:

$$((\boldsymbol{\eta}_M(v^\varepsilon)\cdot\nabla)v^\varepsilon) = \mu\Delta v^\varepsilon - \nabla p^\varepsilon - \frac{\xi(x)}{\varepsilon}v^\varepsilon + f, \quad (9)$$

$$\operatorname{div} v^\varepsilon = 0,$$

$$v^\varepsilon \cdot \tau|_{S_1} = 0, \quad p^\varepsilon|_{S_1} = 0, \quad (10)$$

where $\boldsymbol{\eta}_M(v^\varepsilon) = (\eta_M(v_1^\varepsilon), \eta_M(v_2^\varepsilon), \eta_M(v_3^\varepsilon))$.

It turns out that there exists the generalized solution to problem (3), (4) for an arbitrary $\varepsilon > 0$, and as $\varepsilon \longrightarrow 0$ these generalized solutions converge to the generalized solution to problem (1), (2).

2. Modeling boundary conditions for the total head. We rewrite equation (1) in the form

$$\operatorname{rot} v \times v = \mu\Delta v - \nabla Q + f,$$

$$\operatorname{div} v = 0, \quad Q = p + \frac{|v|^2}{2}, \quad (11)$$

$$v|_S = 0, \quad (12)$$

where Q is the total head.

For problem (11), (12), we consider the following version of the fictitious-domain method:

$$\operatorname{rot} v^\varepsilon \times v^\varepsilon = \mu\Delta v^\varepsilon - \nabla Q^\varepsilon - \frac{\xi(x)}{\varepsilon}v^\varepsilon + f, \quad (13)$$

$$\operatorname{div} v^\varepsilon = 0,$$

$$v^\varepsilon \cdot \tau|_{S_1} = 0, \quad Q|_{S_1} = 0. \quad (14)$$

The following theorem holds:

Theorem 3. *Let $K(x) \geq 0$, $f \in V_1^*(D)$, and S and S_1 be continuous. In this case, at least one generalized*

solution to problem (13), (14) *exists and the following estimate holds true for it*:

$$\int_{S_1} K(x)\left|v^\varepsilon\right|^2 dS + \left\|v^\varepsilon\right\|_{V_1(D)} + \frac{1}{\varepsilon}\int_{D_1}\left|v^\varepsilon\right|^2 dx \le C\|f\|^2_{V_1^*(D)} \quad (15)$$

for an arbitrary $\varepsilon > 0$. *The generalized solutions to problem* (13), (14) *are reduced to the generalized solution to problem* (1), (2) *as* $\varepsilon \longrightarrow 0$. *Furthermore, the following estimate is valid for a sufficiently small value of* $\|f\|_{L_2(\Omega)}$:

$$\left\|v^\varepsilon - v\right\|^2_{W_2^1(\Omega)} \le C\varepsilon^{3/4},$$

where C is the positive constant independent of ε.

3. Modeling boundary conditions for pressure and total head in the case of the unsteady Navier–Stokes equations. The problem on a unsteady motion of a viscous incompressible fluid is reduced to solving the set of differential equations

$$\frac{\partial v}{\partial t} + (v\cdot\nabla)v = \mu\Delta v - \nabla p + f, \quad (16)$$

$$\operatorname{div} v = 0,$$

$$v|_S = 0, \quad v|_{t=0} = 0. \quad (17)$$

Problem (16), (17) is solved by the fictitious-domain method:

$$\frac{\partial v^\varepsilon}{\partial t} + (v^\varepsilon\cdot\nabla)v^\varepsilon = \mu\Delta v^\varepsilon - \nabla p^\varepsilon - \frac{\xi(x)}{\varepsilon}v^\varepsilon + f, \quad (18)$$

$$\operatorname{div} v^\varepsilon = 0,$$

$$v^\varepsilon\big|_{t=0} = 0,\ v^\varepsilon\cdot\tau|_{S_1} = 0,$$

$$p^\varepsilon\big|_{S_1} = 0,\ t\in[0,T]. \quad (19)$$

Definition 2. The generalized solution to problem (18), (19) is function v^ε, $v_t^\varepsilon \in L_2(0, T; V(D))$, $v^\varepsilon \in L_2(0, T; V_1(D))$, satisfying the integral identity

$$\int_0^T [(v^\varepsilon, \Phi_t)_D + ((v^\varepsilon\cdot\nabla)\Phi, v^\varepsilon)_D]dt$$

$$+ \int_{S_1} K(x)(v^\varepsilon\Phi)ds + \mu\int_0^T(\nabla v^\varepsilon\nabla\Phi)_D dt$$

$$-\int_{S_1}(v^\varepsilon\bar{n})(v^\varepsilon\Phi)ds + \int_0^T(f,\Phi)_D dt = 0$$

for arbitrary $\Phi_t \in L(0, T; V_1(D))$, $\Phi \in L_2(0, T; V(D))$, $\Phi(T) = 0$.

Theorem 4. *Let* $f \in L_1(0, T; L_2(D))$, $f_t \in L_1(0, T; L_2(D))$, $K(x) \ge 0$, *and* $D \subset R^2$. *In this case, a unique generalized solution to problem* (18), (19) *exists and the following estimates hold true*:

$$\left\|v^\varepsilon(t)\right\|_{L_\infty(0,T;V(D))} + \left\|v^\varepsilon\right\|^2_{L_2(0,T;V_1(D))}$$

$$+\frac{1}{\varepsilon}\left\|v^\varepsilon\right\|^2_{L_2(0,T;L_2(D_1))} \le C < \infty,$$

$$\left\|v^\varepsilon\right\|_{L_\infty(0,T;V_1(D))} + \frac{1}{\varepsilon}\left\|v_t^\varepsilon\right\|_{L_2(0,T;L_2(D_1))}$$

$$+\left\|v_{tx}^\varepsilon\right\|_{L_2(0,T;L_2(D))} \le C < \infty.$$

Furthermore, as $\varepsilon \longrightarrow 0$, *the solution to problem* (18), (19) *converges to the solution to problem* (16), (17) *with the rate*

$$\left\|v^\varepsilon - v\right\|^2_{L_\infty(0,T;L_2(\Omega))} + \left\|v^\varepsilon - v\right\|^2_{L_2(0,T;W_2^1(\Omega))} \le C\varepsilon^{1/4}.$$

Note. In the case $\Omega \subset R^3$, Theorem 4 is valid in the small with respect to time.

4. Numerical implementation. To illustrate the efficiency of the proposed method, we considered the three-dimensional problem of the fluid flow in a pipe with curvilinear boundaries. The grid equations are numerically solved using the splitting scheme according to the physical processes [2]. To determine the pressure, the elliptic equation with the Dirichlet boundary conditions is solved by the method of alternating triangles. Numerical calculations were performed in parallelepiped $D = \{0 \le x \le 0.5, 0 \le y \le 1.5, 0 \le z \le 0.5\}$, which involves the initial domain with the curvilinear boundaries. Domain D was covered by the $(11 \times 21 \times 11)$ and $(21 \times 31 \times 21)$ grids. We obtained the numerical results in a wide range of the Reynolds numbers.

REFERENCES

1. O. A. Ladyzhenskaya, *Mathematical Problems in Dynamics of Viscous Incompressible Fluid* (Nauka, Moscow, 1970).
2. O. M. Belotserkovskiĭ, *Numerical Simulations in Mechanics of Continuous Media* (Nauka, Moscow, 1984).
3. A. Chorin, J. Comput. Phys. **2**, 12 (1967).
4. P. N. Vabishchevich, *Method of Fictitious Domains for a Problem of Mathematical Physics* (Mosk. Gos. Univ., Moscow, 1991).
5. A. N. Bugrov and Sh. S. Smagulov, in *Mathematical Models of Fluid Flow* (Novosibirsk, 1978), pp. 79–89.
6. A. A. Samarskiĭ, *The Theory of Difference Schemes* (Nauka, Moscow, 1977).
7. J.-L. Lions, *Quelques méthodes de résolution des problèmes aux limites nonlinéares* (Dunod, Paris, 1969; Mir, Moscow, 1972).

Translated by V. Bukhanov

Doklady Physics, Vol. 45, No. 9, 2000, pp. 499–502. Translated from Doklady Akademii Nauk, Vol. 374, No. 3, 2000, pp. 336–339.

MECHANICS

Incorrectness of the Chapman–Enskog Method

I. A. Sokolova

Presented by Academician A. A. Samarskiĭ November 21, 1999

Received December 24, 1999

The Chapman–Enskog method of successive iterations with the use of expanding perturbation functions in terms of Sonin polynomials is widely applied in the calculations of flows in viscous heat-conducting gases and in the studies of transport properties.

To the first approximation in a small parameter of the Chapman–Enskog method, the Navier–Stokes gasdynamic equations can be derived by solving the linearized Boltzmann equation. Explicit expressions for molecular flows (including relevant coefficients) are obtained by solving the integro-differential equations using variational methods combined with the series expansion of the distribution function perturbations in terms of the Sonin polynomials [1]. For them, an infinite system of algebraic equations have been derived, its order being specified by the number of the Sonin polynomials ξ kept in the expansion.

In the present paper, we study matrices of the system of algebraic equations, which we use to express the molecular transport coefficients. For actual gas mixtures, we show that determinants of these matrices can vanish in the case of long-range interparticle interactions and under the relevant behavior of the collision integrals and their derivatives. The matrix in the denominator turns out to be singular; hence, the system of algebraic equations has no solutions. This singularity was originally revealed in the course of computer simulations with very small steps of the temperature grid and was verified later by theoretical analysis. The singularity actually manifests itself in an interesting range of parameters characteristic of partially ionized mixtures.

Molecular flows and transport coefficients. The expression for the heat flux resolved with respect to thermodiffusion forces can be written as [2]

$$\mathbf{q} = -\lambda\nabla T + \frac{5}{2}kT\sum_{i=1}^{N} n_i\mathbf{V}_i + p\sum_{j=1}^{N} k_{\mathrm{T}}\mathbf{V}_i, \qquad (1)$$

where λ is the heat conductivity coefficient, k_{T_i} are the thermodiffusion ratios, $\mathbf{V}_i$ are vectors of diffusion velocities, and n_i is the number density of particles of the ith component.

Coefficients λ and k_{T_i} are expressed in terms of integral brackets. In final form, they are expressed in terms of the omega integrals $\Omega^{(l, s)}$, which are calculated based on given interaction potentials and depend on temperature [3].

In the framework of the ξ approximation with respect to the Sonin polynomials, the heat-conduction coefficient $[\lambda]_\xi$ is determined by the first coefficient in the $\alpha_1(\xi)$ expansion in terms of the Sonin polynomials. This coefficient is found by solving the following system of algebraic equations:

$$\frac{75nk}{8}\sum_{j=1}^{N}\sum_{p=1}^{\xi-1}\Lambda_{ij}^{m,p}\alpha_{j,p} = \frac{15}{4}x_i\delta_{m1}, \qquad (2)$$
$$i = 1, \ldots, N, \quad m = 1, 2, \ldots, \xi - 1.$$

Elements $\Lambda_{i,j}^{m,p}$ are the combinations of integral brackets $[S_{3/2}^{(m)}, S_{3/2}^{(p)}]$ (see [1]), which are formed by Sonin polynomials $S_{3/2}^{(p)}$ and can be expressed through the omega integrals.

Thermodiffusion relations (in the ξ approximation with respect to the Sonin polynomials) can also be derived from the system of algebraic equations, with the matrix of coefficients in the left-hand side being the same as that for the heat-conduction coefficients. All other transport coefficients are found in a similar way.

Singularity conditions. We now consider the matrices involved in the expressions for transport coefficients that follow from the solution to the system of algebraic equations (2). Evidently, this solution does exist when the matrix of system (2) has no singularities; i.e., the determinant of the matrix in the denominator (we denote it by $\mathbf{D}_2$) does not vanish. For the short-range potentials, this condition is met [1]. However, the numerical calculations suggest that for actual gas mixtures the determinant of the denominator matrix for

Institute of Mathematical Modeling,
Russian Academy of Sciences,
Miusskaya pl. 4a, Moscow, 125047 Russia

1028-3358/00/4509-0499$20.00

heat-conduction coefficients of thermodiffusion ratios can take both positive and negative values. This implies the existence of a point where the matrix determinant $\mathbf{D}_2$ vanishes.

To simplify the analysis, we consider the second approximation in ξ for the binary mixture consisting of two particle species with different interaction potentials and cross sections. To find the singularity condition, we set $\mathbf{D}_2 = 0$:

$$\Lambda_{11}^{1,1}\Lambda_{22}^{2,2} - \Lambda_{12}^{1,2}\Lambda_{21}^{1,2} = 0. \quad (3)$$

The combinations of integral-brackets $\Lambda_{ij}^{1,1}$ for the binary mixture are expressed in terms of the $\Omega^{(l,s)}$ integrals:

$$\Lambda_{ij}^{1,1} = 8\frac{m_i^{1/2}m_j^{1/2}}{75k^2T}\left\{\delta_{ij}\sum_{l=1}^{N} x_i x_l \times 8\mu_l\left[\frac{5}{4}(6\mu_i^2 + 5\mu_l^2)\Omega_{il}^{(1,1)}\right.\right.$$

$$\left. - 5\mu_l^2\Omega_{il}^{(1,2)} + \mu_l^2\Omega_{il}^{(1,3)} + 2\mu_i\mu_l\Omega_{il}^{(2,2)}\right] \quad (4)$$

$$\left. - 8x_i x_j \mu_i^{3/2}\mu_l^{3/2}\left(\frac{55}{4}\Omega_{ij}^{(1,1)} - 5\Omega_{ij}^{(1,2)} + \Omega_{ij}^{(1,3)} - 2\Omega_{ij}^{(2.2)}\right)\right\},$$

where $x_i = n_i/n$ are the molar fractions of the components and μ_i is the reduced mass of the ith component.

Since the second term in expression (3) for $\mathbf{D}_2$ is always positive but the first one involves negative components, expression (3) as a whole can, in principle, vanish.

We now consider a particular case of the mixture of particles with similar masses but with sufficiently different scattering cross sections (e.g., the binary mixture of isotopes of different elements or the dissociated mixture of atoms, one sort of them being in the ground state and the other in the excited state). In this case, we obtain for the binary mixture

$$\Lambda_{11}^{1,1} = 4x_1^2\Omega_{11}^{(2,2)}$$

$$+ x_1x_2\left[\frac{55}{4}\Omega_{12}^{(1,1)} - 5\Omega_{12}^{(1,2)} + \Omega_{12}^{(1,3)} + 2\Omega_{12}^{(2,2)}\right],$$

$$\Lambda_{22}^{1,1} = 4x_2^2\Omega_{22}^{(2,2)}$$

$$+ x_1x_2\left[\frac{55}{4}\Omega_{12}^{(1,1)} - 5\Omega_{12}^{(1,2)} + \Omega_{12}^{(1,3)} + 2\Omega_{12}^{(2,2)}\right],$$

$$\Lambda_{12}^{1,1} = -x_1x_2\left[\frac{55}{4}\Omega_{12}^{(1,1)} - 5\Omega_{12}^{(1,2)} + \Omega_{12}^{(1,3)} - 2\Omega_{12}^{(2,2)}\right].$$

Furthermore, we use the recursion relation for omega integrals $\Omega^{(l,s)}$ of the highest orders in s [3]:

$$T\frac{d\Omega_{ij}^{(l,s)}}{dT} + \left(s + \frac{3}{2}\right)\Omega_{ij}^{(l,s)} = \Omega_{ij}^{(l,s+1)}.$$

As a result, eventual singularity condition for matrix determinant $\mathbf{D}_2$ in (3) takes the form

$$F + 10\Omega_{12}^{(1,1)} = -2T\frac{d\Omega_{12}^{(1,1)}}{dT} - T^2\frac{d^2\Omega_{12}^{(1,1)}}{d^2T}, \quad (5)$$

where $F = F(\Omega_{11}^{(2,2)}, \Omega_{22}^{(2,2)}, \Omega_{12}^{(2,2)})$ is the positive function of the omega integrals and

$$F(\Omega_{11}^{(2,2)}, \Omega_{22}^{(2,2)}, \Omega_{12}^{(2,2)}) \quad (6)$$

$$= \frac{4[x_1^2\Omega_{11}^{(2,2)}\Omega_{12}^{(2,2)} + x_2^2\Omega_{22}^{(2,2)}\Omega_{12}^{(2,2)} + 2x_1x_2\Omega_{11}^{(2,2)}\Omega_{22}^{(2,2)}]}{2x_1^2\Omega_{11}^{(2,2)} + x_2^2\Omega_{22}^{(2,2)} + 3x_1x_2\Omega_{12}^{(2,2)}}.$$

Hence, if the cross sections of cross pairs (i.e., of different-sign particles) decreases with energy, so that omega integral $\Omega_{12}^{(1,1)}(T)$ decreases with temperature, then, at a certain temperature $T = T_c$, algebraic relationship (3) could be met and the matrix determinant of (2) would vanish. In this case, we can verify that the determinant of the numerator matrix does not vanish for this solution.

Particular case. As an example, we consider the case of the cross-particle interactions described by the attractive or repulsive potentials having the inverse-power form $V(R) = \pm C/R^n$. Then, omega integrals are described by the following functions of temperatures [3]:

$$\Omega_{12}^{(l,s)} = \left(\frac{\pi kT}{2\mu}\right)^{1/2}\left(\frac{n|C|}{kT}\right)^{2/n}\Gamma\left(s + 2 - \frac{2}{n}\right)A^l(n),$$

where μ is the reduced mass of two colliding particles.

The interaction of identical-sign particles remains arbitrary and could correspond to any type of interaction potential. Then, if integral $\Omega_{12}^{(1,1)}(T)$ decreases with temperature according to the power law with the power index $n < 4$, then the right-hand side of (5) is positive. The solution to (5) does exist and, at the point $T = T_c$, the matrix determinant $\mathbf{D}_2$ vanishes.

Note that the long-range potentials of repulsive and attractive forces decreasing as R^{-m} ($2 \le m < 4$) were considered in [4].

Numerical test. Numerical calculations of transport coefficients λ and k_{T_i} were performed for a number of partly dissociated and ionized mixtures CO_2 + Ar, N_2 + O_2, F_2, etc. In these mixtures, the interaction potentials for different particles are characterized by fundamen-

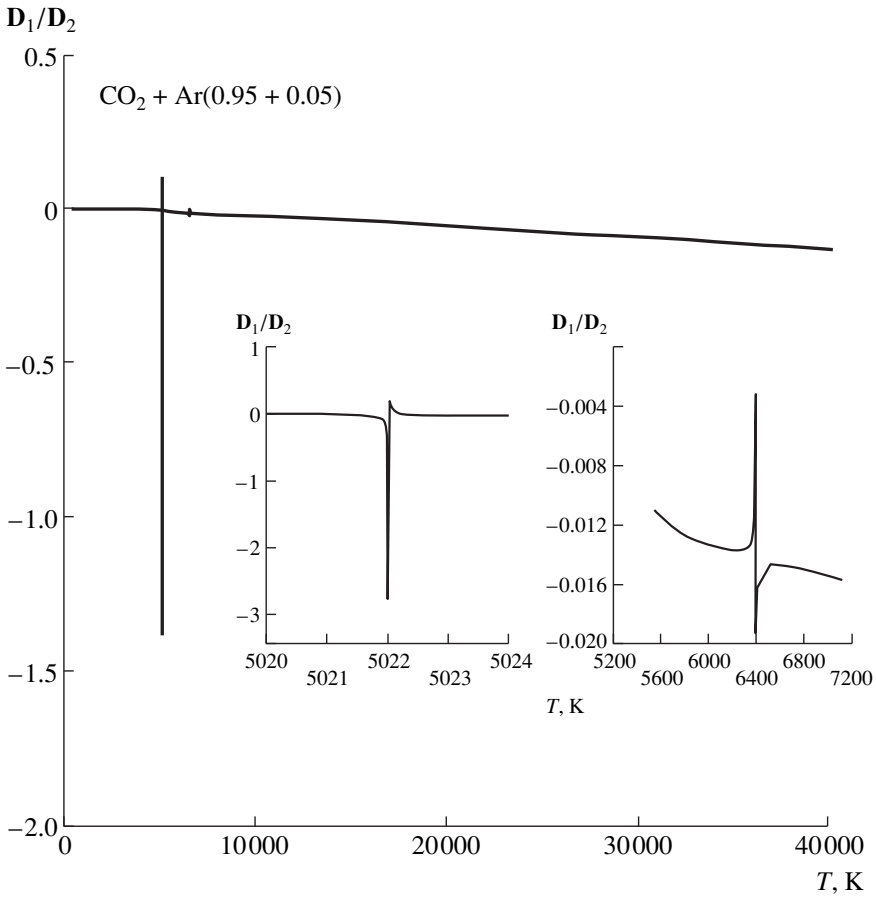

Fig. 1. Ratio of the matrix determinants involved in heat-conduction coefficient as a function of temperature for CO_2 + Ar gas mixture in the chemical-equilibrium state.

tally different behavior. In particular, the interaction of ions and neutrals is described by long-range potentials giving rise to decreasing omega integrals. Collision integrals for the electron–atom pairs (for Ar atoms, etc.) do decrease with temperature.

The ratio $\mathbf{D}_1/\mathbf{D}_2$ of the determinants for the matrices in the numerator and denominator calculated within the fourth-order approximation ($\xi = 4$) for the chemically equilibrium mixtures CO_2 + Ar and F_2 are presented in Figs. 1 and 2, respectively.

These numerical calculations were performed in the fourth-order approximation in terms of the Sonin polynomials, because it is in this case the singular point can be most clearly resolved numerically. In the vicinity of a certain temperature $T = T_c$ (at sufficiently small computation steps along the temperature axis), the singularity in the behavior of the denominator matrix manifests itself. At the very point $T = T_c$, the denominator matrix vanishes. The regions in the vicinity of these points (calculated with small temperature step) are shown in the same figures as additional plots drawn in a larger scale.

The numerical calculations demonstrate that the value of T_c can vary slightly with the change in the parameters of the potential.

Thus, within the method employing the expansion in terms of the Sonin polynomials, to the first approximation within the Chapman–Enskog theory, there appears a problem related to the fact that, at certain types of particle-interaction potentials, the matrix of algebraic equations (involved in the expressions for the transport coefficients) can be singular. Then, the matrix in the denominator should be zero. This singularity occurs in the gas mixtures when interaction of certain particle pairs are described by the long-range potential and the omega integrals are decreasing functions of temperature.

For actual calculations, the presence of a singularity is not, in general, a dramatic feature. This singularity manifests itself within rather narrow temperature ranges; numerically, we can overcome this problem by choosing a smaller step. Thus, this region could be eliminated in the course of numerical calculations of the transport coefficients. On the other hand, in gas-dynamic calculations, the transport coefficients, as a rule, are computed according to approximate formulas

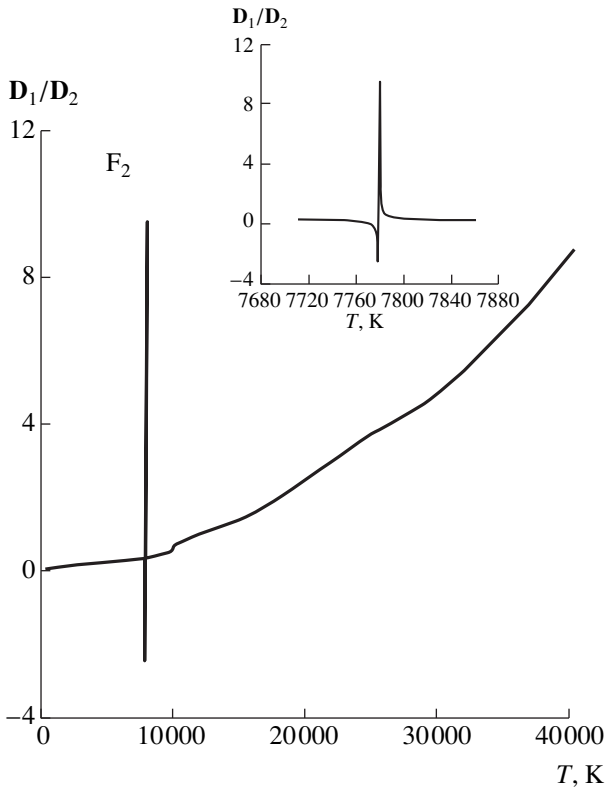

Fig. 2. Ratio of the matrix determinants involved in the heat-conduction coefficient as a function of temperature for F_2 gas mixture in the chemical equilibrium state.

(see [5]) of kinetic theory. These formulas are either simplified expressions of this theory or fit numerical data for transport coefficients. Thus, they can be reduced to simple algebraic relations that do not involve any matrix determinants. Therefore, the singularity under study has no relation to calculations employing the approximate formulas. However, program packages for computations in the field of applied gas dynamics can involve modules for calculations of the transport coefficients, which are based on formulas of rigorous kinetic theory. In this case, a random coincidence with the point $T \approx T_c$ could result in the complete failure of the computation process.

ACKNOWLEDGMENTS

This work was supported by the Russian Foundation for Basic Research, project no. 97-01-00005.

REFERENCES

1. J. H. Ferziger and H. G. Kaper, *Mathematical Theory of Transport in Gases* (North-Holland, Amsterdam, 1972; Mir, Moscow, 1976).
2. A. F. Kolesnikov and G. A. Tirskiĭ, in *Molecular Gas Dynamics* (Nauka, Moscow, 1982), pp. 20–44.
3. J. O. Hirschfelder, C. F. Curtiss, and R. B. Bird, *Molecular Theory of Gases and Liquids* (Wiley, New York, 1954; Inostrannaya Literatura, Moscow, 1961).
4. G. Ya. Gerasimov *et al.*, in *Obz. Teplofiz. Svoĭstvam Veshchestv*, No. 6 (86) (1990), p. 137.
5. I. A. Sokolova, in *Obz. Teplofiz. Svoĭstvam Veshchestv*, No. 2 (94) (1992), p. 100.

Translated by O. Chernavskaya

Doklady Physics, Vol. 45, No. 9, 2000, pp. 503–505. Translated from Doklady Akademii Nauk, Vol. 374, No. 3, 2000, pp. 340–342.

MECHANICS

Cathode Phenomena in the Self-Maintained Glow Discharge in a Supersonic Air Flow

Corresponding Member of RAS V. M. Fomin*, T. Alziary de Roquefort, A. V. Lebedev*, and A. I. Ivanchenko***

Received May 26, 2000

The self-maintained glow discharge in a supersonic gas flow is of interest from the viewpoint of the interaction of shock waves with nonequilibrium plasma as well as from the viewpoint of its applications for control of external and internal streamlines. As a fundamental phenomenon, the glow discharge is far from being well understood and there are almost no data on its characteristics. The electrical parameters of the longitudinal discharge in a supersonic air flow were reported just recently in [1, 2]. In [1], data on the spatial electrical characteristics of the discharge are presented. In [2], dependences of the electrical characteristics of discharge on parameters of the incident flow and on the width of interelectrode gap were studied.

In this paper, we study the effect of the cathode regions of the self-maintained glow discharge in the supersonic air flow on the wave pattern of flows. It is shown that plasma in the cathode regions of the discharge manifests itself as a virtual body. For the first time, we present data concerning the distribution of parameters determining flow stagnation (pressure and temperature) in plasma of the cathode layer for such a discharge. The effect of the discharge power on the stagnation parameters is demonstrated.

The experiments were performed in a wind tunnel with the free jet in the operating part. The Mach number of the incident flow was $M_\infty = 3.2$ at velocity $U_\infty = 629$ m/s. The static pressure and temperature were equal to 7.67 torr and 96 K, respectively. In our experiments, as well as in [1, 2], we consider the longitudinal structure of the discharge. As a cathode, we used a body that did not introduce significant disturbances to the flow. The body had the shape of a ring 10 mm in diameter, 2.5 mm in height, and with a wall thickness of 0.5 mm. The anode was made of a metal plate 0.3 mm thick and had a bump on the back side to localize the discharge point. The electrodes were located along the jet symmetry axis at a zero angle of attack. The electrode gap was 41 mm wide. In each experiment, the discharge was burning during approximately 20 s. The visualization of the discharge was performed by taking color photos, shadow visualization of the wave flow pattern, and using measurements of profiles of the total pressure and stagnation temperature in the discharge area. In addition, we recorded the values of current intensity and voltage across electrodes.

The physical configuration of the discharge is shown in Fig. 1. The discharge can be divided into four regions.

(1) The cathode layer (the region of the cathode voltage drop), the region of the blue-violet glow covering the surface of the cathode ring. The characteristic thickness of this layer determined with the help of the photographic pictures is approximately equal to 0.2 mm.

(2) The near-cathode region. This is the object of our investigation. This area of discharge has the shape of a cylinder with a conical nose part. The rose-orange color dominates in its visible glow spectrum. With an increase in the discharge current, the diameter and the length of this area also increase (the region becomes wider toward the incident flow).

(3) The discharge column. This region has the shape of a truncated cone with pronounced elongation. It is a conductor closing the near-cathode and anode regions.

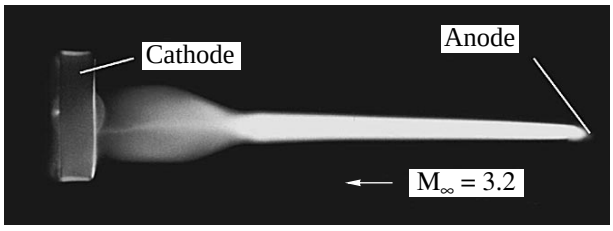

Fig. 1. The physical configuration of the discharge.

* *Institute of Theoretical and Applied Mechanics, Siberian Division, Russian Academy of Sciences, Institutskaya ul. 4/1, Novosibirsk, 630090 Russia*

** *Centre d'Études Aérodynamiques et Thérmiques, 43, Route de l'Aérodrome, 86036 Poitiers Cedex, France*

1028-3358/00/4509-0503$20.00

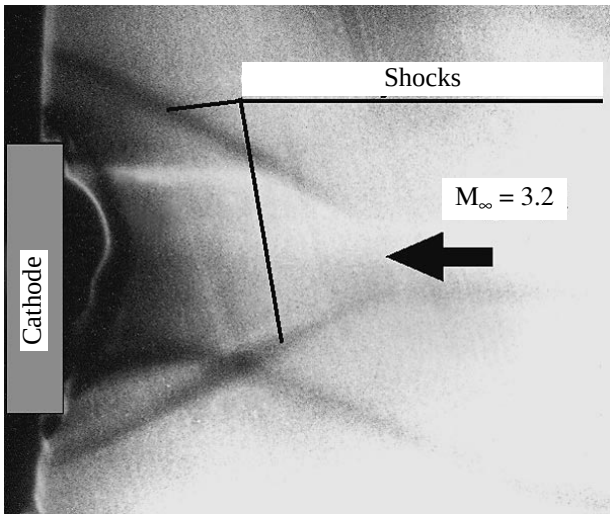

Fig. 2. The wave pattern of the flow in the presence of the discharge.

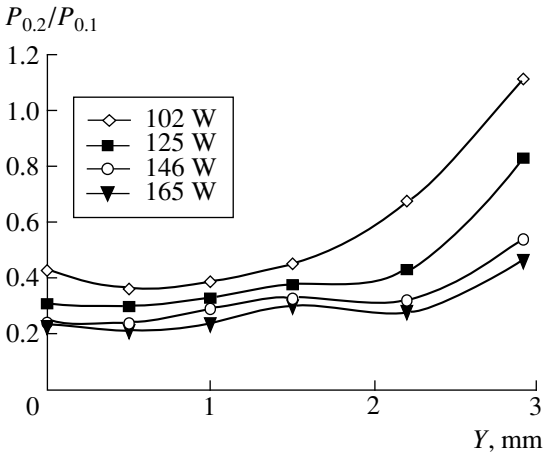

Fig. 3. The distribution of the total pressure in the discharge plasma.

Here, the orange-rose glowing is also observed, but it is more intense than in the near-cathode region.

(4) The anode region (small in size) is formed in the vicinity of the discharge localization point at the anode.

At the discharge current equal to 0.125 A, the lengths of the discharge column and near-cathode region were equal to 27 and 11.5 mm, respectively. The averaged current densities at the boundary between the anode area and discharge column in the middle cross section of the discharge column, at the boundary between the discharge column and the near-cathode region, in the cylindrical part of the near-cathode region, and at the surface of the cathode were equal to 10.2, 4.5, 2.6, 0.4, and 0.08 A/cm^2, respectively. The voltage drop across the discharge gap was equal to 1000 V. This value was the sum of the following voltage drops: approximately 300 V across the anode region, 100 V across the discharge gap, and about 600 V across the cathode region of discharge (at the near-cathode region and in the region of the cathode voltage drop). In each experiment, the effect of the normal current density was clearly pronounced; i.e., the area of the current zone at the cathode surface increased with the current until the entire surface was covered by the glowing. The further growth in the discharge current was accompanied by the increase in its density at the cathode surface. In our experiments, the minimum current density was chosen in such a way that the current zone covered the whole cathode surface. As a result, the discharge became nearly axially symmetric.

The shadow visualization was performed by a conventional technique; i.e., the blade was placed normal to the flow, the steady light source was used, and the exposure time while taking the photos was 10^{-3} s. In the absence of the discharge, we can see small disturbances introduced to the flow by the anode plate and cathode ring. In the presence of the discharge, the wave pattern changed significantly (Fig. 2). At the conic part of the plasma in the near-cathode region of the discharge, the oblique shocks arise. The half-angles of the conical part of the plasma at the cathode and of the oblique shock, measured by the photographic technique, are equal to 22° and 29.5°, respectively. The calculated value of the inclination angle for the oblique shock at the streamline of the circular cone with the same half-angle 22° for the flow with $M_\infty = 3.2$ is equal to 29.6°. Thus, the geometry of the wave patterns arising in the flow around the plasma and solid cones almost coincide; i.e., the plasma in the cathode regions of the discharge behaves like a virtual body.

The distribution of the total pressure in the discharge region was measured with the help of a Pitot tube having an outer diameter of 1 mm. The measurements were performed in the symmetry plane of the discharge at a distance of 2 mm from the front cut of the ring. These results are presented in Fig. 3. Here, P_{02} is the measured value of the total pressure in the presence of the discharge and P_{01} is the total pressure behind the direct shock wave in the absence of the discharge and at the unchanged parameters of the incident flow. A set of curves corresponds to the different values of the discharge power. It follows from the plots that the pressure decreases with increasing the discharge power. In addition, it increases from the axial part to the periphery; the rise being the most significant in the vicinity of the glow zone boundary.

To measure the stagnation temperature, we used a thermocouple 0.1 mm in diameter. It was tightened transversely to the flow. The discharge power was 125 W. It was found that the temperature of the flow, as it passes through the anode region of the discharge, increased by 300 K and was nearly constant in the discharge column. At the near-cathode region, the temperature distribution was measured in the symmetry plane

of the discharge at a distance of 4 mm from the front cut of the ring. The result is shown in Fig. 4, where ΔT_0 denotes the difference between the stagnation temperatures at a given point with and without the discharge, provided that the parameters of the incident flow are unchanged. The temperature is slightly altered in the paraxial area and rapidly drops at the periphery; i.e., similarly to the total pressure, the temperature changes mainly in the vicinity of the plasma boundary. Note that the distance at which the stagnation temperature becomes equal to that in the incident flow nearly coincides with the radius of the glowing area. It is evident that the total heat release in the near-cathode region increases compared to that in the discharge column. Indeed, the cross section area of the cylindrical part at the near-cathode region exceeds by an order of magnitude the corresponding cross-sectional area for the discharge column, whereas temperatures in both regions are close. As was mentioned above, the current density in the near-cathode region is well below that in the discharge column. Therefore, we would here expect high values of the electric field compared to those in the discharge column causing the increase in the heat release. The near-cathode region can be considered as the self-maintained discharge between the discharge column and the cathode. The electric current lines here possess radial components, and a double electric layer must appear at the boundary of the current-carrying zone of the discharge. A two-dimensional pattern of the electric fields must be similar to those arising in the transverse electric discharges in subsonic flows [3]. The comparison of the photographs for the discharge and the wave pattern of the flow in the experiments both with the ring-shape and blunted bodies demonstrated that significant changes in the flow (in particular, the generation of oblique shocks) are observed in such regions where the electric-current lines diverge. Therefore, it is reasonable to suppose that the mechanism underlying the changes in the flow is the same in the experiments both with circular and blunted bodies.

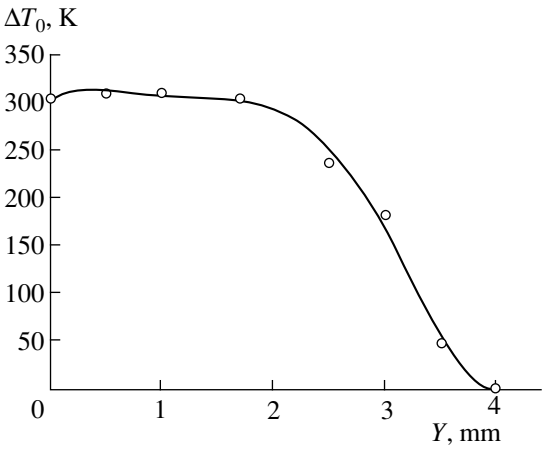

Fig. 4. The distribution of the stagnation temperature in the discharge plasma.

ACKNOWLEDGMENTS

This work was supported by the Russian Foundation for Basic Research, project no. 98-02-17936.

REFERENCES

1. V. M. Fomin, A. V. Lebedev, and A. I. Ivanchenko, Dokl. Akad. Nauk **361**, 58 (1998) [Dokl. Phys. **43**, 443 (1998)].
2. V. M. Fomin, T. A. de Roquefort, A. V. Lebedev, and A. I. Ivanchenko, Dokl. Akad. Nauk **370**, 623 (2000) [Dokl. Phys. **45**, 84 (2000)].
3. A. I. Ivanchenko and A. A. Shepelenko, Zh. Tekh. Fiz. **51**, 2043 (1981) [Sov. Phys. Tech. Phys. **26**, 1191 (1981)].

Translated by Yu. Vishnyakov